

# **Cladding Formation in Laser-Beam Fusion of Metal Powder**

by

**Vladimir Yevko**

A thesis submitted in conformity with the requirements  
for the Degree of Master of Applied Science in the  
Department of Mechanical and Industrial Engineering,  
University of Toronto

Copyright © December 1997, by Vladimir Yevko



National Library  
of Canada

Acquisitions and  
Bibliographic Services

395 Wellington Street  
Ottawa ON K1A 0N4  
Canada

Bibliothèque nationale  
du Canada

Acquisitions et  
services bibliographiques

395, rue Wellington  
Ottawa ON K1A 0N4  
Canada

*Your file* *Votre référence*

*Our file* *Notre référence*

The author has granted a non-exclusive licence allowing the National Library of Canada to reproduce, loan, distribute or sell copies of this thesis in microform, paper or electronic formats.

The author retains ownership of the copyright in this thesis. Neither the thesis nor substantial extracts from it may be printed or otherwise reproduced without the author's permission.

L'auteur a accordé une licence non exclusive permettant à la Bibliothèque nationale du Canada de reproduire, prêter, distribuer ou vendre des copies de cette thèse sous la forme de microfiche/film, de reproduction sur papier ou sur format électronique.

L'auteur conserve la propriété du droit d'auteur qui protège cette thèse. Ni la thèse ni des extraits substantiels de celle-ci ne doivent être imprimés ou autrement reproduits sans son autorisation.

0-612-33971-8

*To My Family*

## **ACKNOWLEDGMENTS**

I am sincerely grateful to my thesis supervisors, Professors B. Benhabib and C. B. Park for their invaluable guidance, encouragement, and support throughout the course of this thesis. I also must thank Professor T. W. Coyle from the Department of Metallurgy and Material Science for his comments on material- and process-related issues.

I wish to thank all of my colleagues and friends at the University of Toronto Computer Integrated Manufacturing Laboratory for their helpful comments, opinions and advice. In particular, I must thank Gene Zak for his valuable comments and contributions, particularly in computer programming and all aspects related to thesis writing. The assistance, provided by Dr. M. N. Sela for the mechanical design and computer simulation aspects of this thesis are also greatly appreciated. This work would have been much more difficult without Dr. A. Qamhiyah's help in the field of computer-aided design and simulation, and for this, I am very grateful. Also, I wish to thank Martin Bonert for his continuous willingness to help with anything.

Finally, I must thank my beloved wife, Marina, for her love, support and understanding in everything I have done, and my kids, Ksenia, Sofia, and Daniel for their love and patient waiting for daddy to come home.

## **ABSTRACT**

Over the past decade, many novel layered-manufacturing techniques have been used successfully for building complex 3D parts. However, parts built by these Rapid Prototyping (RP) methods have been used either for checking fit and geometry, or as models for subsequent creation of fully-densed metal parts using investment casting. Due to increased market competition and, in turn, shortened product development cycles, there is a demand to rapidly create the functional fully-densed metal parts without hard tooling.

A possible solution to this problem is layered Rapid Manufacturing (RM), for example, via laser-beam fusion of metal powder. The RM process proposed in this thesis is based on this approach. It involves selective laser-beam scanning of a predeposited metal-powder layer. The laser beam melts the powder locally, forming fully-densed claddings, as the basic building block of individual layers.

This thesis specifically addresses only one of the fundamental issues of the proposed RM process, namely the fabrication of single claddings. The most important process parameter, in this context, is the laser-beam scanning speed. The influence of this process parameter on cladding's descriptive parameters was investigated for two possible laser-working modes: pulsed and continuous.

The theoretical investigation of the process-parameter influence on cladding's geometrical properties employed computer modeling and process simulation. The commercial finite-difference, thermal-modeling software I-DEAS TMG was used for the determination of the global temperature fields within the powder layer and the metal substrate due to the application of a laser-beam heat source. The cladding's expected

geometry was reconstructed using an algorithm based on surface analytical geometry. The relationships between cladding's geometrical properties, namely its width and height, and the scanning speed were determined for both laser-working modes.

In order to verify the findings of the process simulations, numerous experiments, involving fabrication of single claddings, were carried out with varying process parameters. A generic experimental set-up, which can be used for both laser-working modes, was designed, built and utilized for this purpose. Comparisons of the process simulations and experimental results showed good agreement in terms of overall trends.

# TABLE OF CONTENTS

<b>ACKNOWLEDGMENTS</b>	<b>iii</b>
<b>ABSTRACT</b>	<b>iv</b>
<b>TABLE OF CONTENTS</b>	<b>vi</b>
<b>LIST OF FIGURES</b>	<b>xi</b>
<b>LIST OF TABLES</b>	<b>xiv</b>
<b>NOMENCLATURE AND ACRONYMS</b>	<b>xv</b>
<b>1. INTRODUCTION</b>	<b>1</b>
<b>1.1 Motivation</b>	<b>1</b>
<b>1.2 Overview of Existing Rapid Manufacturing Technologies</b>	<b>3</b>
1.2.1 Conventional Welding-Based Processes	3
1.2.1.1 3D Welding	3
1.2.1.2 Shape-Deposition Manufacturing	4
1.2.2. Laser-Based Powder-Spraying Processes	5
1.2.2.1 Directed Light Fabrication	5
1.2.2.2 Aluminum-Powder Spraying	5
1.2.2.3 Laser Cladding	6
1.2.2.4 Laser Generating	6
1.2.2.5 Laser Engineered Net Shaping	7
<b>1.3 Overview of Process-Simulation Techniques</b>	<b>7</b>

<b>1.4 Thesis Objective</b>	<b>9</b>
<b>1.5 Thesis Organization</b>	<b>10</b>
<b>2. PROBLEM FORMULATION AND PROPOSED SOLUTION</b>	<b>11</b>
<b>2.1 Description of the Proposed Process</b>	<b>11</b>
<b>2.2 Process Parameters and Properties of the Cladding</b>	<b>12</b>
2.2.1 Identification of Process Parameters	14
2.2.1.1 Laser's Working Mode	14
2.2.1.2 Power Level and Diameter of the Laser Beam	14
2.2.1.3 Pulse Frequency and Duration	15
2.2.1.4 Scanning Speed	16
2.2.1.5 Other Parameters	16
<b>2.3 Methodology</b>	<b>17</b>
2.3.1 Computer Simulation	17
2.3.2 Experimental Verification	17
<b>3. PROCESS SIMULATION</b>	<b>18</b>
<b>3.1 Background Theory</b>	<b>18</b>
3.1.1 Heat Transfer	18
3.1.2 Finite-Difference Method	20
3.1.3 Thermal-Modeling Software	22
<b>3.2 Process Model</b>	<b>26</b>
3.2.1 Description of the Process Model	26
3.2.2 Calculation of Powder's Thermal Properties	28
<b>3.3 Thermal-Modeling Procedure</b>	<b>31</b>
3.3.1 Pulsed Laser	32



3.3.2 Continuous Laser	33
<b>3.4 Heat-Transfer Analysis Simulation Results</b>	<b>35</b>
<b>3.5 Calculation of Cladding Shape Properties for the Pulsed Laser</b>	<b>47</b>
3.5.1 Assumptions	47
3.5.2 Cladding Width Calculation	48
3.5.3 Cladding-Height Calculation	50
3.5.4 Longitudinal, Centerline Cross-Section of the Pulsed-Laser Cladding	55
<b>3.6 Calculation of Cladding-Shape Properties for a Continuous Laser</b>	<b>57</b>
<b>3.7 Simulation Results of Cladding's Shape-Properties</b>	<b>58</b>
3.7.1 Discussion	60
3.7.1.1 Cladding Width	60
3.7.1.2 Cladding Height	61
<b>4. DESIGN OF EXPERIMENTAL SET-UP</b>	<b>62</b>
<b>4.1 Axiomatic Approach to Design</b>	<b>62</b>
<b>4.2 Identification of Main Functional Requirements</b>	<b>63</b>
<b>4.3 Selection of the First-Level Design Parameters</b>	<b>64</b>
4.3.1 First-Level, Design-Matrix Considerations	65
<b>4.4 Design Decomposition</b>	<b>67</b>
4.4.1 Powder Delivery and Leveling	67
4.4.1.1 Powder-Delivery Subsystem	68
4.4.1.2 Wiping Subsystem	70
4.4.2 Laser-Light Delivery	72
4.4.3 Horizontal Motion Subsystem	73
4.4.4 Vertical-Motion Subsystem	74

<b>5. EXPERIMENTS</b>	<b>77</b>
<b>5.1 Experiments with A Pulsed Laser</b>	<b>77</b>
5.1.1 Experimental Set-Up	77
5.1.2 Experimental Procedure	78
5.1.3 Experimental Results	79
5.1.4 Comparison to Simulation Results	84
<b>5.2 Experiments with a Continuous Laser</b>	<b>85</b>
5.2.1 Experimental Set-Up	85
5.2.2 Experimental Procedure	86
5.2.3 Experimental Results	87
5.2.4 Comparison to Simulation Results	89
<b>6. CONCLUSIONS</b>	<b>92</b>
<b>6.1 Summary</b>	<b>92</b>
<b>6.2 Conclusions</b>	<b>93</b>
<b>6.3 Recommendations</b>	<b>94</b>
<b>REFERENCES</b>	<b>95</b>
<b><i>APPENDIX A: Thermal Modeling with I-DEAS TMGError! Bookmark not defined.</i></b>	
<b>A.1 Model Meshing</b>	<b>100</b>
<b>A.2 Boundary Conditions</b>	<b>101</b>
A.2.1 Heat Load	101
A.2.2 Convection	104
A.2.3. Initial Temperature Set-up	106
<b>A.3 Analysis Control</b>	<b>107</b>

<b>A.4 Analysis Solution and Post-Processing</b>	<b>108</b>
--	------------

***APPENDIX B: Cladding Geometrical-Properties Calculation***

<b><i>using MATLAB</i></b>	<b>110</b>
----------------------------	------------

<b>B.1 Retrieval of Thermal-Modeling Results</b>	<b>110</b>
--	------------

<b>B.2 Calculations for the Pulsed-Laser Mode</b>	<b>110</b>
---	------------

<b>B.3 Calculations for the Continuous-Laser Mode</b>	<b>112</b>
---	------------

## LIST OF FIGURES

Figure 2.1. Single-Cladding Building. ....	11
Figure 2.2. Proposed Process. ....	12
Figure 3.1. Nomenclature Used in Two-Dimensional Finite-Difference Analysis of Heat Conduction.....	21
Figure 3.2. Temperature Field Around Impulse Point Source. Analytical and Numerical Solutions.....	26
Figure 3.3. Model of Physical Set-Up. ....	27
Figure 3.4. Thermal Conductivity versus Temperature for AISI 316 Stainless Steel. ....	29
Figure 3.5. Specific Heat versus Temperature for AISI 316 Stainless Steel.....	29
Figure 3.6. Thermal Conductivity versus Temperature for AISI 316 Stainless Steel Powder.....	31
Figure 3.7. The Scheme of the Laser Beam Scanning Model for the Pulsed Laser. ....	33
Figure 3.8. Laser-Beam Spot Model for Continuous Laser. ....	34
Figure 3.9. Heat Load Input for Continuous-Laser Simulation.....	35
Figure 3.10. Definition of Longitudinal and Transverse Temperature Profiles. ....	37
Figure 3.11. Longitudinal Temperature Profiles. Pulsed Laser. 1.76 mm/s Scanning Speed.....	38
Figure 3.12. Longitudinal Temperature Profiles. Pulsed Laser. 3.52 mm/s Scanning Speed.....	39
Figure 3.13. Longitudinal Temperature Profiles. Pulsed Laser. 5.28 mm/s Scanning Speed.....	40

Figure 3.14. Thermal Cycles. Pulsed Laser. 1.76 mm/s Scanning Speed. ....	42
Figure 3.15. Longitudinal Temperature Profiles.	
Continuous Laser. 0.75 mm/s Scanning Speed. ....	43
Figure 3.16. Longitudinal Temperature Profiles.	
Continuous Laser. 1.76 mm/s Scanning Speed. ....	44
Figure 3.17. Longitudinal Temperature Profiles.	
Continuous Laser. 3.52 mm/s Scanning Speed. ....	45
Figure 3.18. Longitudinal Temperature Profiles.	
Continuous Laser. 7.04 mm/s Scanning Speed. ....	46
Figure 3.19. Typical Transverse Temperature Profiles for Continuous Laser .....	47
Figure 3.20. Temperature-Profile Projection. ....	48
Figure 3.21. Conic Shape of the Molten Powder. ....	49
Figure 3.22. Cladding Height Calculation for A Pulsed Laser. ....	53
Figure 3.23. Nomenclature Used in the Calculation of Geometrical Properties	
of the Second Segment. ....	54
Figure 3.24. Longitudinal Centerline Cross-Section Profile of the Cladding	
Produced by a Pulsed Laser (14 Hz). ....	56
Figure 3.25. Geometric Approximation of A Cladding Produced	
by a Continuous Laser. ....	57
Figure 3.26. Cladding Width versus Scanning Speed. ....	59
Figure 3.27. Cladding Height versus Scanning Speed. ....	59
Figure 4.1. Powder-Delivery Working Chamber. ....	69

Figure 4.2. Wiping Subsystem. ....	71
Figure 4.3. Laser-Light Delivery Subsystem.....	72
Figure 4.4. X-Y Motion System. ....	73
Figure 4.5. Vertical Motion Subsystem.....	75
Figure 4.6. CAD Model of the Set-Up. ....	76
Figure 4.7. Photograph of the Assembled Set-Up.....	76
Figure 5.1. Experimental Set-Up for Pulsed-Laser Experiments. ....	78
Figure 5.2. Powder Leveling. ....	79
Figure 5.3. Typical Cladding’s Cross-Section for Pulsed Laser. ....	80
Figure 5.4. Typical Cladding’s Longitudinal-Centerline Section for Pulsed Laser. ....	80
Figure 5.5. Cladding Width versus Scanning Speed for Pulsed-Laser Experiments. ....	81
Figure 5.6. Cladding Height versus Scanning Speed for Pulsed-Laser Experiments.....	82
Figure 5.7. Cladding Width versus Laser-Power Level for Pulsed-Laser Experiments..	83
Figure 5.8. Cladding Height versus Laser-Power Level for Pulsed-Laser Experiments.	83
Figure 5.9. Experimental versus Simulation Results for Cladding-Width Measurements.....	84
Figure 5.10. Experimental versus Simulation Results for Cladding-Height Measurements.....	85
Figure 5.11. Top View of Cladding. ....	87
Figure 5.12. 45° View of Cladding. ....	87
Figure 5.13. Cladding’s Cross-Section in the Beginning.....	87
Figure 5.14. Cladding’s Cross-Section 2 mm from the Beginning. ....	88

Figure 5.15. Cladding Width versus Scanning Speed for Continuous-Laser Experiments. ....	88
Figure 5.16. Cladding Height versus Scanning Speed for Continuous-Laser Experiments. ....	89
Figure 5.17. Experimental versus Simulation Results for Cladding-Width Measurements. Continuous Laser. ....	90
Figure 5.18. Experimental versus Simulation Results for Cladding-Height Measurements. Continuous Laser. ....	91

## **LIST OF TABLES**

Table 3.1. Values of the Parameters for the Short Pulse-Application Problem. ....	25
Table 3.2. Layer Height versus Scanning Speed for Pulsed Laser (14 Hz).....	55
Table 3.3. Results of the Cladding's Shape-Properties Calculation.....	60
Table 5.1 Chemical Composition of AISI 316 Stainless Steel.....	77

## NOMENCLATURE AND ACRONYMS

A	Area
c	Specific heat
C	Capacitance of control volume
d	Length of element
G	Linear conductive conductance
h	Z-coordinate of spherical mass' center
H	Cladding's height
$H_{pl}$	Original powder-layer thickness
k	Thermal conductivity
$k_c$	Thermal conductivity of continuous phase
$k_d$	Thermal conductivity of dispersed phase
K	Effective thermal conductivity of powder
$l_{hw}$	Heat-wave propagation length
m	Distance between adjacent-pulses centers
q	Heat-transfer rate
$Q_g$	Heat generated within control volume
$Q_n$	Heat flow across control-volume boundaries
R	Spherical-mass radius
$R_{bp}$	Molten-zone radius on the powder-layer bottom surface
$R_c$	Half-width of (i)th spherical mass
$R_{cnew}$	Half-width of (i+1)th spherical mass



$R_{mp}$	Molten-zone radius on the powder-layer mid-surface
$R_{tp}$	Molten-zone radius on the powder-layer top surface
$R_{ts}$	Molten-zone radius on the baseplate's top surface
$t$	Time
$T$	Temperature
$T_0$	Initial Temperature
$U$	Energy stored within control volume
$V$	Volume
$V_m$	Molar volume
$V_p$	Volume of molten powder
$V_p'$	Volume of molten powder for (i+1)th pulse
$V_s$	Solid-mass volume
$V_{ss}$	Scanning Speed
$V_{sg}$	Volume of spherical mass
$x_{new}$	X-coordinate of spherical mass' center
$Z_p$	Maximum height of spherical mass' unmolten part
$\alpha$	Thermal diffusivity
$\beta$	Dimensionless factor for determination of thermal conductivity
$\varepsilon$	Volume fraction of dispersed phase
$\phi$	Factor for determination of thermal conductivity ( $\varepsilon\beta$ )
$\rho$	Density

$\rho_p$	Powder density
$\rho_s$	Solid metal density
AISI	American Iron and Steel Institute
CNC	Computer Numerically Controlled
DP	Design Parameter
FR	Functional Requirement
LOM	Laminated Object Manufacturing
MIG	Metal Inert Gas
Nd-YAG	Neodymium-Yttrium-Aluminum-Garnet
RM	Rapid Manufacturing
RP	Rapid Prototyping
SL	Stereolithography
SLS	Selective Laser Sintering
TEM	Transverse Electromagnetic Mode

# 1. INTRODUCTION

Over the past two decades, various new laser-based manufacturing techniques have been reaching the industrial market. These include precision welding, welding of dissimilar materials, precision cutting and drilling, heat treatment, surface hardening, cladding, and worn-surface repair [1].

One of the recent applications of lasers is in Rapid Prototyping (RP). Parts of complex geometry can now be produced using innovative technologies without hard tooling. Common RP techniques include Stereolithography (SL), Selective Laser Sintering (SLS), and Laminated Object Manufacturing (LOM). These methods use different types of lasers for additive layer-by-layer building of 3D objects [2].

Most commercially-available RP techniques have a common disadvantage: the fabricated parts can normally be used only for checking fit and geometry. Also, most materials used cannot be considered functional. However, some recent progress has been made in the utilization of RP parts for the rapid manufacture of mold cavities and investment- and vacuum-casting shells [3].

Several research groups in the world are currently working on the design and development of Rapid Manufacturing (RM) processes, that would be capable of fabricating functional parts using metals with high melting points. The research reported herein falls into this category.

## 1.1 Motivation

Most of the layered, metallic-part fabrication methods reported in the literature have been based on powder spraying. The powder is normally injected into a molten

metal pool on the surface of a baseplate. Injection is achieved by spraying the powder through a nozzle with the aid of pressurized inert gas, such as Argon. The primary difference among these methods is the design of the nozzle. Materials investigated include aluminum, ferrous alloys, nickel alloys, tungsten and titanium [4, 5].

Researchers have shown that the metallic parts produced by their methods are almost fully dense and have mechanical properties comparable to those produced by conventional methods. However, these parts only have limited 3D geometries, e.g., inclination of the vertical walls cannot exceed  $30^\circ$  (off the vertical plane), since there exists no possibility of using the powder as a support [6]. Even if some support powder were to be deposited onto the baseplate during build time, independently of the molten material deposited via the nozzle, it would be blown away by the stream of gas carrying the molten powder. A potential solution to this problem is the use of a 5-axis motion system for part orientation [7]. In this case, any geometrical feature can be built by maintaining orientation of the scanning path constant with respect to gravity. Another disadvantage of existing methods is the high complexity of the powder-delivery systems. The powder-delivery system requires use of a high-precision flow-metering system in order to precisely control volumetric rate of the deposited powder, which affects the quality of the part built [8].

The research work reported herein represents a preliminary phase in the development of a rapid layered-manufacturing process for fully-densed metal parts. The process adopted is the selective laser-beam scanning (melting) of a thin layer of a metal powder, predeposited over earlier shaped layers. The main feature that distinguishes this

approach from powder-spraying processes is that it enables the building of complex 3D parts by providing necessary support for overhanging and inclined features.

The primary objective of this thesis is the investigation of the process parameters which influence the geometry of a layer built and its material properties. The two primary tasks of research are: (i) process modeling and computer simulation, and (ii) preliminary experimental verification via mechanical system design and testing.

## **1.2 Overview of Existing Rapid Manufacturing Technologies**

The existing RM processes for building fully-densed metal parts can be categorized into two groups - conventional welding based and laser-based powder spraying.

### **1.2.1 Conventional Welding-Based Processes**

These methods are based on the use of a guided welding torch for building parts in a layered fashion. Prior to present-day research in this area, successful applications of this method in the 1960s have been reported by companies such as Krupp, Thussen and Sulzer in Germany. These companies developed welding techniques for fabrication of large, simple-geometry components, such as pressure vessels weighing up to 500 tons. The technique since has become known as "Shape Welding" [4].

#### **1.2.1.1 3D Welding**

Researchers from the Department of Manufacturing Engineering in University of Nottingham, UK, have been working on the development of a technique called "3D Welding" which uses a MIG welding process for fabricating 3D parts [9]. In this method,

a robot-mounted MIG torch builds the part via layer-by-layer welding. The accuracy at the present stage of development is about  $\pm 0.5$  mm. Also, the surface roughness is unacceptable for many cases, but the researchers claim that with better weld control and appropriate cooling they may overcome these limitations.

### 1.2.1.2 Shape-Deposition Manufacturing

This layer-by-layer fabrication method is currently under research at Carnegie-Mellon University [10]. Each layer consists of a primary and a support-structure material. The support-structure material protects the surface of the layer from damage when the next layer is deposited and also helps to support the overhangs. The support structure is removed by etching, when the building process is complete.

The layers are deposited using a variety of techniques such as thermal spraying, welding and microcasting. Subsequently, the layer is shaped by 5-axis machining, and the support material is deposited and shaped. Finally, the layer is shot-peened to control the residual stresses. The method can potentially yield acceptable material properties expected from a welding-based process and an accuracy achievable via CNC machining.

The main benefit of this method is the ability to directly create complex shapes from metals with high melting points, such as steel. Its disadvantages are:

- Multiple processing steps and expensive equipment.
- Long build times. For example, the building of a part with a layer area of under  $40 \text{ cm}^2$  and a height of 4 cm can take over 40 hours.
- Uneconomical consumption of raw materials. For the above-mentioned part

with a weight of 180 g, 4.5 kg of stainless steel and 3.6 kg of copper support material were used, in other words, about 98% of the material was wasted.

## 1.2.2. Laser-Based Powder-Spraying Processes

### 1.2.2.1 Directed Light Fabrication

The Directed Light Fabrication method is under investigation in Los Alamos National Laboratory [7]. In this process, the layer is built by the scanning motion of the laser beam which melts the powder sprayed into the working zone by a powder delivery system. The powder melts upon entering into the focal zone and forms a planar layer upon solidification.

This process can produce very accurate (within a few thousandths of an inch) metal components with nearly full density in a single processing step. Examples of the parts produced during experiments include fully-densed stainless-steel tubes, rods and plates. These, however, have a surface roughness comparable to that of sand-cast objects. Also, currently only 2.5-D parts can be produced, i.e., parts with a constant cross-section.

### 1.2.2.2 Aluminum-Powder Spraying

Researchers in the University of Illinois at Urbana-Champaign are using an aluminum powder for the rapid manufacturing of fully-densed parts [6]. A water-cooled powder-feed tube, with a concentric shield gas nozzle mounted at a 55° angle (off the horizontal) and in the same plane as the direction of travel, for producing straight-lines is used. The nozzle remains at a constant orientation relative to the direction of travel. Test parts included plates and hollow cylinders.

Tensile specimens were produced both parallel and perpendicular to the scanning direction. Mechanical tests showed tensile strengths equal to that of cast material and almost no difference in stress-strain data for both orientations. The density of specimens was found to be 2.4% below that of pure aluminum.

#### 1.2.2.3 Laser Cladding

This process, under development at the University of Liverpool, involves two primary steps: laser-based cladding and conventional machining [4]. The laser and the 4-axis NC milling machine are integrated to avoid repositioning of the part during the fabrication process. The powder-delivery system consists of a single hopper, screw-driven powder feeder mounted on top of the Z-axis. Powder is delivered onto the melting pool by a copper tube.

The primary cladding material used was nearly-spherical Cobalt powder with particle size of 150  $\mu\text{m}$ . Some trials were carried out with AISI 316 stainless steel as well. The claddings were machined after each layer to control the thickness of the part. Thin-walled and rectangular-box-shaped parts were produced. Also, inclined and overhanging sections were built using additional rotational axis of the part in the YZ plane.

#### 1.2.2.4 Laser Generating

This method is currently under development in Fraunhofer-Institute of Production Technology (IPT), Germany [4]. The equipment used comprises a pulsed laser, a 3-axis CNC motion system, and a concentric nozzle for powder delivery. The metal powder is blown into a focused laser beam and melted inside the nozzle, thus, depositing a bead of material onto the surface of the baseplate.



Materials used were AISI 316 stainless steel and cobalt. Simple thin-walled and solid parts as well as complex-geometry turbine blade shapes have been produced. The cladding height was 0.1 mm and the cladding width was in the range of 0.5-1.0 mm. Their surface roughness was in the order of 50  $\mu\text{m}$ .

#### **1.2.2.5 Laser Engineered Net Shaping**

This method is currently under investigation at the Sandia National Laboratories [11]. The equipment comprises a laser, a 3-axis CNC positioning system, and a powder-feeder unit in the form of a concentric nozzle. The laser beam is focused onto the baseplate to create the molten pool, in which powder particles are simultaneously injected by the powder feeder to build up a layer.

Materials investigated include AISI 316 stainless steel, H13 tool steel, tungsten, and Inconel 625. Thin-walled and solid specimens were built for examination of the process-parameters' influence on shape and material properties of the parts. The dimensional tolerances of the parts varied from 0.02 to 0.12 mm in the X and Y directions, and up to 0.4 mm in Z direction.

The parts produced were fully-densed and exhibited mechanical properties comparable to those of the solid material's yield and tensile strength. Tensile test results showed no difference in regard to building direction of the layers.

### **1.3 Overview of Process-Simulation Techniques**

An important part of any investigation of a complex manufacturing process is its mathematical modeling and simulation. In our proposed manufacturing method, the powder absorbs energy from the laser beam. This energy increases the temperature of the

metal powder, directly illuminated by the laser beam and its surrounding area. If the temperature increase is significantly large, the powder undergoes a phase change from solid to liquid. When application of the laser beam ceases, the molten powder solidifies into a fully-densed metal.

From a process modeling and control point of view, it is imperative to understand the underlying trends of the heat-transfer process and determine the functional relationships between the process parameters and the shape and material properties of the resultant metal layer. In this context, the main task is to determine the temperature fields, which can be used in determining the shape properties of the cladding.

Mathematical modeling has been used in the past for laser welding and cladding [14]. The existence of numerical tools, capable of solving complex boundary problems, for which closed analytical solutions do not exist, or are very complicated due to non-linearity of the problems, has been helpful in that respect [12].

Usually, the analytical solution of a process' governing equation can be found only if a considerable number of assumptions are made, thus, reducing correspondence between the mathematical model and reality. For example, in order to account for materials' thermal properties' dependence on temperature, networks of dissimilar materials, phase changes, etc., numerical methods must be employed [13].

Most of the research work in the field of laser-welding modeling is directed toward the investigation of the molten-pool behavior, convective flow of the molten liquid, the microstructure of the solidified part, etc. [14]. On the other hand, the research directed toward the investigation of the process-parameters' influence on the shape properties of laser claddings has been very limited. Existing literature mostly deals with

powder-spraying techniques and provides readers with very simple analytical models [15,16], or numerical models that assume constant volume of molten powder [17,18]. The models represent a laser-cladding process which utilizes powder injection by an axial inclined nozzle. The volume of the molten powder is assumed to be constant and equal to that of deposited powder, which significantly simplifies the simulation procedure. The relationships between the process parameters, such as scanning speed, and cladding geometrical properties, such as width and height, are determined.

#### **1.4 Thesis Objective**

The primary objective of this thesis is the investigation of process parameters for a metal-based, layered RM technique, which influence the geometrical-shape and material properties of the layers. The proposed process is based on the laser-beam fusion of predeposited metal powder and its selective formation into a desired cross-section layer.

The primary research tasks planned include:

- Process modeling and computer simulation:
  - ◇ Thermal modeling of the process based on a finite differences method, and
  - ◇ Determination of layer geometrical properties based on analytical-geometry formulation.
- Experimental verification of simulation results:
  - ◇ Mechanical design of the experimental setup, and
  - ◇ Testing of process performance for two different laser sources.

## **1.5 Thesis Organization**

The manufacturing process adopted for this research is of a complex nature, involving several physical phenomena, such as energy transfer, and heat and mass transfer with phase change. In Chapter 2, the proposed process will be first described and the relevant process parameters, which influence the process' outcome, will be identified. In Chapter 3, the mathematical aspects pertinent to the process simulation will be presented. Since the main physical phenomenon involved is heat propagation, the necessary background theory will be briefly discussed, followed by the choice of suitable mathematical models to be used for the computer simulations. The procedure for determination of the layer geometrical properties will be outlined. Results of extensive simulations will be presented and discussed.

Chapter 4 will outline the mechanical design of the experimental set-up. Various aspects relevant to the layout of the system and design decisions will be presented. In Chapter 5, the experimental procedure and results of the experimental work will be outlined. A comparison of the experimental and simulation results will be presented and discussed.

Finally, conclusions and recommendations for future work will be summarized in Chapter 6.

## 2. PROBLEM FORMULATION AND PROPOSED SOLUTION

Manufacturing and testing of prototypes are among the most time-consuming tasks in the cycle of product development. In order to be functional, a prototype requires geometrical and material properties similar to those of the final product. Although, it is now possible to fabricate functional metal components by utilizing investment casting [19], a real improvement would be the direct rapid manufacturing (RM) of the metal parts. The novel solution proposed herein is an additive layer-by-layer RM process, which uses a laser-beam energy for selective scanning of a thin layer of a metal powder predeposited over layers built earlier.

### 2.1 Description of the Proposed Process

The first step in the proposed manufacturing process is the representation of the part in the form of a CAD solid model, with its subsequent slicing into “thin” 2.5D layers. The selective laser-scanning paths are then generated for each layer. The actual fabrication process involves the laser-beam fusion of the predeposited metal powder layer, Figure 2.1.

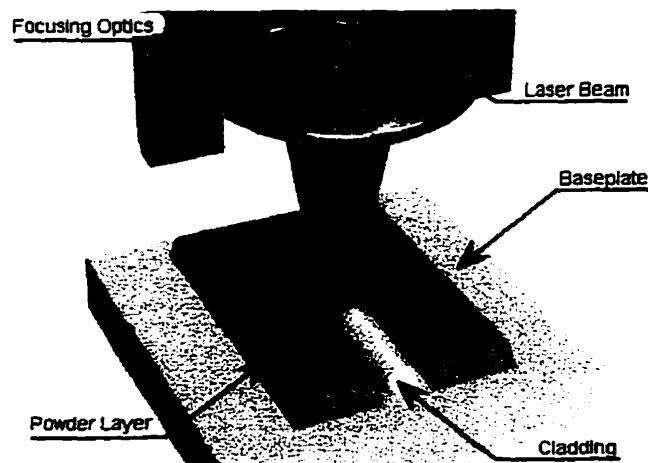


Figure 2.1. Single-Cladding Building.

The process must take place in an inert gas (argon) environment in order to eliminate oxidation and powder burning. The laser beam, scanning the surface of the powder layer, selectively melts the powder, producing fully-densed claddings.

The individual processing steps for building a multi-layered part are as follows:

- (1) A powder-container unit deposits the powder onto the top surface of the baseplate, Figure 2.2(a).
- (2) A wiper levels the powder yielding the required layer thickness, Figure 2.2(b).
- (3) A laser beam selectively melts the metal powder, Figure 2.2(c).
- (4) A piston lowers the part by the required height, Figure 2.2(d), and the process Steps (1) to (3) are repeated.

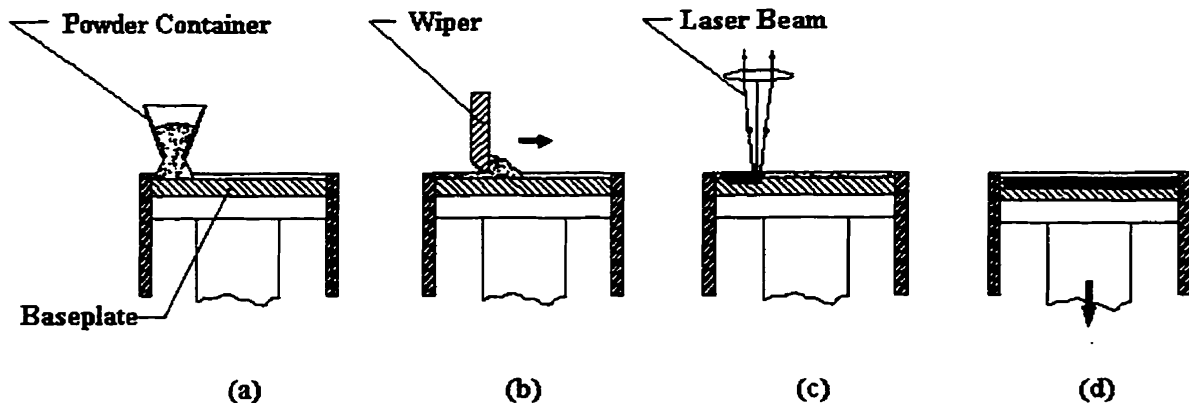


Figure 2.2. Proposed Process.

## 2.2 Process Parameters and Properties of the Cladding

The most fundamental processing issue is the “drawing” of a single cladding line. The repetitive building of these claddings, with good material properties, surface finish, and low variability of the geometrical properties, leads to the fabrication of a multi-layer part.

The primary research issue in the building of the cladding is the relationships between process parameters and the resultant geometrical and material properties. The process parameters, whose influence on part fabrication can be analytically predicted or have already been reported in the literature [20, 21, 22], can be classified as follows:

- Laser-beam parameters:
  1. Working mode of the laser (i.e., pulsed or continuous);
  2. Power level;
  3. Diameter of the beam spot;
  4. Transverse electromagnetic mode (TEM) of the beam, which is a measure of the beam energy profile (i.e., intensity distribution). (For example, TEM<sub>00</sub> corresponds to Gaussian intensity distribution and TEM<sub>01</sub> to “doughnut” intensity distribution. Further increases in the subscript value are referred to as “multimode” distribution, or “top hat”, and can be approximated as constant energy distribution over the beam area, [1]); and,
  5. Pulse frequency and duration (for pulsed lasers)
- Scanning speed; and
- Preparation of the powder (e.g., preheating of powder and/or baseplate).

The geometrical properties of the cladding can be defined as:

- Cross-sectional height; and,
- Cross-sectional width.

The material properties of the cladding can be defined by:

- Density; and,
- Mechanical properties;

Determination of the cladding's density and mechanical properties requires building of tensile-test specimens, which cannot be achieved without an established procedure for the building of individual layers and parts. This issue is beyond the scope of this thesis.

### 2.2.1 Identification of Process Parameters

The objective of this research is to establish relationships between the main process parameters and the geometrical properties of the cladding. Since the process may be characterized by a large number of the parameters, it is important to identify those that have the greatest effect on the cladding's geometrical properties and their variability.

#### 2.2.1.1 Laser's Working Mode

Information on the influence of the laser working mode (i.e., continuous or pulsed) on the geometrical properties of the cladding could not be found in the literature. However, since pulsed-laser application is a cyclic event, where the heating of the powder is followed by a cooling period, and whereas continuous-laser application is a persistent heating of the powder, this difference in the working mode of the laser is anticipated to have a significant influence on the cladding's geometrical properties.

#### 2.2.1.2 Power Level and Diameter of the Laser Beam

The powder must absorb certain quantity of energy in order to melt. This energy can be characterized by the power level of the laser and its application time. In [23], it was shown that there exists a small working region for the value of the laser's irradiance,



which is the ratio of the power level to the beam's area, suitable for a particular RM process. When the irradiance is below the lower bound of this region, the metal does not melt, and when it is above the upper bound of this region, the metal vaporizes. Increasing vaporization of the metal leads to the initiation of the vaporization recoil pressure application, which leads to squirting of molten metal. This would cause increased variability in the cladding's geometrical properties.

In [24], it was shown that the increase in the laser's power level (with a constant beam diameter) mostly affects the depth of the molten zone, and does not affect significantly the width of the cladding. This implies that the power level of the laser (provided that its value is within the irradiance working region) does not have a significant effect on the cladding's geometrical properties.

The cladding's width is principally determined by the diameter of the laser beam [5]. However, in order to be able to build parts with small features and tight tolerances, it would be beneficial to minimize the beam diameter. Naturally, a decrease in the laser-beam diameter will result in a decrease of the volumetric build rate, significantly slowing the part-building process.

### 2.2.1.3 Pulse Frequency and Duration

No information could be found in the literature on the influence of the laser-beam's pulse frequency and duration on the cladding's geometrical properties. However, in this thesis, both will be assumed as parameters that significantly influence the fabrication process. (It can be noted that the continuous laser beam is the limiting case).

#### 2.2.1.4 Scanning Speed

Scanning speed for laser-based cladding has been reported in the literature to be a major process parameter [e.g., 11, 20]. Since the scanning speed defines the part-building time, it would be beneficial to maximize it. Thus, the relationship between scanning speed and geometrical properties of the cladding must be investigated.

#### 2.2.1.5 Other Parameters

Usually, industrial high-power lasers produce a beam with Transverse Electromagnetic Mode, corresponding to multimode power distribution [1]. Therefore, the influence of this process parameter on the cladding's geometrical properties is not considered in this study. The beam energy distribution is assumed to be constant over the beam's area.

Existence of an inert gas atmosphere is an essential condition to welding and cladding processes. The inert gas shields the high-melting-temperature metal against oxidation [1]. Since the inert gas affects only the material properties of the cladding, the investigation of its influence on the process was excluded from this study.

The shape and size of the powder particles affect the powder density, which would consequently have an effect on heat propagation [25]. However, due to small variations in densities for commercially available metal powders (i.e., from 35 to 55% of the base material density [25]), this material parameter was not considered in this thesis either.

Preheating the powder and/or the baseplate may also have an effect on the geometrical properties of the cladding [22]. However, due to the high complexity of the

necessary experimental setup needed to investigate this process parameter (i.e., heating system, use of high-temperature materials, etc.), it was also excluded from this thesis.

## **2.3 Methodology**

As stated earlier, this thesis' objectives are to be achieved through first mathematical modeling and computer simulations, followed by experiments.

### **2.3.1 Computer Simulation**

Mathematical modeling and computer simulations will be used herein to identify the functional relationships between the major process parameters and the cladding geometrical properties. The simulations will employ the finite-difference numerical method to determine the global temperature field in the powder-metal system, resulting from the application of the laser-beam energy. Knowledge of the global temperature field as a function of time will be used to determine the cladding's height and width. Two working modes of the laser (i.e., continuous and pulsed) will be modeled.

### **2.3.2 Experimental Verification**

A generic experimental set-up, independent of the operation mode of the laser, will be designed and built to verify the simulation results. Axiomatic Approach to Design [36], will be utilized in the experimental set-up design process. The setup will be used to produce claddings with varying process parameters. The claddings will be analyzed to identify their geometrical properties, such as height and width. The measurements will help to identify the functional relationships between major process parameters and cladding's geometrical properties, which will be compared to those obtained through computer simulations.

### 3. PROCESS SIMULATION

The overall objective of process simulation is to determine qualitative relationships between process parameters and single cladding line's geometrical properties - namely, its height and width. This can be accomplished by calculating the global temperature field within the powder and baseplate induced by the application of the laser beam. Modeling has been carried out for both laser light modes - continuous wave and pulsed.

The temperature-field calculation problem is a non-linear one due to materials' thermal properties' dependence on the temperature. Therefore, a numerical finite-difference method was employed in this thesis for the solution of the problem.

#### 3.1 Background Theory

##### 3.1.1 Heat Transfer

The three fundamental modes of heat transfer are conduction, convection and radiation [26]. Conduction is a process of energy transfer inside the body due to existence of a temperature gradient. The energy is transferred from the high-temperature region to the low-temperature region, where the heat-transfer rate per unit area is proportional to the temperature gradient. The proportionality coefficient is called the thermal conductivity of the material. Thus, the heat-transfer rate  $q$  is given by a one-dimensional Fourier's Law of heat conduction [26]:

$$q = -kA \frac{\partial T}{\partial x}, \quad (3.1)$$

where  $k$  is the thermal conductivity of the material (W/m K),  $A$  is the area ( $m^2$ ), and  $\frac{\partial T}{\partial x}$  is the temperature gradient in the direction of the heat flow.

The general 3D heat-conduction equation for a material's temperature-independent thermal properties is given as [26]:

$$\frac{\partial^2 T}{\partial x^2} + \frac{\partial^2 T}{\partial y^2} + \frac{\partial^2 T}{\partial z^2} + \frac{q_g}{k} = \frac{\rho c}{k} \frac{\partial T}{\partial t}, \quad (3.2)$$

where  $q_g$  is the amount of heat generated within the body,  $\rho$  is the density of the material ( $kg/m^3$ ),  $c$  is the specific heat of the material (J/kg K), and  $t$  is the time (s). In the case of temperature-dependent thermal conductivity, the heat-conduction equation is given as [13]:

$$\rho c \frac{dT}{dt} = k \nabla^2 T + Q + \frac{dk}{dT} \left\{ \left( \frac{dT}{dx} \right)^2 + \left( \frac{dT}{dy} \right)^2 + \left( \frac{dT}{dz} \right)^2 \right\} \quad (3.3)$$

where,  $\nabla^2 T = \frac{d^2 T}{dx^2} + \frac{d^2 T}{dy^2} + \frac{d^2 T}{dz^2}$ , and  $Q$  is the heat supplied to the material per unit time, per unit volume .

The process under investigation involves all fundamental modes of heat transfer, but the governing heat-transport phenomenon is conduction. Hence, for determination of the global temperature field in the system, consisting of the powder and the baseplate, Equation (3.3) must be solved. Due to the non-linearity of the problem (dependence of the thermal properties of the materials on temperature) and complex boundary conditions, a numerical method, such as a finite-difference method, must be employed.

### 3.1.2 Finite-Difference Method

In the finite-difference technique, the body is represented as a nodal network rather than one single object. For transient problems, where the boundary conditions change with time, time is also divided into finite increments. Continuous boundary conditions (such as heat loads, convection and radiation) are distributed between the nodes. The objective is to calculate the temperature at the points of nodal network within the body using Equation (3.3) as the governing condition. For simplification purposes, only the two-dimensional formulation is provided in this section.

Assuming a linear temperature function between the nodes, differential increments in temperature and 2D space coordinates can be approximated as follows,

Figure 3.1 [26]:

$$\left. \frac{\partial T}{\partial x} \right|_{m+1/2,n} \approx \frac{T_{m+1,n} - T_{m,n}}{\Delta x}, \quad (3.4)$$

$$\left. \frac{\partial T}{\partial x} \right|_{m-1/2,n} \approx \frac{T_{m,n} - T_{m-1,n}}{\Delta x}, \quad (3.5)$$

$$\left. \frac{\partial T}{\partial y} \right|_{m,n+1/2} \approx \frac{T_{m,n+1} - T_{m,n}}{\Delta y}, \quad (3.6)$$

$$\left. \frac{\partial T}{\partial y} \right|_{m,n-1/2} \approx \frac{T_{m,n} - T_{m,n-1}}{\Delta y}, \quad (3.7)$$

$$\left. \frac{\partial^2 T}{\partial x^2} \right|_{m,n} \approx \frac{\left. \frac{\partial T}{\partial x} \right|_{m+1/2,n} - \left. \frac{\partial T}{\partial x} \right|_{m-1/2,n}}{\Delta x} = \frac{T_{m+1,n} + T_{m-1,n} - 2T_{m,n}}{(\Delta x)^2}, \quad (3.8)$$

$$\left. \frac{\partial^2 T}{\partial y^2} \right|_{m,n} \approx \frac{\left. \frac{\partial T}{\partial y} \right|_{m,n+1/2} - \left. \frac{\partial T}{\partial y} \right|_{m,n-1/2}}{\Delta y} = \frac{T_{m,n+1} + T_{m,n-1} - 2T_{m,n}}{(\Delta y)^2}. \quad (3.9)$$

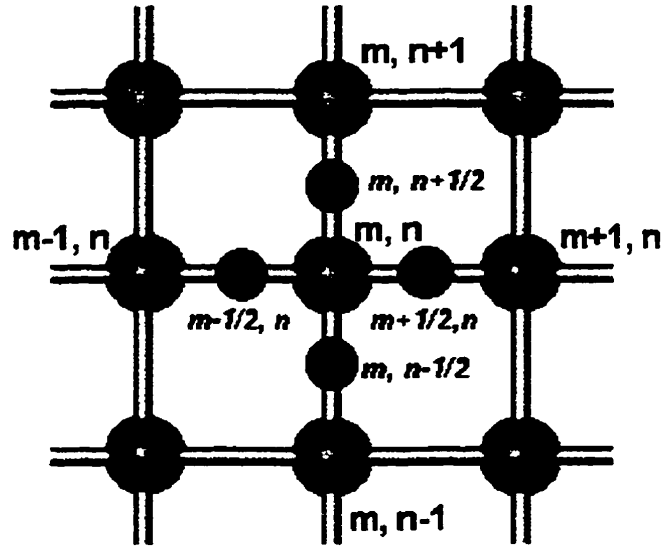


Figure 3.1. Nomenclature Used in Two - Dimensional Finite-Difference Analysis of Heat Conduction.

The time increments are approximated as follows [26]:

$$\frac{\partial T}{\partial t} \approx \frac{T_{m,n}^{p+1} - T_{m,n}^p}{\Delta t} \quad (3.10)$$

where  $T_{m,n}^{p+1}$  is the temperature at node  $(m, n)$ , at the time point  $p+1$ , and  $T_{m,n}^p$  is the temperature at node  $(m, n)$ , at the time point  $p$ .

Substitution of Equations (3.8), to (3.10) into the 2D version of Equation (3.3) results in an expression of temperature for node  $(m, n)$ , at time point  $p+1$ , in terms of the temperatures of points surrounding it, at time point  $p$ . Therefore, by generating such expressions for each point in the 2D space and adding boundary conditions, such as heat loads, convection and radiation, the system of equations can be solved sequentially for each time step. The 3D problem can be handled using the same methodology, by simply adding the terms corresponding to the third dimension [26].

The nodal finite-difference equations, based on Equations (3.4) through (3.10) are called *explicit* expressions, because the nodal temperatures,  $T_{m,n}^{p+1}$ , are written explicitly in terms of the previous nodal temperatures,  $T_{m,n}^p$ . In this case, the calculation proceeds from one time step to another until the final time point is reached. This technique is called *the forward-difference method*.

It must be noted here that there exists a limiting criterion for the finite-difference solution [23]. For example, for the two-dimensional problem this criterion is written as follows:

$$\Delta t < \frac{(\Delta x \Delta y)(c / V_m k)}{4}, \quad (3.11)$$

where  $V_m$  is the molar volume of the material ( $\text{m}^3/\text{mole}$ ). Equation (3.11) limits the values of the time step, once a specific increment in 2D space has been chosen.

The finite-difference equations can also be formulated by computing the space derivatives in terms of the temperatures at time increment  $p+1$ . In this case, the complete set of expressions must be written for the overall nodal network and solved simultaneously to determine the temperatures  $T_{m,n}^{p+1}$ . This technique is called *the backward-difference method*. The advantage of the backward-difference technique is that it has no restrictions on time step. The disadvantage is that, it requires a larger number of calculations for each time step.

### 3.1.3 Thermal-Modeling Software

In order to perform a mathematical modeling of our heat-transfer process, a commercial finite-difference software package, such as I-DEAS TMG can be used [27].



This package uses a control-volume finite-difference technique with available forward, backward, and forward-backward solvers.

The control-volume finite-difference technique involves geometrical discretization, or meshing, of the model into control-volume regions and establishing a calculation point within each region. Heat-balance equations are established for each of these control volumes. The governing heat-balance equation for a control volume is as follows [27]:

$$\int_A q_n dA + \int_V q_0 dV = \int_V \rho c \frac{\partial T}{\partial t} dV, \quad (3.12)$$

or:

$$Q_n + Q_g = \frac{\partial U}{\partial t} \quad (3.13)$$

where  $q_n$  is the heat-flow rate across the control volume boundaries,  $q_0$  is the heat generation rate within the control volume,  $Q_n$  is the heat flow across the control volume boundaries,  $Q_g$  is the heat generated within the control volume,  $U$  is the energy stored within the region, and  $V$  is the volume. The term  $C = \rho c V$  in Equation (3.12) is called capacitance of the control volume.

The heat flow across the boundary between adjacent control volumes,  $i$  and  $j$ , is characterized by a linear conductive conductance  $G_{ij}$ :

$$Q_{n_{ij}} = G_{ij} \times (T_i - T_j) \quad (3.14)$$

where  $T_i$  and  $T_j$  are the temperatures of the control volumes  $i$  and  $j$ , respectively. The radiative and convective conductances are non-linear and involve more complicated functions of temperature.

The I-DEAS TMG module automatically calculates accurate finite-difference capacitances and conductances for arbitrary element meshes. For each element in the

model, the calculation points are established at the centroids and boundaries of the element. Conductances are established between the boundary points using an algorithm that constrains a linear-element temperature function to satisfy the governing differential equation for conduction. The centroidal point is used to compute distributed heat transfer, such as radiation and convection. For each time step, the material's thermal properties are considered to be constant within the control volume and are changed for the next time-step calculation.

In order to evaluate the applicability of the I-DEAS software to our process, a verification test was performed. A heat-transfer problem related to welding, for which an analytical solution exists [12], was solved. The results of the analytical and numerical solutions were compared.

The problem considered is determination of the global temperature field within a metallic material with constant thermal properties, induced by the application of a momentary stationary heat point source [12]. This problem may be considered as a possible approximation of the short-time heating and subsequent cooling of the material, e.g., a pulsed-laser welding.

The heat quantity,  $q$ , is considered to be applied at time  $t = 0$ , momentarily (duration of the pulse application  $\Delta t = 0$ ), at the center of a semi-infinite solid, and heat propagates in three dimensions. No convection or radiation is considered. The temperature increase,  $T - T_0$ , at an arbitrary distance  $R$  from the point source, at time  $t$ , is defined by [12]:

$$T - T_0 = \frac{2q}{\rho c (4\pi\alpha t)^{3/2}} e^{-R^2/4\alpha t}, \quad (3.15)$$

where  $\alpha = k/\rho c$  is the thermal diffusivity of the material ( $\text{m}^2/\text{s}$ ).

At the start of the process,  $t=0$ , the temperature at the source is infinitely high, (which is a consequence of its simplification as a point source), and then drops hyperbolically.

For the solution of the problem using I-DEAS, the body was meshed using 3D solid elements. The parameter values for the problem are given in Table 3.1. The body can be considered semi-infinite, if the heat-wave propagation length,  $l_{hw}$ , is much smaller than the dimensions of the body [28]:

$$l_{hw} = (\alpha t)^{1/2}. \quad (3.16)$$

In our case,  $t < 5$  s, which yielded  $l_{hw} \approx 6$  mm, whereas the dimensions of the body, modeled in I-DEAS were 100 x 100 x 100 mm.

The heat transmission was modeled as a pulse with duration of  $10^{-7}$  s and of power of  $2.1 \times 10^{10}$  W, which gives a total pulse energy of 2,100 J.

Table 3.1. Values of the Parameters for the Short Pulse-Application Problem.

$k$ (J/mK)	$\rho c$ (J/m <sup>3</sup> K)	$\alpha$ (m <sup>2</sup> /s)	$q$ (J)	$T_0$ (K)
42	$4.2 \times 10^6$	$10^{-5}$	2100	273

The temperature values for different distances, from the application point of the heat source, are shown in Figure 3.2 for different times after the pulse. The dashed lines show results of the problem solution yielded by I-DEAS, and the solid lines show analytical solutions using Equation (3.15). From our extensive simulations, it was

concluded that the numerical method yields very close results to those obtained by analytical method. Thus, it can be used with high confidence in our process simulations.

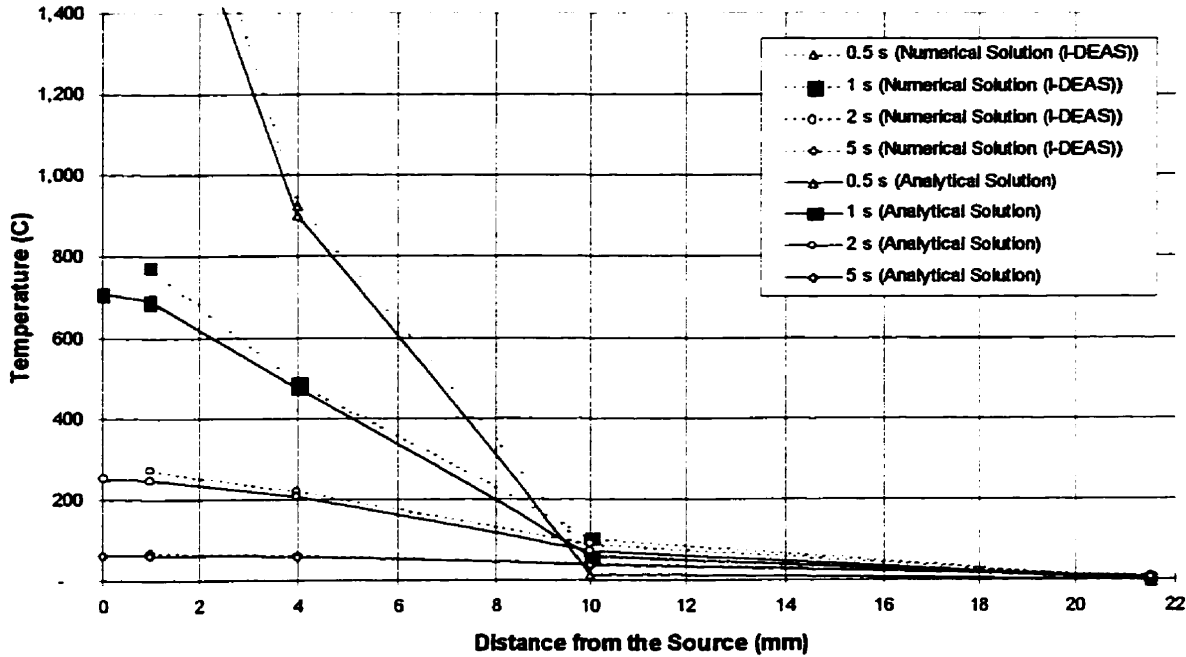


Figure 3.2. Temperature Field Around Impulse Point Source. Analytical and Numerical Solutions

### 3.2 Process Model

#### 3.2.1 Description of the Process Model

The general purpose of modeling a physical phenomenon is to computer simulate it under varying conditions. However, the governing phenomenon of our process - heat transfer, is a very complex one, and thus, difficult to formulate. A possible simplification would be use of approximations in the calculation domain, as discussed below.

The proposed model comprises a three-material system (i.e., powder, baseplate, and surrounding gas). Although the thermal properties of solid stainless steel are well-known [29] and can be used to model the baseplate, the same is not true for its powder

form. Therefore, in this thesis, the powder was modeled as a solid material with thermal properties different than those of the baseplate [32].

Also, in the mathematical model, only half of the object space was used due to the symmetry of the problem along the laser scanning path, Figure 3.3. The dimensions of the plate were kept as minimal as possible in order to minimize the number of elements in the FEA model. Using Equation (3.16), it can be shown that these dimensions, however, are sufficient for our plate to be considered as a semi-infinite object.

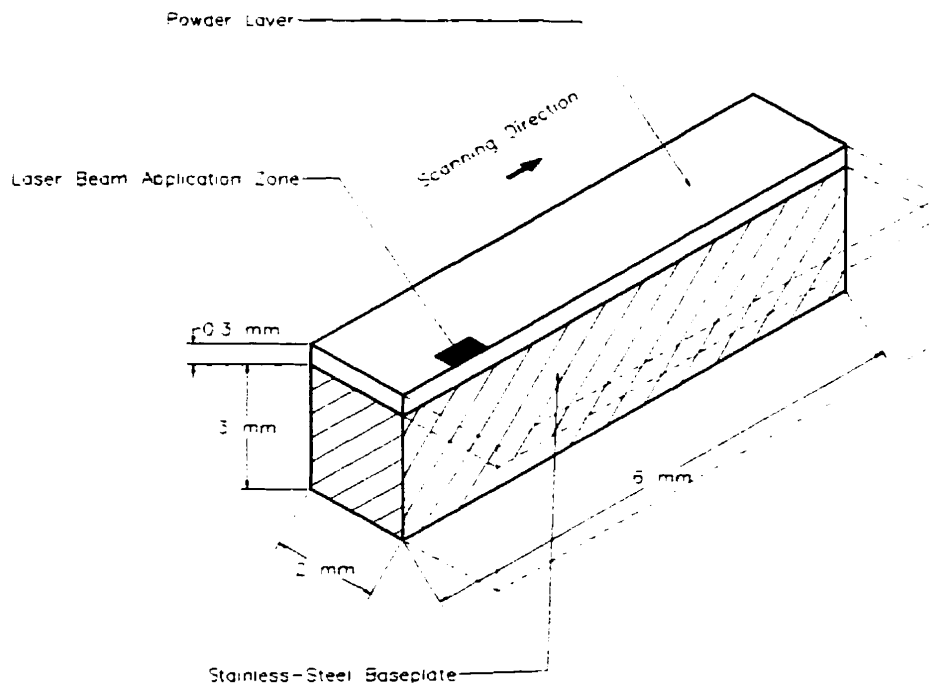


Figure 3.3. Model of Physical Set-Up.

The model in Figure 3.3 was meshed using 3D rectangular solid elements with dimensions of 0.125 x 0.125 mm in length and width, and depth of 0.15 mm for the powder layer, and variable depths of 0.2 mm to 1.4 mm for the baseplate (the thinner elements were located near the baseplate's upper region for better resolution). In order to

apply a heat load onto the powder surface, and to be able to model convection and radiation, the model was augmented with “surface-coating elements”. These are 10  $\mu\text{m}$  elements, as used by I-DEAS, which cover free surfaces of solid elements and share boundary nodes with them.

The laser beam was modeled as being perpendicular to the top surface of the baseplate, possessing 200 W power for the pulsed mode and 50 W for the continuous mode (half-spot values). These values were chosen based on experiments reported in [11, 24]. The heat load is evenly distributed over a rectangular area with dimensions of 0.25 x 0.5 mm (2 x 4 elements) in order to approximate the semi-circular part of the multi-mode laser spot of 0.5 mm diameter.

### 3.2.2 Calculation of Powder’s Thermal Properties

The following material parameters are needed to determine the global temperature field in any modeled system:

- Thermal conductivity,
- Specific Heat, and
- Density.

The first two are strong functions of temperature, as shown in Figures 3.4 and 3.5, [29, 30].

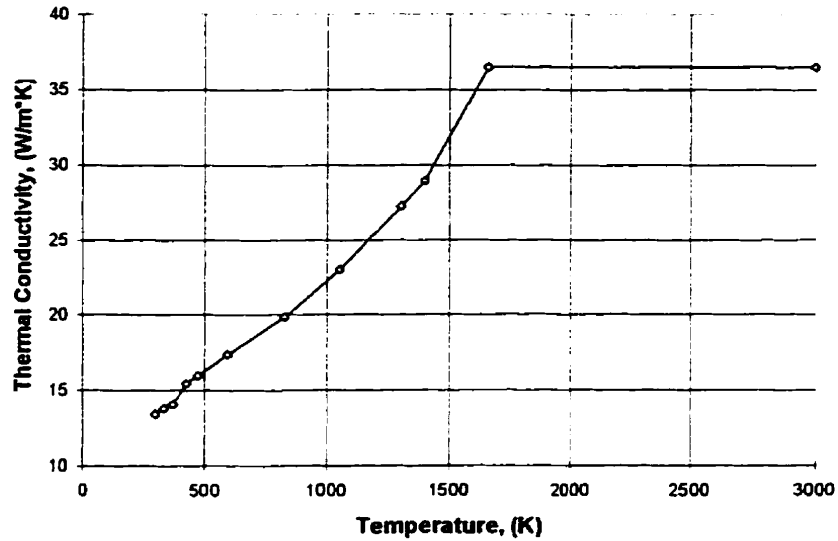


Figure 3.4. Thermal Conductivity versus Temperature for AISI 316 Stainless Steel.

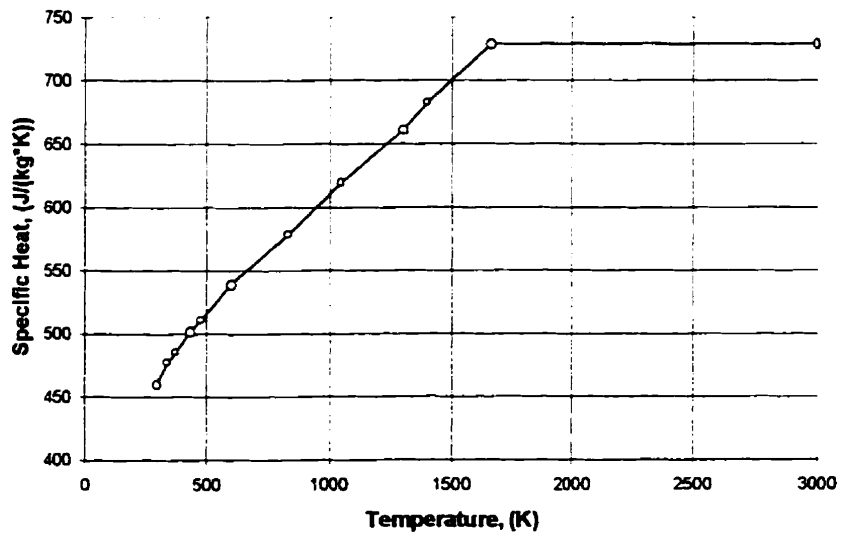


Figure 3.5. Specific Heat versus Temperature for AISI 316 Stainless Steel.

For stainless-steel powder the values for the above three parameters, could not be found in the literature. Thus, the density of the powder was first simply determined experimentally by weighing known volumes of water-atomized AISI 316 stainless-steel powder, with particle size less than 45  $\mu\text{m}$  (manufacturer's specification), produced by GoodFellow Inc., UK. The average density of the powder was noted as 2.95  $\text{g/cm}^3$ .

Accordingly, the volume fraction of the powder's density to solid stainless steel density is 1:2.7. Subsequently, the specific heat of the powder,  $c_m$ , was determined assuming a mixture of two components (stainless steel and argon) [31]:

$$c_m = \frac{\rho_1 c_1 \gamma_1 + \rho_2 c_2 \gamma_2}{\rho_1 \gamma_1 + \rho_2 \gamma_2}, \quad (3.17)$$

where  $c_1, c_2$  are the specific heats of the first component and of the second component, respectively,  $\rho_1, \rho_2$  are the densities of these two constituent components, and  $\gamma_1, \gamma_2$  are their volume fractions. Since the density of the argon is much smaller than the density of the stainless steel, the relationship between the powder's specific heat and temperature would be almost identical to that of solid stainless steel.

A suitable way to determine the powder's thermal conductivity would be to assume that the powder is a packed-bed object consisting of an infinite number of hard spheres. Based on this, the powder can be thought of as a regular dispersion of stainless steel spheres in a continuous medium (in our case, argon). Therefore, the thermal conductivity of the powder was calculated herein as follows [32]:

$$K = 1 + \frac{3\phi}{1 - \phi - \frac{1.306\phi^{10/3}}{1 - 0.4072\phi^{7/3}} - 0.07296\phi^{14/3}}, \quad (3.18)$$

where  $\phi = \varepsilon\beta$ ,  $\varepsilon$  is the volume fraction of dispersed phase (steel),  $\beta = \frac{\frac{k_d}{k_c} - 1}{\frac{k_d}{k_c} + 2}$ ,  $k_d$  is the

thermal conductivity of the dispersed phase, and  $k_c$  is the thermal conductivity of the continuous phase (argon).



After reaching the melting point temperature (which in our case is 1658 K, or 1385 °C), the powder becomes molten stainless steel, and has the same thermal properties of a solid object of the same material. The thermal conductivity of the powder as a function of temperature calculated according to Equation 3.18 is shown in Figure 3.6.

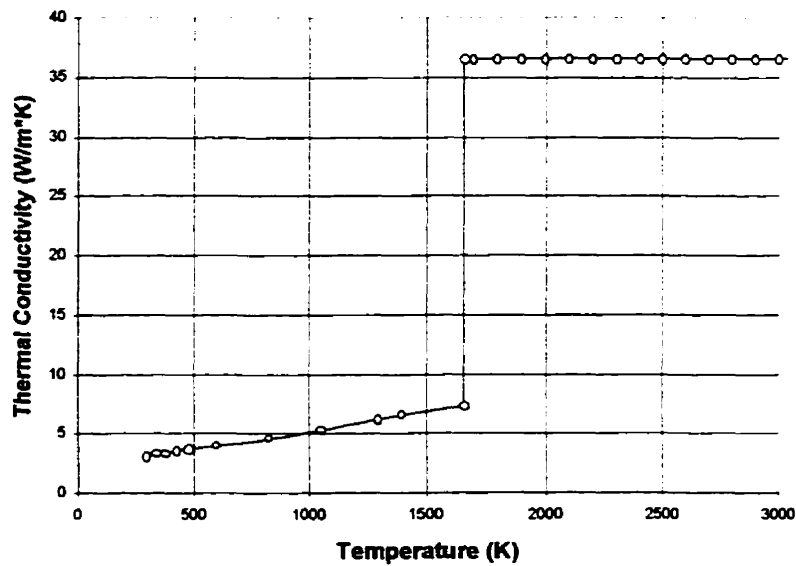


Figure 3.6. Thermal Conductivity versus Temperature for AISI 316 Stainless Steel Powder.

### 3.3 Thermal-Modeling Procedure

For the proposed process, the powder as well as the baseplate undergo a phase change from solid state to liquid state and then back to solid. This phase change is associated with latent heat - the amount of energy stored in the material and used to change its state, which is not used for increasing its temperature. However, it can be shown that the amount of energy consumed for phase change is less than 5% of total energy supplied to the material [29]. Thus, for simplification purposes, the latent heat was excluded from our calculations.

### 3.3.1 Pulsed Laser

As mentioned in Section 3.2.1, the model of the baseplate and the powder layer is discretized for use with a finite-difference method. Hence, the continuous motion of the pulsed laser must be also discretized in (scanning-) time space.

The laser beam's pulsing parameters are assumed to be as follows: a pulsing time of 2.5 milliseconds and a pulsing rate (frequency) of 14 Hz (corresponding to the pulsing parameters of the actual laser used in our experiments). Thus, a pulsing cycle (i.e., the pulse itself and the time delay until the next pulse) is equal to 71 ms - 2.5 ms for the pulse and 68.5 ms for the delay.

The scanning procedure is as follows:

1. The laser pulse is applied at the first location onto the top surface of the powder for 2.5 ms. The heat-load application point for each element of the 8-element laser-beam spot model is located at the centers of the individual elements.
2. (a) The laser application is stopped at the end of the 2.5 ms and heat dissipation takes place for 68.5 ms.
2. (b) The laser-beam spot is moved by an integer number of elements, calculated based on the scanning speed, in the scanning direction and Steps (1) and (2) are repeated.

Three scanning speeds were used in our simulations: 1.76 mm/s, 3.52 mm/s, 5.28 mm/s. These correspond to the shift of the laser-beam spot by one, two, and three lengths of an element per cycle, respectively, Figure 3.7. A further increase in speed for our particular pulsing frequency would result in adjacent pulses not overlapping. In practice, this introduces discontinuities in the cladding and large variations in its shape properties.

For comparison purposes, the analysis was also performed for a 33 Hz pulsed laser with a 2.5 ms heat application period. Two corresponding scanning speeds were considered: 4.16 mm/s and 8.32 mm/s.

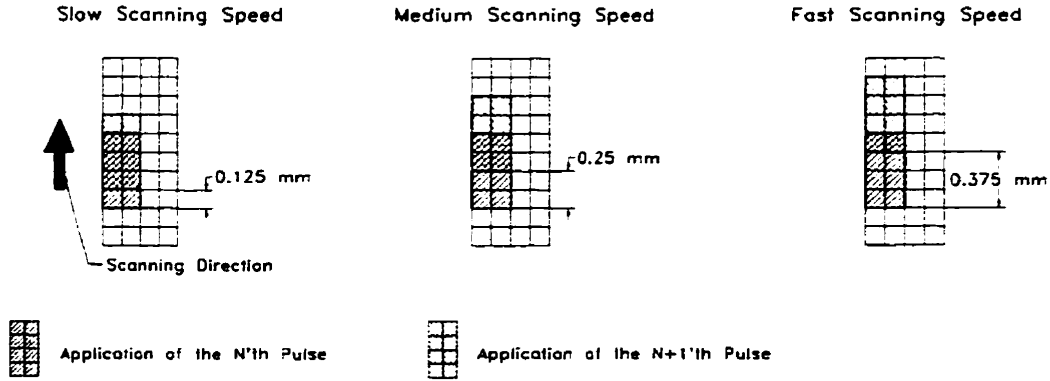


Figure 3.7. The Scheme of the Laser Beam Scanning Model for the Pulsed Laser.

### 3.3.2 Continuous Laser

The I-DEAS module permits the definition of a heat load as a function of time. This specific feature was used for the modeling of the continuous-laser-beam scanning considered in this thesis. In this case, the laser beam moves with a constant speed, crossing an element from one side to another in a specific period of time,  $\Delta t$ . Hence, the scanning speed is equal to:

$$V_{ss} = \frac{d}{\Delta t}, \quad (3.19)$$

where  $d$  is the length of the element.

The heat load is once again applied at the center point of the element. Therefore, continuous-laser-beam scanning can be represented as a decrease, or an increase, in the heat load for a specific element that is currently scanned by the laser beam, Figure 3.8.

When a rectangular strip of 4 x 2 elements is completely covered by the laser beam, each element in the strip receives one-eighth of the 50 W total load, namely 6.25 W. The applied complete heat load for elements #1, #3, and #5, as shown in Figure 3.8 are plotted in Figure 3.9. (a-c), respectively, as a function of time.

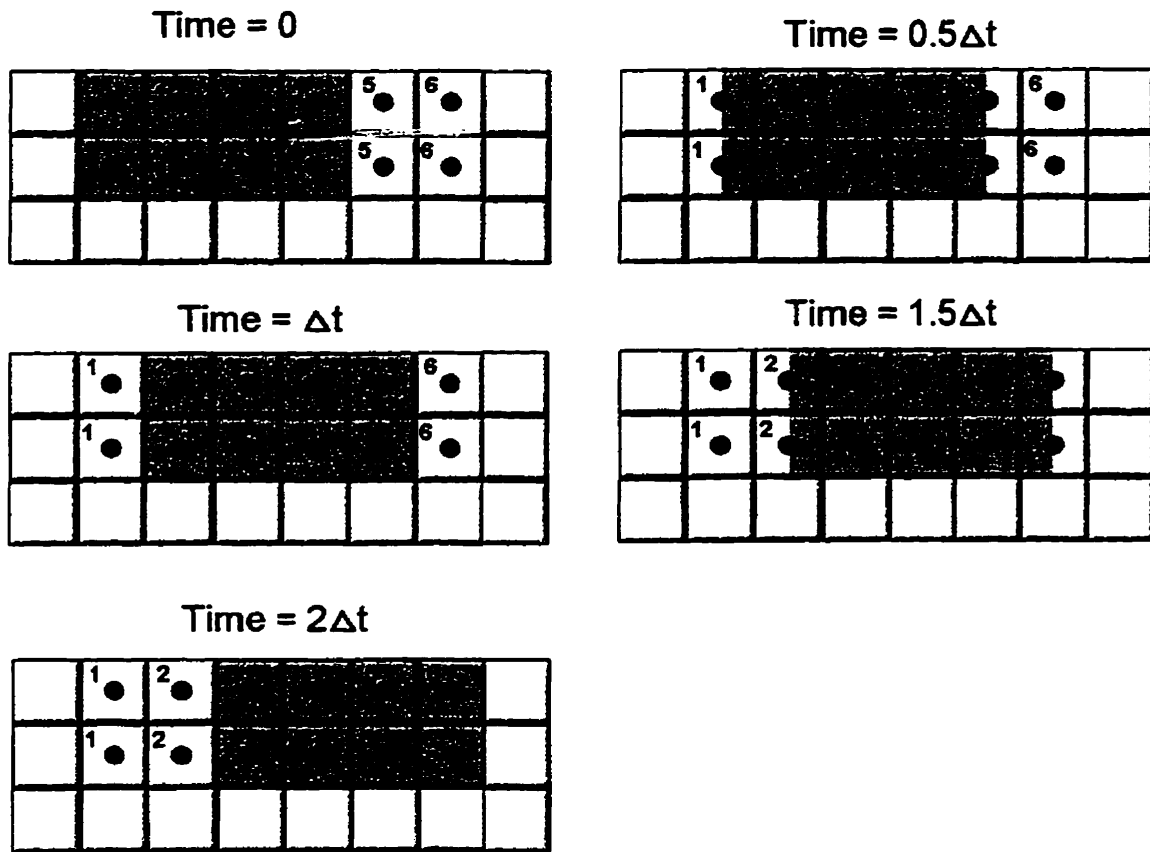
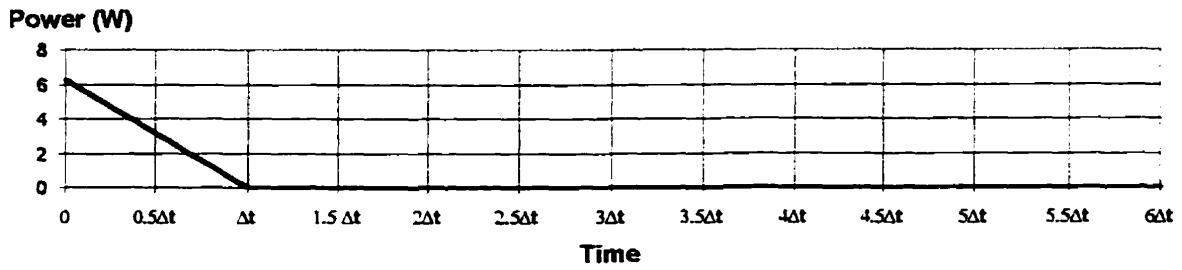
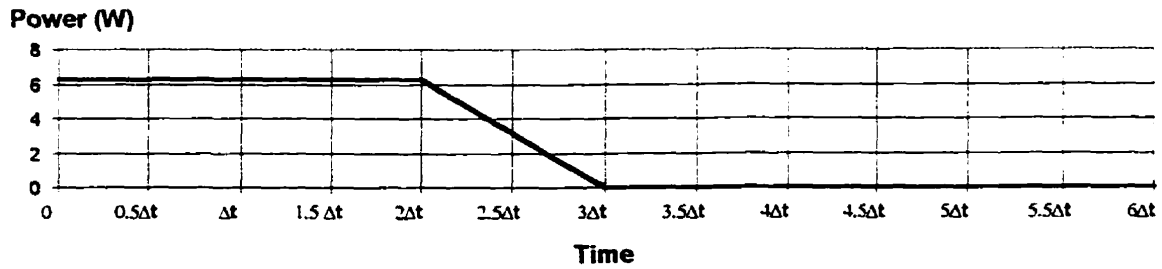


Figure 3.8. Laser-Beam Spot Model for Continuous Laser.

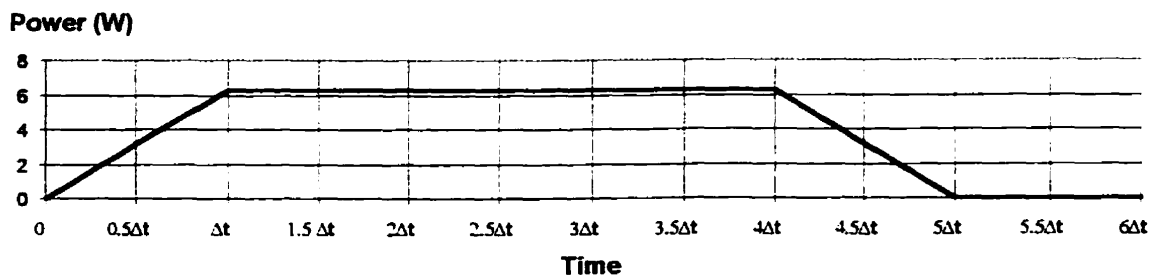
Four scanning speeds were considered for continuous-laser-beam simulation: 0.75 mm/s, 1.76 mm/s, 3.52 mm/s, and 7.04 mm/s. These yield  $\Delta t = 167$  ms, 70 ms, 35.5 ms, and 17.75 ms, respectively.



(a)



(b)



(c)

Figure 3.9. Heat Load Input for Continuous-Laser Simulation for: (a) Elements #1, (b) Elements #3, and (c) Elements #5.

### 3.4 Heat-Transfer Analysis Simulation Results

The forward-difference solver of I-DEAS was used for the heat-transfer analysis since it is superior to backward and forward-backward solvers in terms of computational time [26]. The value of calculation's time step was chosen as half of the maximum permissible time step, where the latter was determined by the software module based on

the 3D version of Equation (3.11), as  $3.5 \times 10^{-3}$  ms. The initial temperature of the model was assumed to be 20 °C.

The analysis is stopped, for the both modes of the laser beam, when the process reaches a “steady state”. The criterion for the steady-state condition is defined as achieving a difference of less than 1 °C between the maximum temperatures noted on the powder's top surface for two adjacent pulses.

The output of the thermal analysis consists of data files containing two temperature values, for all the nodes of the model:

1. One immediately after the current pulse application, and
2. Another just before the next pulse application.

For the pulsed laser, the longitudinal temperature profiles (Figure 3.10) for different scanning speeds are shown in Figures 3.11 to 3.13. These figures show temperature values for different locations on the model at the end of different pulsing cycles (i.e., 71 ms each): the top surface of the powder layer, the mid-layer-surface (hereafter referred to as the mid-surface) of the powder layer, and the top surface of the baseplate. The zero on the X-axis corresponds to the center of the first pulse application.

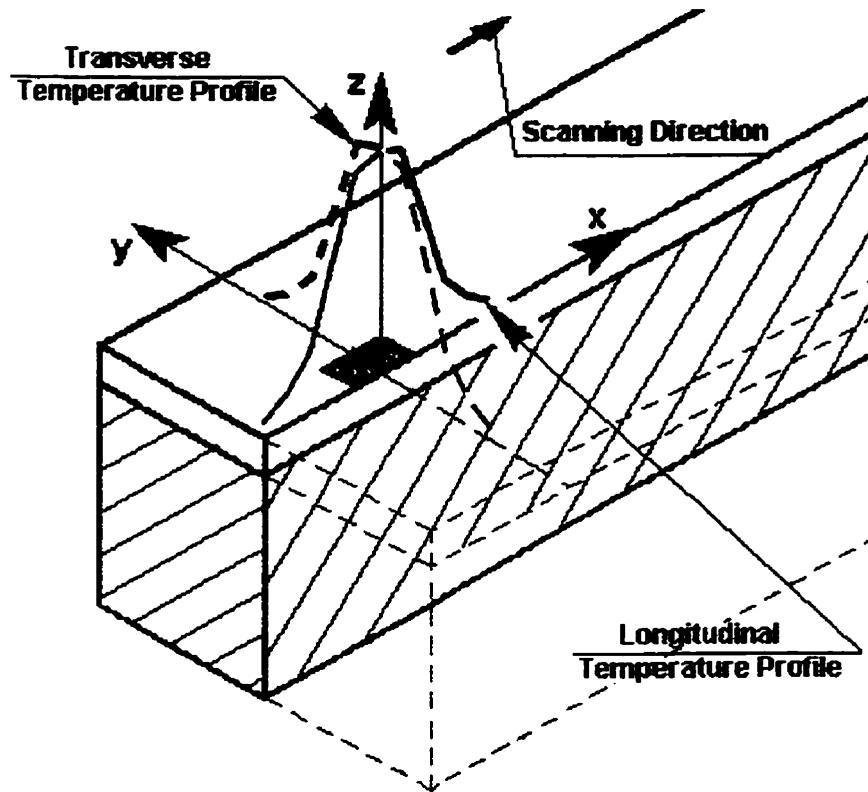


Figure 3.10. Definition of Longitudinal and Transverse Temperature Profiles.

As seen from Figures 3.11-3.13, for all scanning speeds considered, the thermal process reached a steady-state on the top surface of the powder after the application of the sixth pulse, independently of the scanning speed. On the top surface of the baseplate, the process reached a steady state after the seventh pulse.

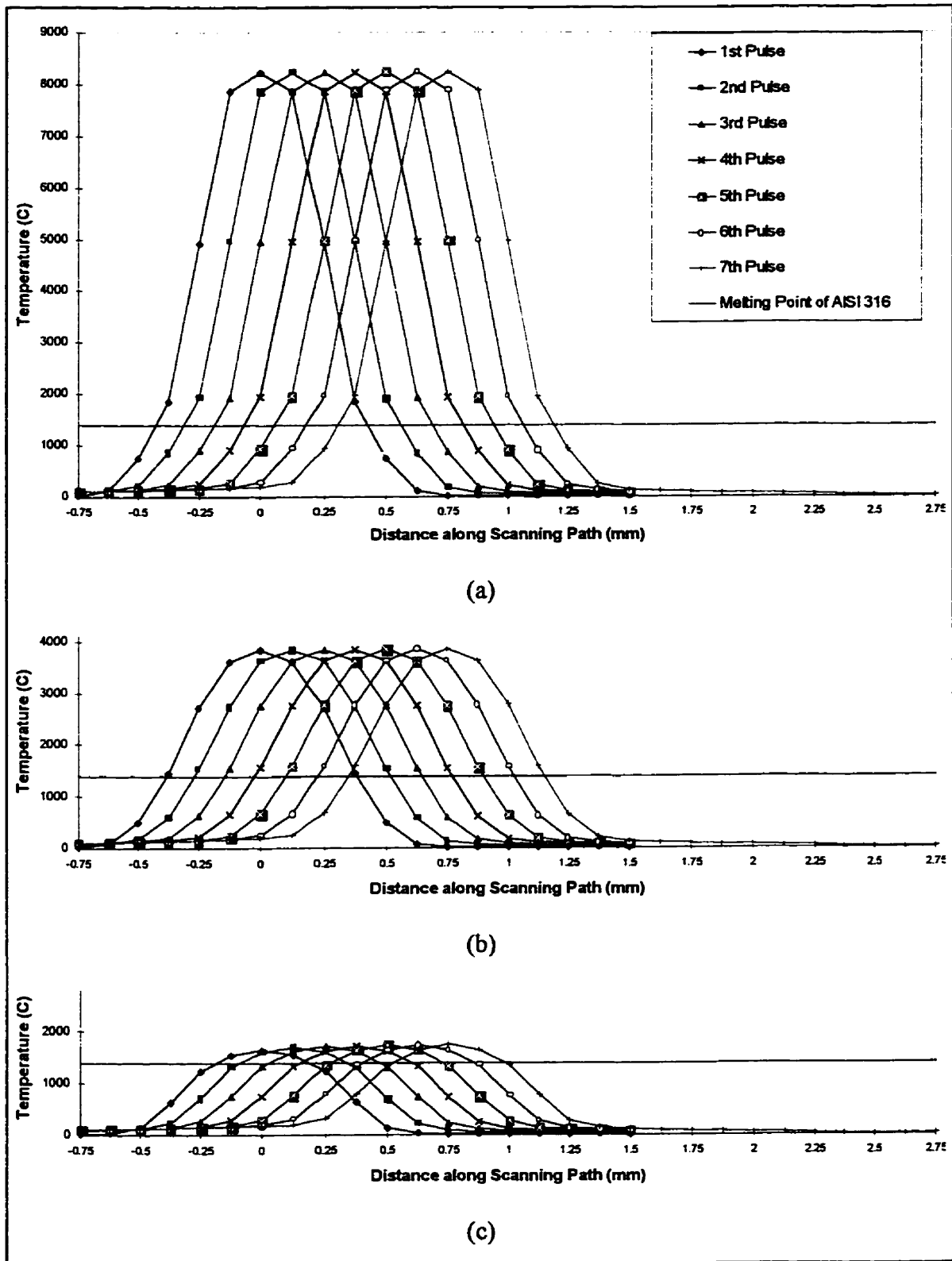


Figure 3.11. Longitudinal Temperature Profiles at (a) the Top Surface of the Powder, (b) the Mid-Surface of the Powder, and (c) the Top Surface of the Baseplate. Pulsed Laser. 1.76 mm/s Scanning Speed.



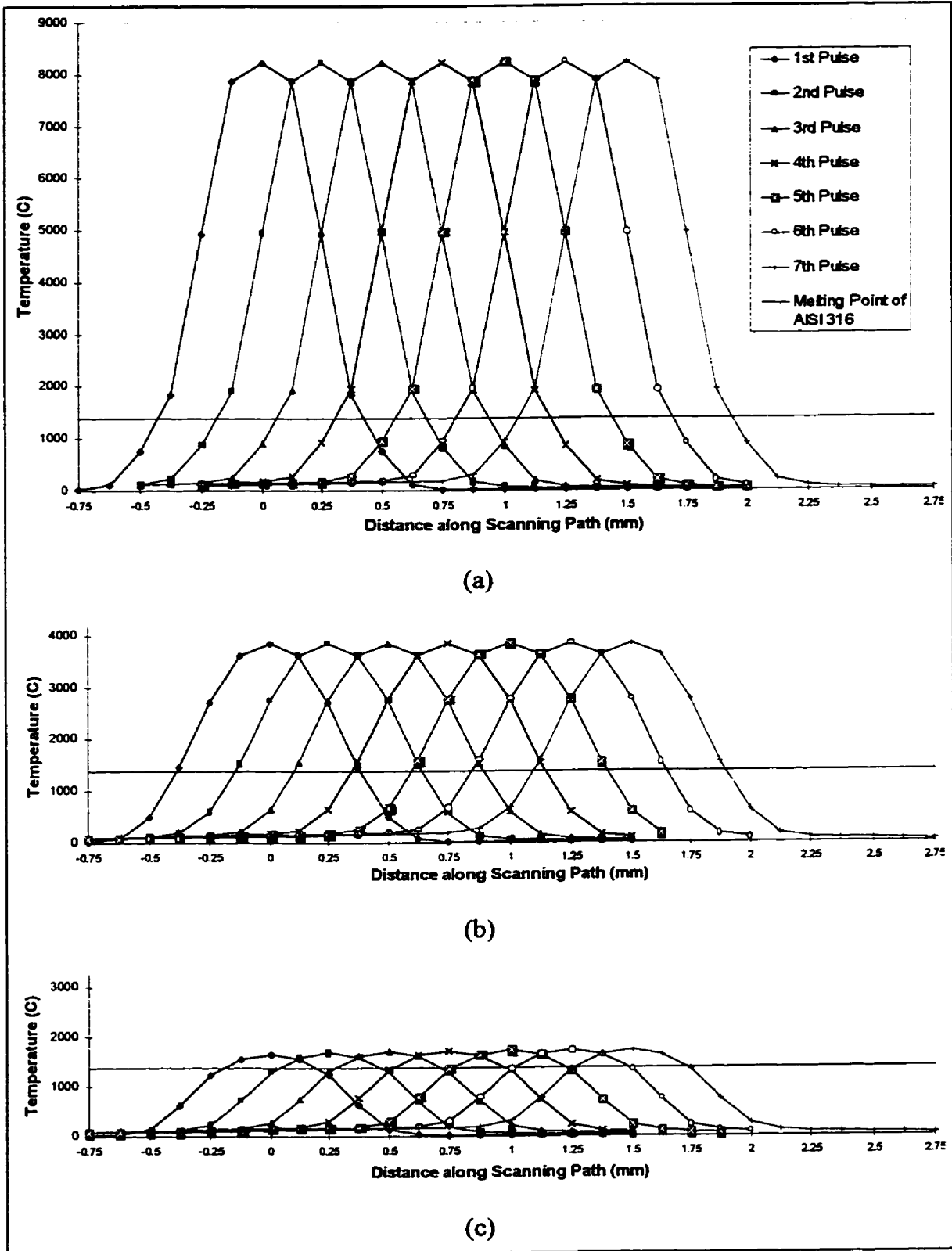


Figure 3.12. Longitudinal Temperature Profiles at (a) the Top Surface of the Powder, (b) the Mid-Surface of the Powder, and (c) the Top Surface of the Baseplate. Pulsed Laser. 3.52 mm/s Scanning Speed.

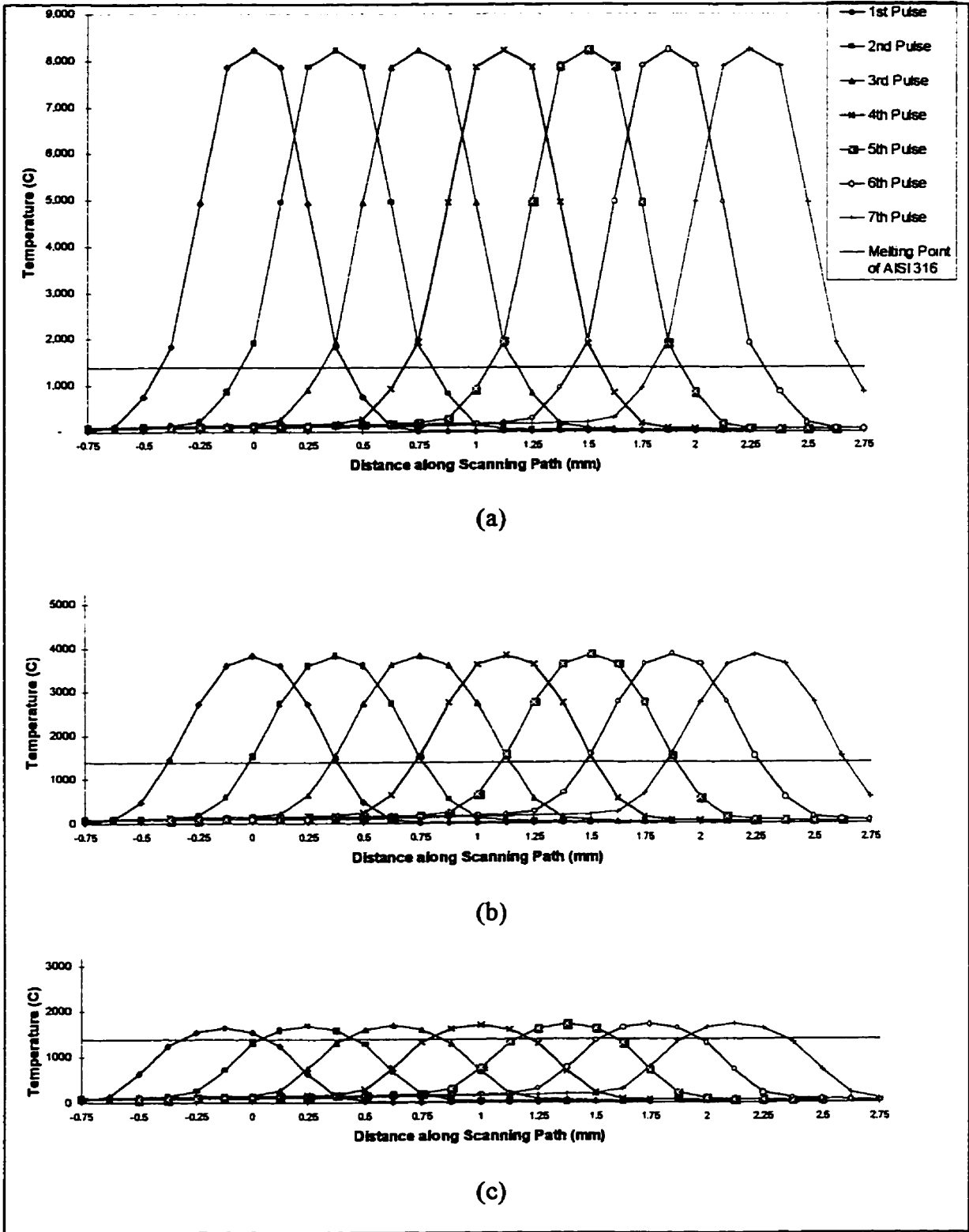


Figure 3.13. Longitudinal Temperature Profiles at (a) the Top Surface of the Powder, (b) the Mid-Surface of the Powder, and (c) the Top Surface of the Baseplate. Pulsed Laser. 5.28 mm/s Scanning Speed.

Figure 3.14, (a)-(c) show the thermal cycles, experienced by the three points located at the center of the first pulse application ( $x = 0, y = 0$ ) different  $z$  locations, namely at the top and mid-surfaces of the powder and at the top surface of the baseplate, respectively. The horizontal line represents the melting point of AISI 316 stainless steel.

The longitudinal temperature profiles for various scanning speeds for a continuous laser are shown in Figures 3.16-3.18. For the continuous laser, the process reached a steady state after 668 ms, 710 ms, 355 ms, and 177.5 ms for 0.75 mm/s, 1.76 mm/s, 3.52 mm/s, and 7.04 mm/s scanning speeds, respectively. For this laser operation mode the typical transverse temperature profiles (as defined in Figure 3.10) are given in Figure 3.19 at steady-state process conditions. One can note that only half of these profiles (+Y, +Z) are shown due to symmetry.

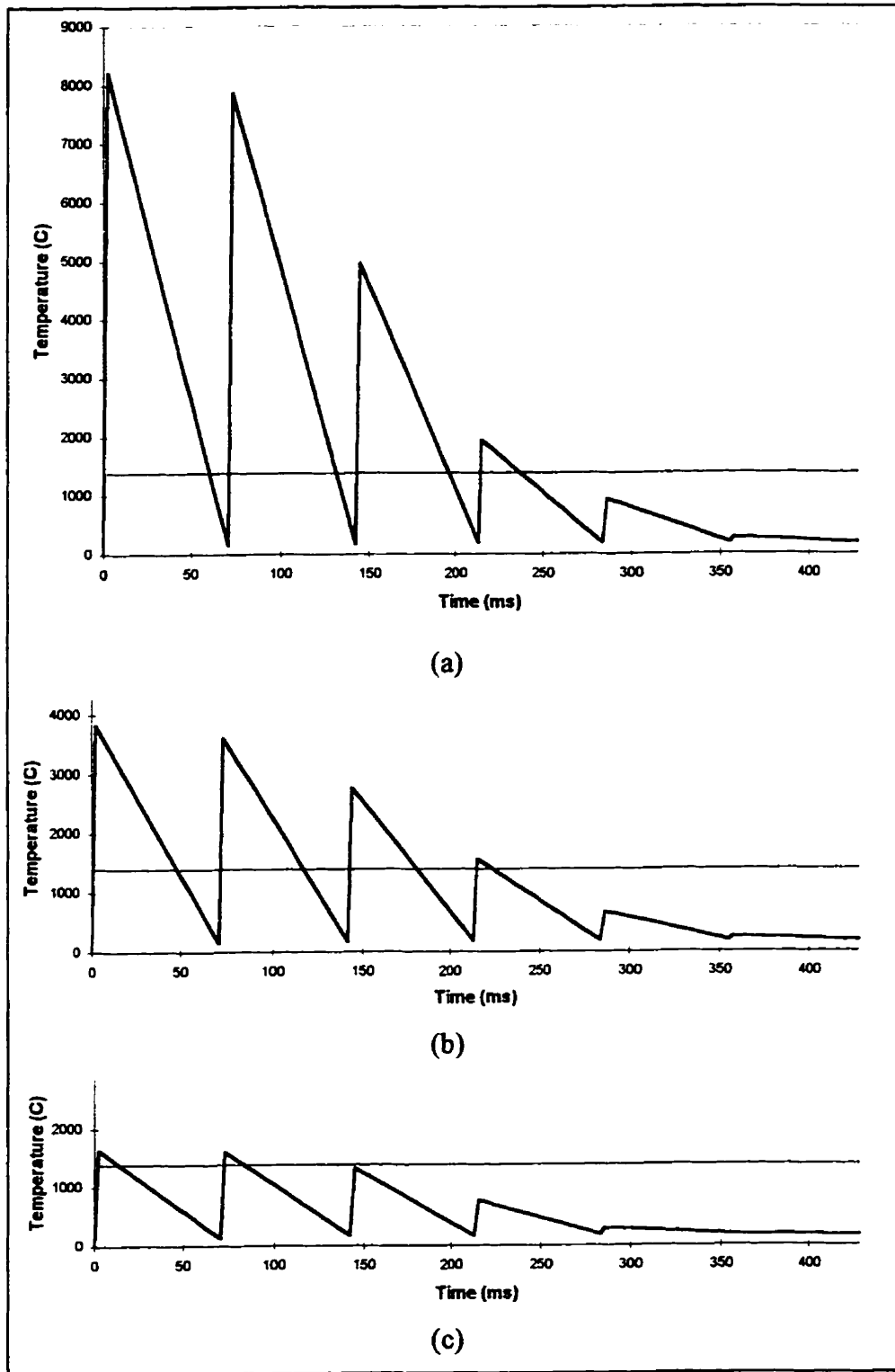


Figure 3.14. Thermal Cycles at Points on (a) the Top Surface of the Powder, (b) the Mid-Surface of the Powder, and (c) the Top Surface of the Baseplate. Pulsed Laser. 1.76 mm/s Scanning Speed.

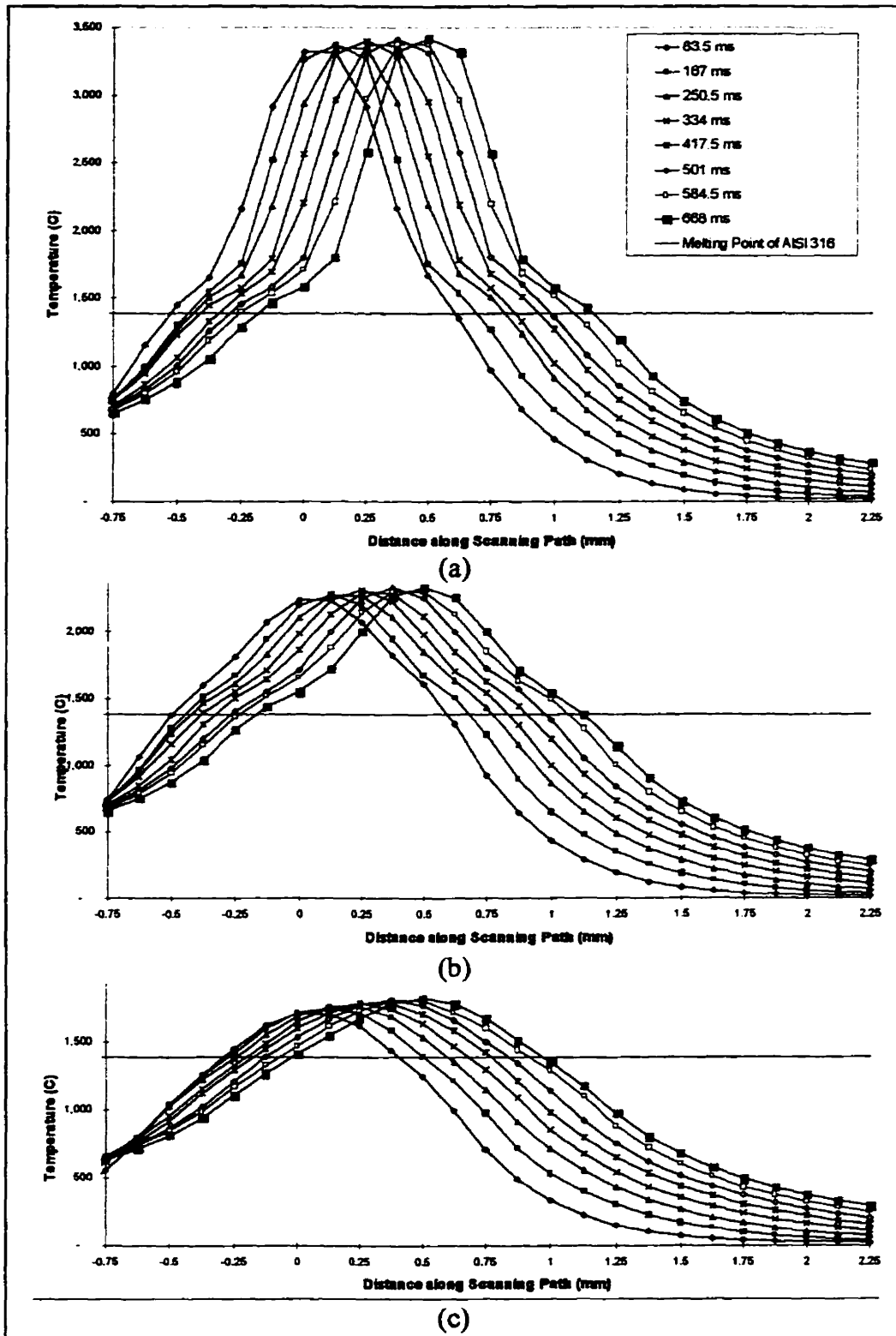


Figure 3.15. Longitudinal Temperature Profiles at (a) the Top Surface of the Powder, (b) the Mid-Surface of the Powder, and (c) the Top Surface of the Baseplate. Continuous Laser. 0.75 mm/s Scanning Speed.

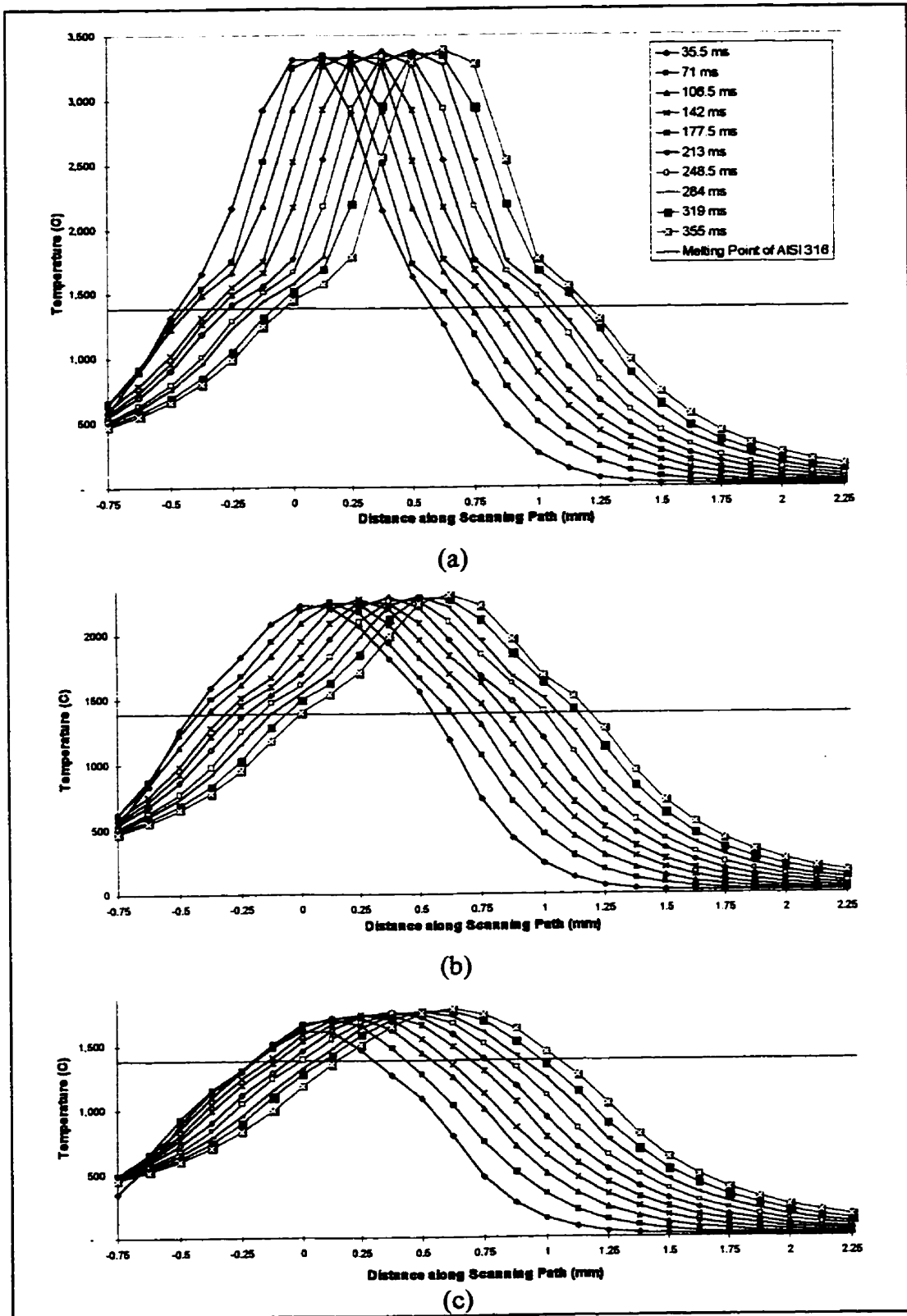


Figure 3.16. Longitudinal Temperature Profiles at (a) the Top Surface of the Powder, (b) the Mid-Surface of the Powder, and (c) the Top Surface of the Baseplate. Continuous Laser. 1.76 mm/s Scanning Speed.

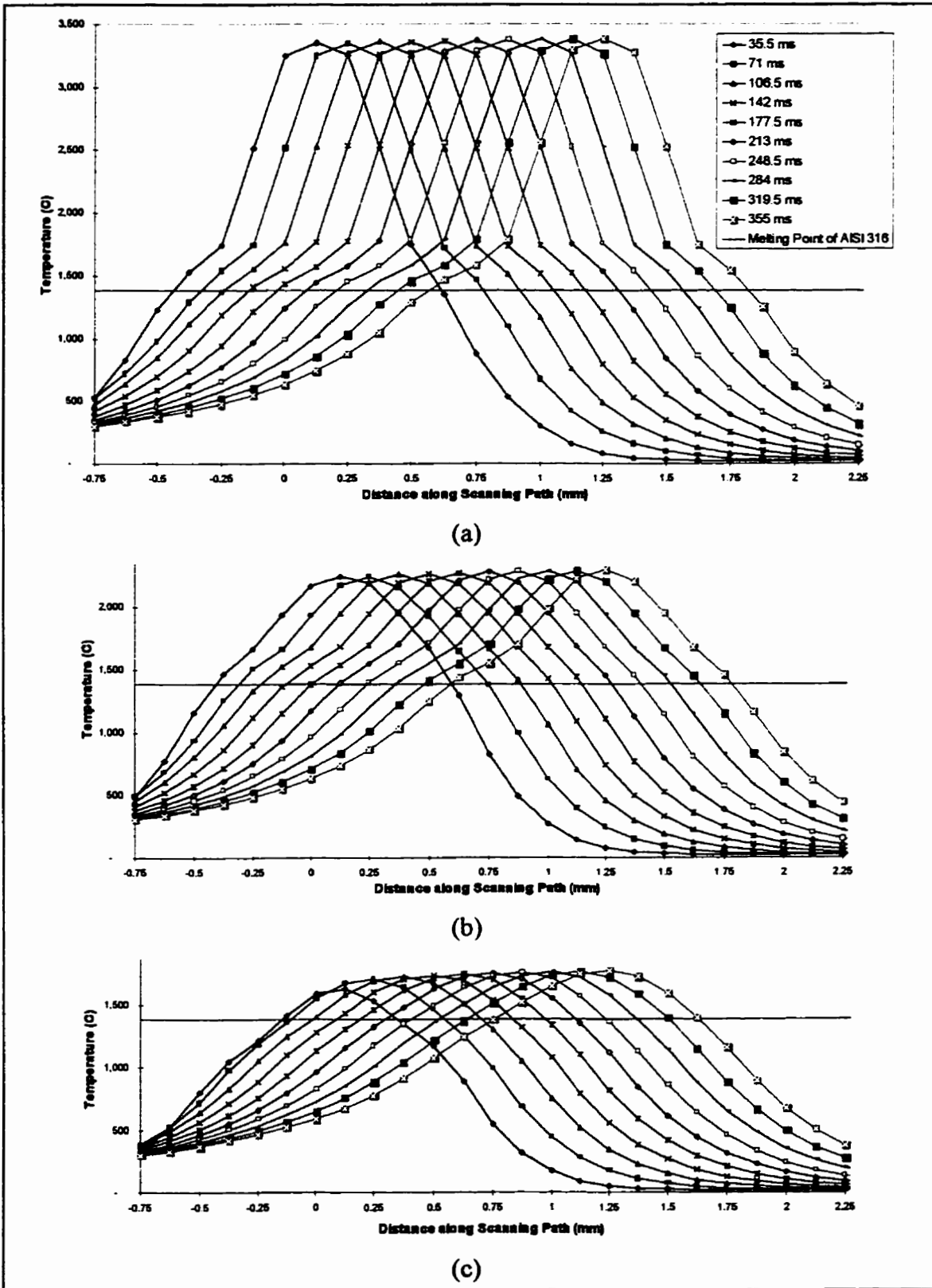


Figure 3.17. Longitudinal Temperature Profiles at (a) the Top Surface of the Powder, (b) the Mid-Surface of the Powder, and (c) the Top Surface of the Baseplate. Continuous Laser. 3.52 mm/s Scanning Speed.

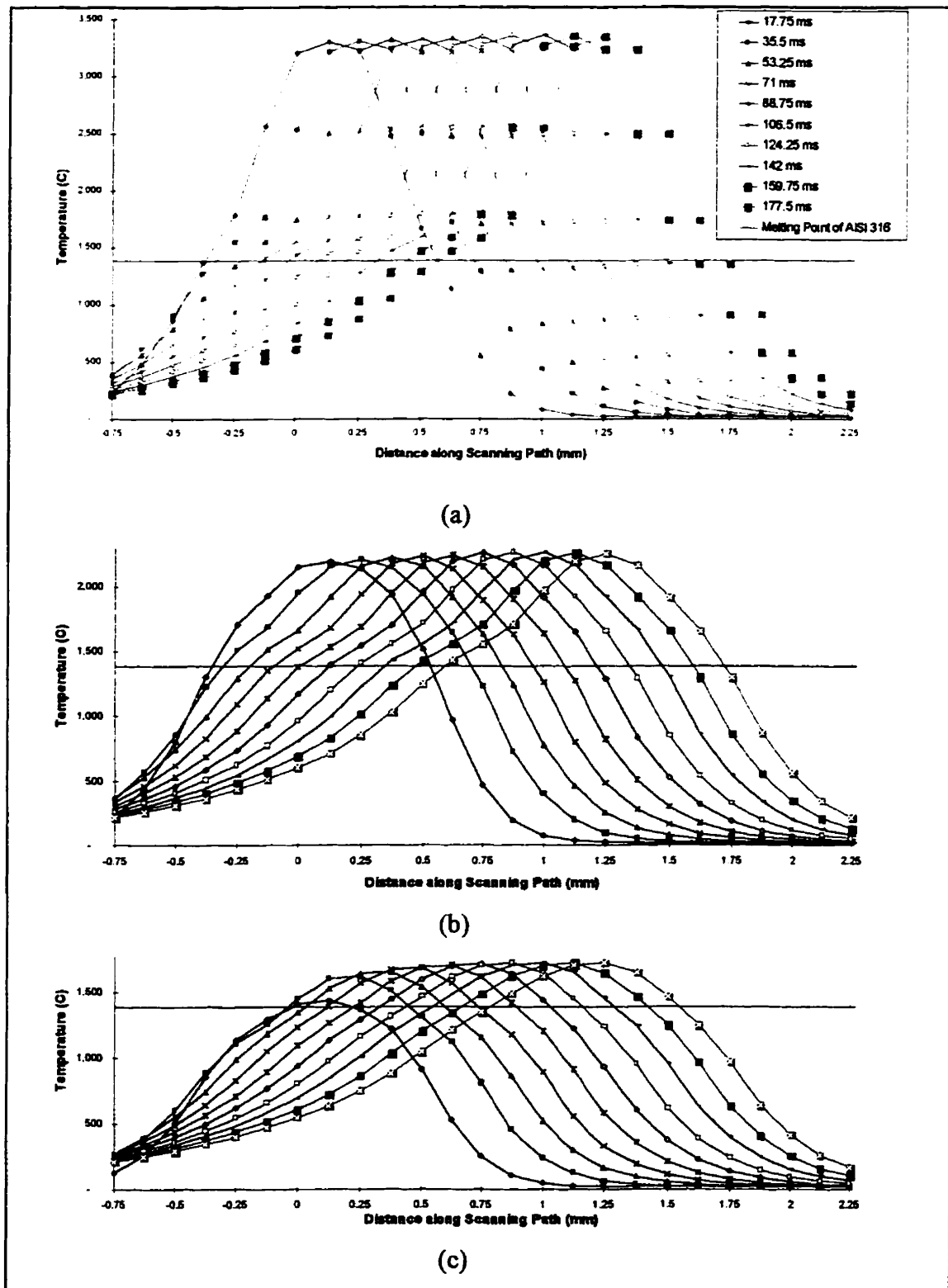


Figure 3.18. Longitudinal Temperature Profiles at (a) the Top Surface of the Powder, (b) the Mid-Surface of the Powder, and (c) the Top Surface of the Baseplate. Continuous Laser. 7.04 mm/s Scanning Speed.



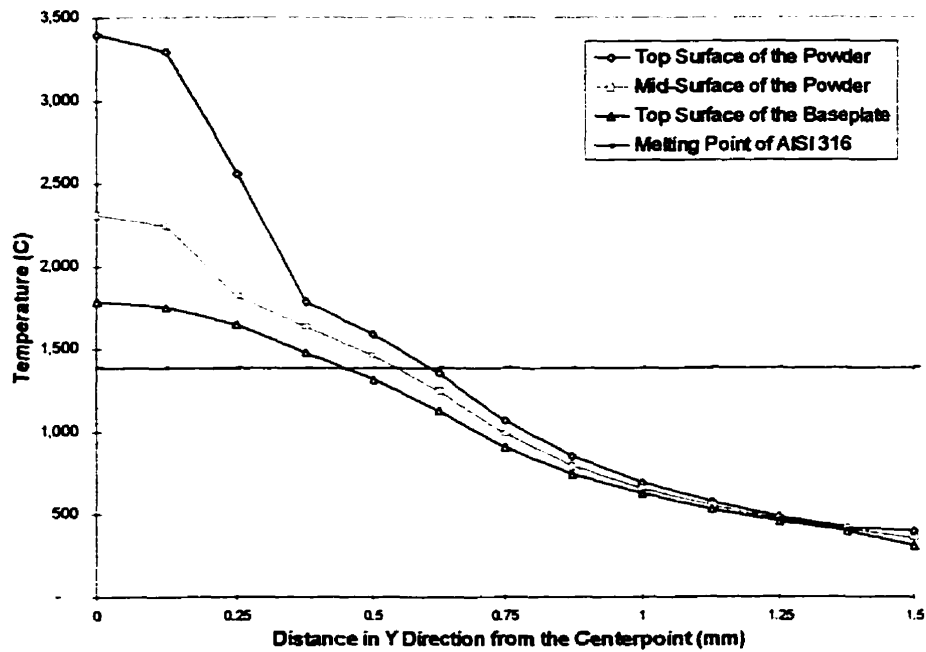


Figure 3.19. Typical Transverse Temperature Profiles for Continuous Laser

### 3.5 Calculation of Cladding Shape Properties for the Pulsed Laser

The cladding-shape properties considered herein are the cladding's width and height. The first step in the calculation of cladding shape properties is determination of the amount of molten powder due to the application of a pulse. From the results of thermal analysis, shown in Figure 3.14, it is noted that the maximum temperature is reached when the laser-pulse application ceases. Hence, the volume of molten powder should be calculated based on the temperature profiles corresponding to the ending time of the application of pulses.

#### 3.5.1 Assumptions

The following three assumptions are made:

- The molten powder forms a spherical shape on the baseplate,

- No material leaves the surface, i.e., no evaporation exists, and
- Shrinkage due to solidification is negligible.

### 3.5.2 Cladding Width Calculation

Proposed calculation of the cladding's molten-zone width is first based on the determination of the molten zone as follows:

- (A) Intersections of the temperature profiles, corresponding to (i) the top surface of the powder layer, (ii) the mid-surface of the powder layer, and (iii) the bottom surface of the powder layer (top surface of the baseplate), with the melting point line are determined, Figure 3.20. These intersection points are projected onto the X-axis.

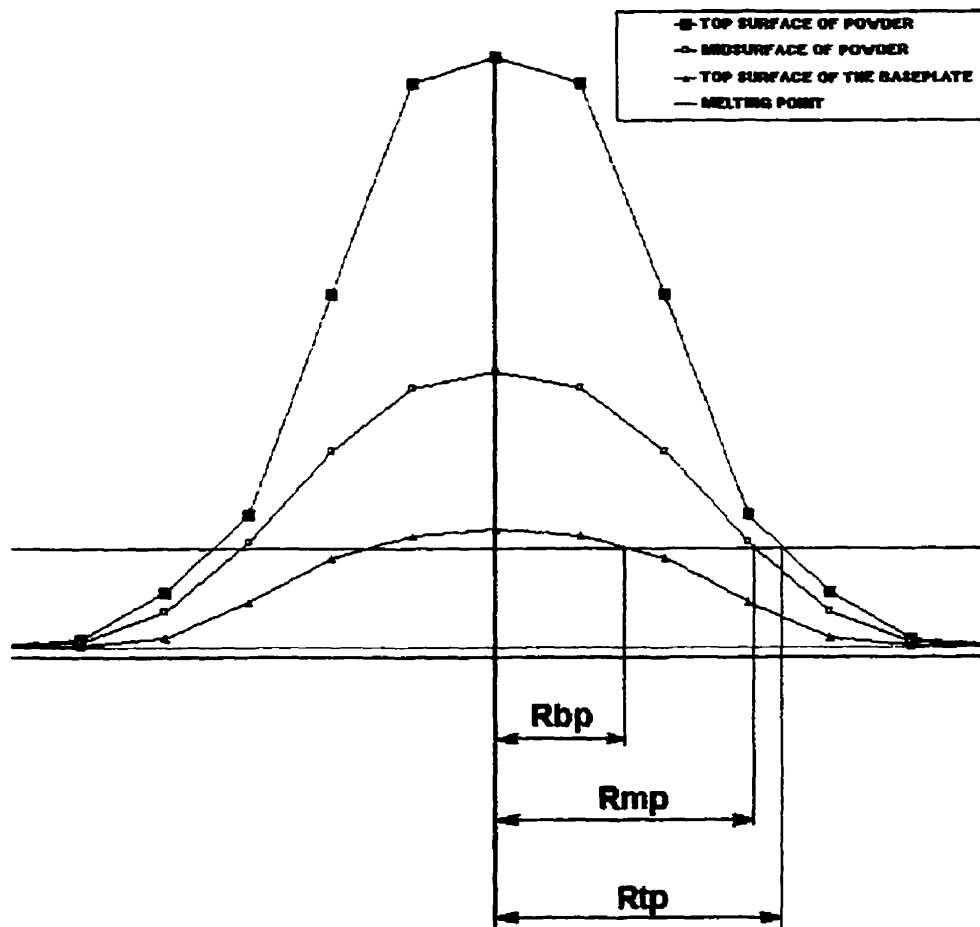


Figure 3.20. Temperature-Profile Projection.

(B) The distances between the center of the pulse and the projected points are defined as: (i)  $R_{tp}$ , on the top surface of the powder, (ii)  $R_{mp}$ , on the mid-surface of the powder, and (iii)  $R_{bp}=R_{ts}$ , on the bottom surface of the powder, respectively, Figure 3.21. These are utilized below to calculate the width of the molten zone.

In Figure 3.21, one can imagine the existence of two partial cones, whose combination approximately yields the equivalence of the overall molten powder. The first cone has the top powder surface as the base with a radius of  $R_{tp}$ , and it is intersected by the mid-surface plane. The second cone has the powder's mid-surface as the base with a radius of  $R_{mp}$ , and it is intersected by the bottom surface plane. It can be shown that, a cylinder with radius  $R_c$  is equal in volume to that of the two cones defined above [33]:

$$R_c = \sqrt{\frac{R_{tp}^2 + R_{tp}R_{mp} + 2R_{mp}^2 + R_{ts}R_{mp} + R_{ts}^2}{6}} \quad (3.20)$$

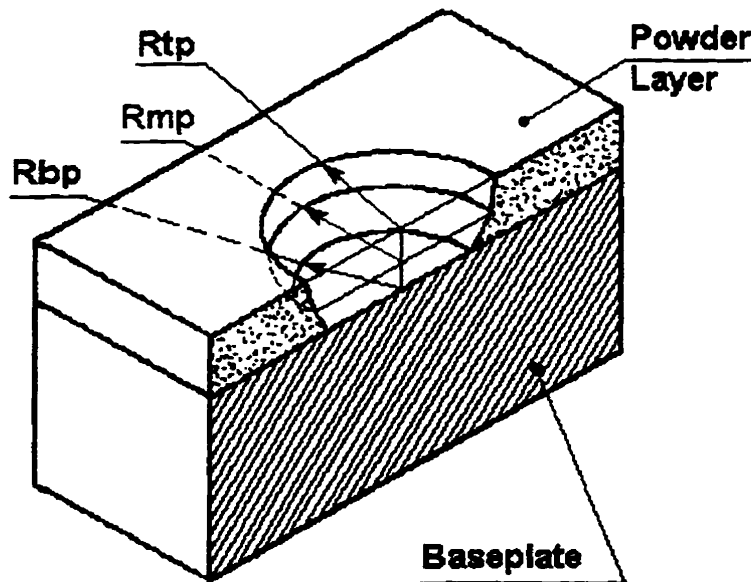


Figure 3.21. Conic Shape of the Molten Powder.

For simplification of the layer's height-calculation procedure, the radius of this cylinder  $R_c$  will be considered as the layer width.

### 3.5.3 Cladding-Height Calculation

The first step in the cladding height calculation is the determination of height of the mass, created on the top surface of the baseplate after the application of the first pulse.

The volume of the molten powder is:

$$V_p = \pi R_c^2 H_{pl}, \quad (3.21)$$

where  $H_{pl}$  is the original thickness of the powder layer (mm).

Correspondingly, the volume of the solid mass,  $V_{sg}$ , is determined as:

$$V_{sg} = V_p (\rho_p / \rho_s), \quad (3.22)$$

where  $\rho_p$  is the density of powder ( $\text{kg/m}^3$ ), and  $\rho_s$  is the density of baseplate ( $\text{kg/m}^3$ ).

Based on the assumption that the mass created on the top surface of the baseplate assumes a spherical shape, we can calculate the height of this mass,  $H$ , from the following relationship [33], Figure 3.22 (a):

$$H = \left( \frac{3V_{sg} + \sqrt{\pi^2 R_c^6 + 9V_{sg}^2}}{\pi} \right)^{1/3} - \frac{R_c^2}{\left( \frac{3V_{sg} + \sqrt{\pi^2 R_c^6 + 9V_{sg}^2}}{\pi} \right)^{1/3}}. \quad (3.23)$$

The center of the above defined spherical mass with radius  $R$ , is located at distance,  $h$ , below the surface of the plate:

$$h = R - H, \quad (3.24)$$

where

$$R = \frac{R_c^2 + H^2}{2H}.$$

(3.25)

From the temperature profiles corresponding to the end of the first pulse's cooling period, shown earlier in Figure 3.14, it can be noted that, the spherical mass may be completely re-solidified before the second pulse is applied. Thus, the application zone of the second pulse, overlapping in part with this first spherical mass, would remelt part of it in addition to the melting of additional new powder, Figure 3.22 (b). Therefore, the following generic procedure can be followed in order to determine the heights of the consecutive masses:

- i) The radii  $R_{tp}$ ,  $R_{mp}$ , and  $R_{bp}$  are determined from the temperature profiles, corresponding to the end of the (i+1)th pulsing cycle. Subsequently, the new value of  $R_c$ , namely  $R_{cnew}$ , is calculated.
- ii) The re-melted segment mass can be approximated as the cutout made by the cylinder of radius  $R_{cnew}$ . The distance between the center of the original mass and the center of the cutout cylinder,  $m$ , in the scanning direction, is defined by the scanning speed. (For example for the slow speed used in our analysis,  $m$  is equal to the length of one element, for the medium speed,  $m$  is equal to two lengths of the element, and for the fast speed,  $m$  is equal to three lengths of the element). The volume of this cutout is determined as [34]:

$$V_s = \int_{m-R_{cnew}}^{m+R_{cnew}} dx \int_0^{R_{cnew}^2 - (x-m)^2} z dy, \quad (3.26)$$

where  $z = h + \sqrt{R^2 - x^2 - y^2}$  is the equation of the (i)th spherical segment. Due to the complexity of Equation (3.26), it was solved numerically using MATLAB [35].

- iii) The volume of the new powder melted by the (i+1)th laser pulse,  $V_p'$ , is determined by the intersection of two parallel cylinders, of radii  $R_c$  and  $R_{cnew}$ , respectively. These cylinders are bounded by the planes  $z = H_{pl}$  and  $z = 0$ , (top surface of the baseplate), and their centers are separated by the distance  $m$ .
- iv) Thus, the total volume of the new spherical “solid” mass,  $V_t$ , obtained after the application of the (i+1)th pulse, is:

$$V_t = \frac{\rho_p}{\rho_s} V_p' + V_s \quad (3.27)$$

- v) The known parameters for the calculation of the (i+1)th segment's height are: its width,  $R_{cnew}$ , and the maximum height of the unmolten part of the first spherical mass,  $Z_p$ , (Figure 3.23), which can be derived as [34]:

$$Z_p = \sqrt{R^2 - m^2 - 2mR_{cnew} + R_{cnew}^2} \quad (3.28)$$

The second mass can be approximated as a portion of the spherical segment with radius  $R_{new}$ , bounded by cylinder with radius  $R_{cnew}$ , Figure 3.22 (c).

- vi) In order to determine the (i+1)th mass height, one must find the location of this mass' center. This center is located on the X-Z plane at  $y = 0$ , Figure 3.23.

The volume of the (i+1)th mass,  $V_{i+1}$ , which is equal to  $V_t$ , can be expressed in terms of  $R_{new}$ , X-coordinate of the center of the sphere,  $x_{new}$ , and the Z-coordinate of the center of the spherical segment,  $h_{new}$ , as [34]:

$$V_{i+1} = 2 \int_{x_{new}-R_{cnew}}^{x_{new}+R_{cnew}} dx \int_0^{\sqrt{R_{cnew}^2 - (x-x_{new})^2}} \left( h_{new} + \sqrt{R_{new}^2 - x^2 - y^2} \right) dy \quad (3.29)$$

Solving Equation (3.29) for  $R_{new}$ , the height of the second mass,  $H_{new}$ , is determined using the following equation:

$$H_{new} = R_{new} - h_{new} \quad (3.30)$$

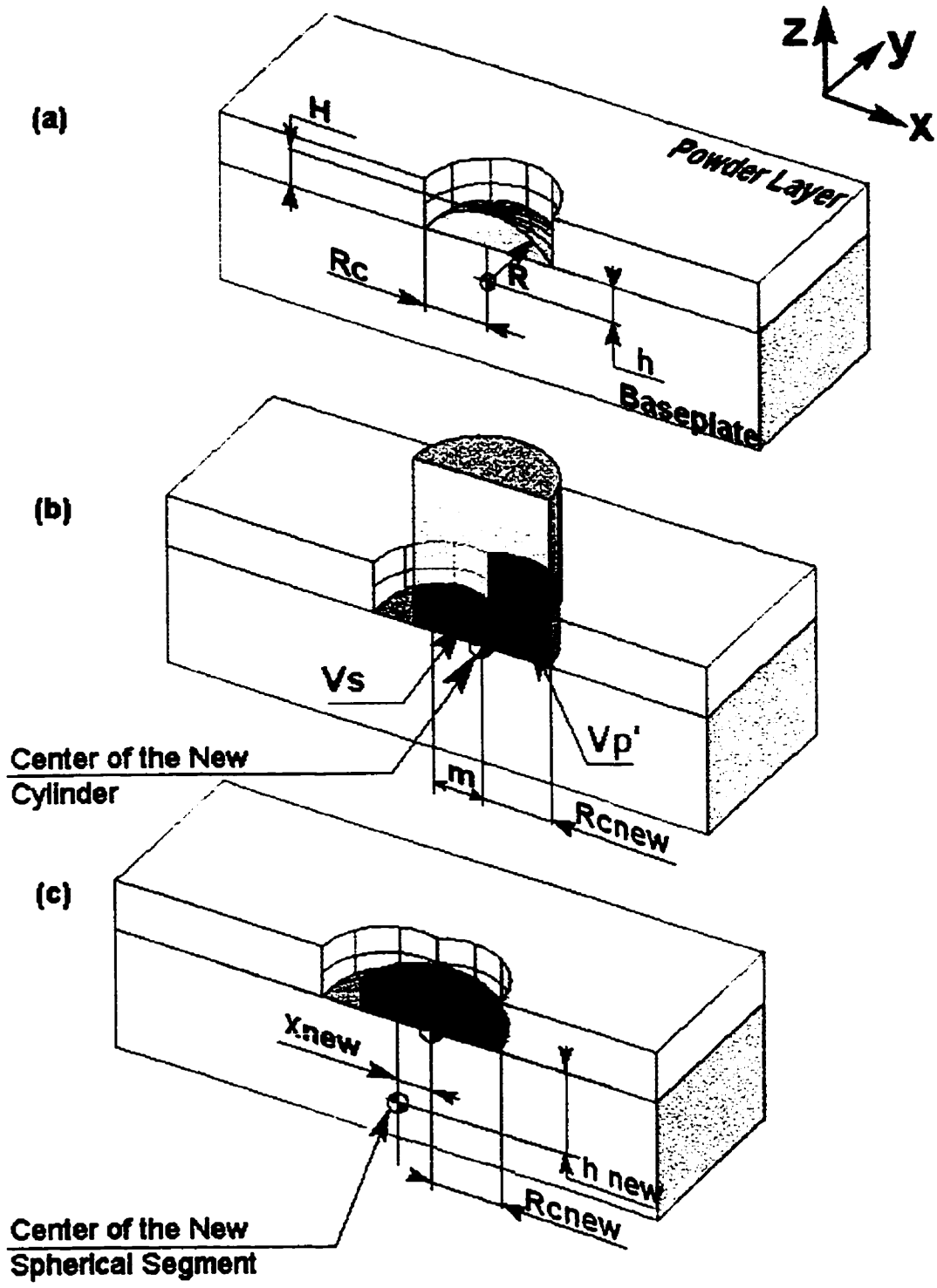


Figure 3.22. Cladding Height Calculation for A Pulsed Laser.

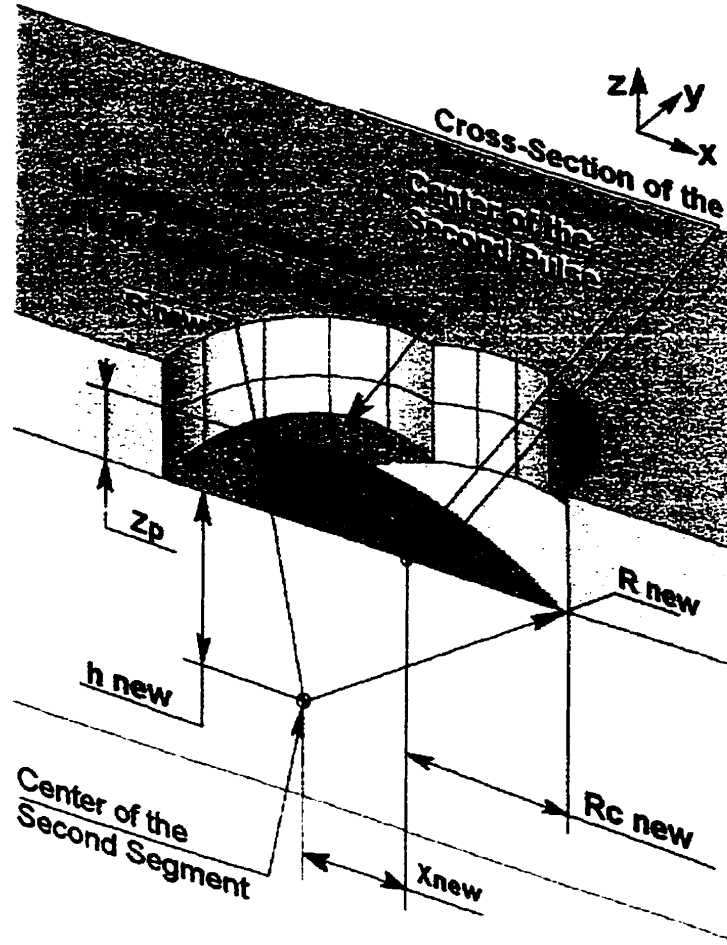


Figure 3.23. Nomenclature Used in the Calculation of Geometrical Properties of the Second Segment.

It can be shown that  $R_{new}$  and  $h_{new}$ , in Equation (3.29) can be expressed as [33]:

$$h_{new} = \frac{Z_p^2 - 4x_{new}^2}{2Z_p}, \quad (3.31)$$

$$R_{new} = \sqrt{(x_{new} + R_{cnew})^2 + h_{new}^2}. \quad (3.32)$$

Substitution of Equations (3.31) and (3.32) into Equation (3.29) leads to an equation with one unknown  $x_{new}$ . Due to complexity of the resulting equation, this equation was solved herein numerically using MATLAB [35]. The values of  $R_{new}$ ,  $h_{new}$ , and  $H_{new}$  are found using Equations (3.30) through (3.32).



### 3.5.4 Longitudinal, Centerline Cross-Section of the Pulsed-Laser Cladding

The cross sections of the spherical masses, obtained after every laser-beam pulse are represented in Figure 3.24 for the three different scanning velocities used in this thesis. Since the thermal process reached a steady state after at most seven pulsing cycles, the cross-sections were constructed only for these seven pulses.

In Figure 3.24, the dashed lines show the cross-sections of the original spherical masses before they are remelted by the subsequent pulse. The remelted zones are noted by vertical lines. Also, the centers of these single spherical masses are shown.

The simulated results of the longitudinal, centerline cross-section cladding-profile reconstruction process, are shown in Table 3.2. The maximum layer height is given along with the variability<sup>1</sup> of its value. It can be noted from Table 3.2 that, claddings, produced with higher scanning speeds have greater height variability.

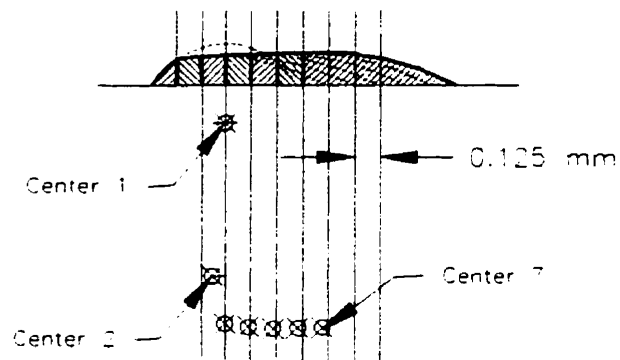
Table 3.2. Layer Height versus Scanning Speed for Pulsed Laser (14 Hz).

Scanning Speed (mm/s)	1.76	3.52	5.28
Cladding Height (mm)	0.16±0.0003	0.151±0.0034	0.132±0.0082

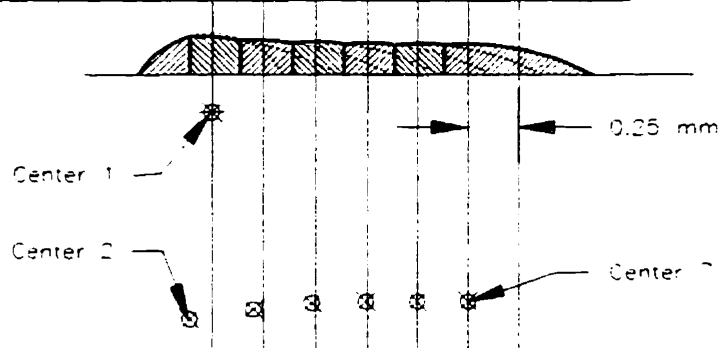
---

<sup>1</sup> Variability is the difference between the maximum and the minimum cladding height.

Scanning Speed = 1.76 mm/s



Scanning Speed = 3.52 mm/s



Scanning Speed = 5.28 mm/s

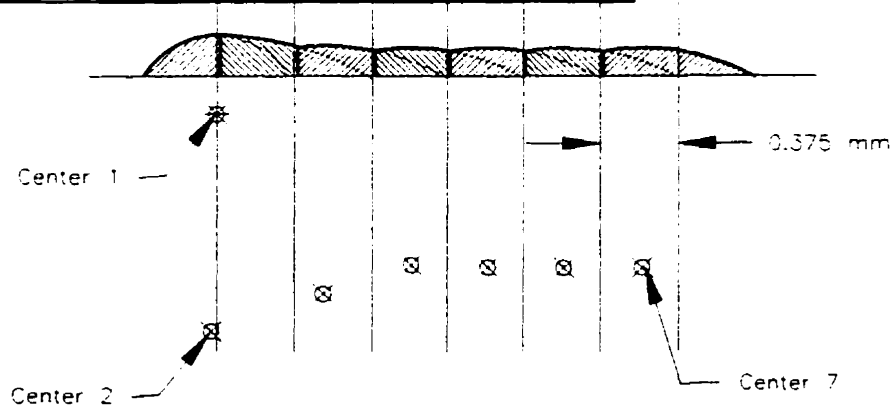


Figure 3.24. Longitudinal Centerline Cross-Section Profile of the Cladding Produced by Pulsed Laser (14 Hz).

### 3.6 Calculation of Cladding-Shape Properties for a Continuous Laser

The powder melting process for the continuous laser beam is a continuous event. As the laser advances in the scanning direction, it melts new powder with a solidifying wall preceding it. The shape of the cladding can be approximated simply by a horizontal cylindrical mass bounded by two half-spherical segments, Figure 3.25.

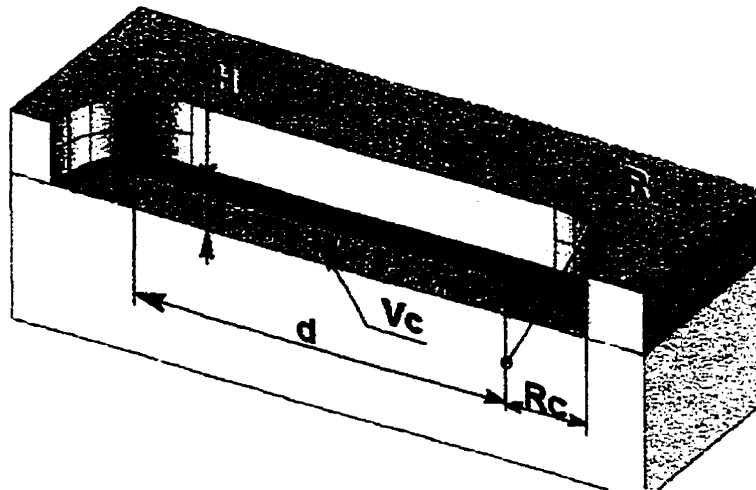


Figure 3.25. Geometric Approximation of A Cladding Produced by a Continuous Laser.

The width of the cladding is determined using the same procedure as the one for the pulsed laser. However, in this case instead of the longitudinal temperature profile, the transverse temperature profile is used. The intersections of the temperature profiles, at the powder's top, mid-, and bottom surfaces with the melting point of the metal, projected onto the X-axis, yield the molten-zones' radii. These radii values are used to determine the cladding width as in Section 3.5.2.

One can recall that the results of the thermal analysis showed a quick convergence to the steady state for a continuous laser beam, Figures 3.16 through 3.18. The implication is that, the geometric properties of the cladding at the beginning of the scanning can be

omitted. Therefore, the following cladding-height determination procedure is used by first assuming that the process has already reached a steady state:

- (i) The volume of the overall powder, molten by the laser,  $V_p$ , is determined as [33]:

$$V_p = \pi R_c^2 H_{pl} + R_c H_{pl} d, \quad (3.33)$$

where  $R_c$  is the half-width of the layer,  $H_{pl}$  is the original thickness of the powder layer, and  $d$  is the distance traveled by the laser beam.

This powder volume is converted into an equivalent solid-mass' volume,  $V_s$ , as:

$$V_s = \frac{\rho_p}{\rho_s} V_p. \quad (3.34)$$

- (ii) Since the shape of the cladding is approximated by two geometrical primitives, its volume,  $V_c$ , can be written as a function of one unknown,  $H$ , (cladding height) [33]:

$$V_s = \frac{1}{6} \pi (3R_c^2 H + H^3) + \frac{1}{8} d \frac{(H^2 + R_c^2)^2 \left( 2 \arcsin\left(\frac{2R_c H}{H^2 + R_c^2}\right) - \sin\left(2 \arcsin\left(\frac{2R_c H}{H^2 + R_c^2}\right)\right) \right)}{H^2} \quad (3.35)$$

The solution of Equation (3.35) for  $H$  yields the cladding height.

### 3.7 Simulation Results of Cladding's Shape-Properties

The cladding-height and the cladding-width calculation results are plotted in Figures 3.26 and 3.27, and detailed in Table 3.3, for (i) a pulsed laser at 14 Hz pulsing frequency, (ii) a pulsed laser at 33 Hz pulsing frequency, and (iii) a continuous laser. The calculations for the pulsed-laser cladding height and width correspond to their maximum values at the steady state.

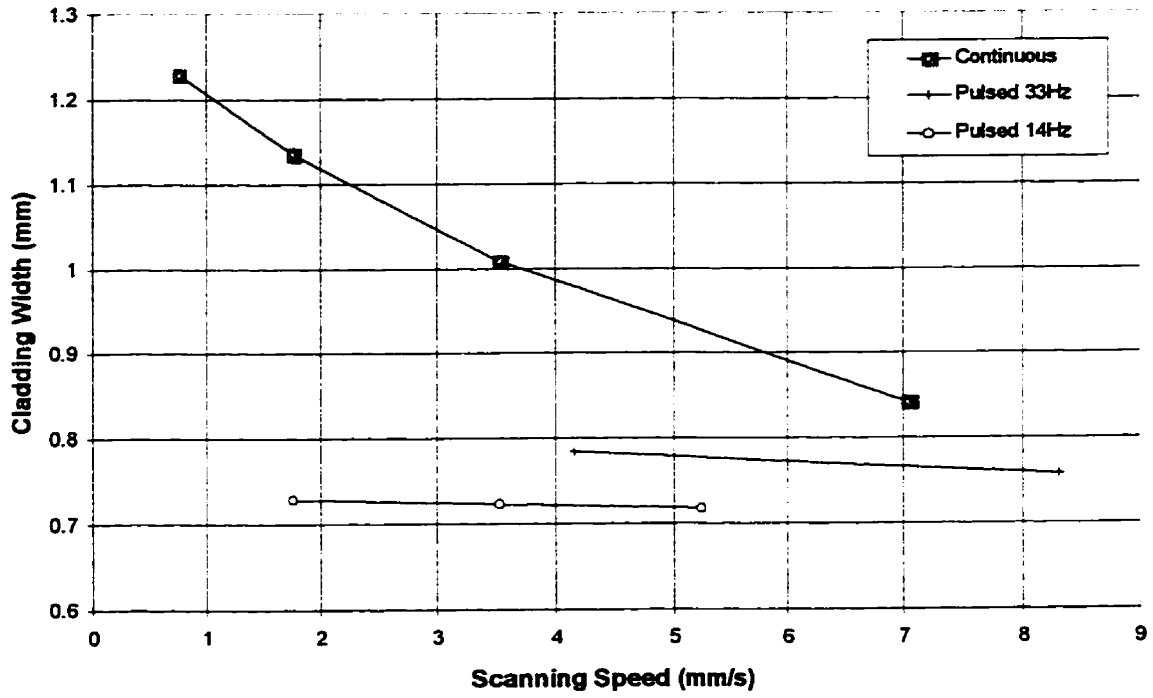


Figure 3.26. Cladding Width versus Scanning Speed.

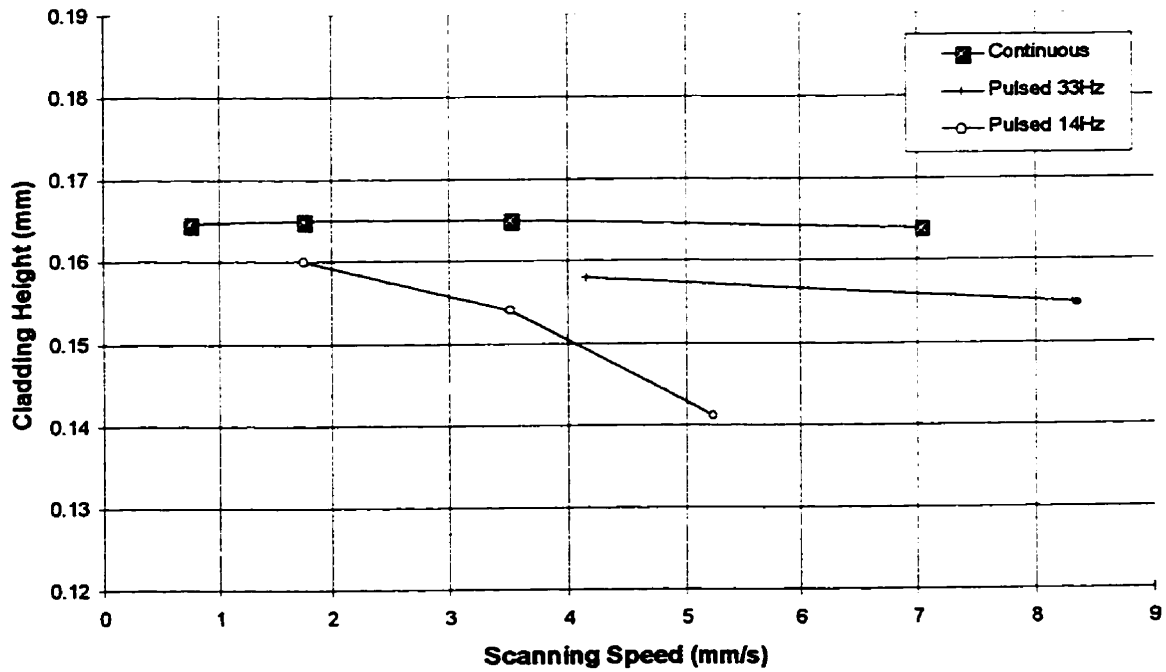


Figure 3.27. Cladding Height versus Scanning Speed.

**Table 3.3. Results of the Cladding's Shape-Properties Calculation**

Speed (mm/s)		0.75	1.76	3.52	4.16	5.24	7.04	8.32
Cladding Height (mm)	Continuous	0.1647	0.165	0.165			0.164	
	Pulsed 33Hz				0.158			0.155
	Pulsed 14Hz		0.16	0.154		0.141		
Cladding Width (mm)	Continuous	1.228	1.135	1.009			0.841	
	Pulsed 33Hz				0.784			0.757
	Pulsed 14Hz		0.729	0.723		0.718		

### 3.7.1 Discussion

#### 3.7.1.1 Cladding Width

From Figure 3.26, it is seen that the width of the cladding produced by the pulsed laser decreases with increasing scanning speed. This phenomenon is explained below.

First, from Figure 3.14, one notes that the thermal process is characterized by high cooling rates. The top surface of the powder cools down from 8,000°C to about 150°C within 71 ms. Thus, when the next laser pulse is applied, the surface has a temperature only slightly higher than the initial temperature (max.  $\Delta T \approx 130^\circ\text{C}$ ). As the laser translates with higher speeds, the temperature of the previous application area decreases more rapidly as well. However, it was noted that the corresponding differential decrease in temperature is not large (in the order of 20°C). The consequent decrease in the cladding width is therefore also not significant.

On the other hand, in the case of the continuous laser, the impact of the increase in speed is more substantial and causes a significant decrease of the layer width. Namely, the slower the continuous laser beam scans the surface, the more it preheats the region of the powder and the baseplate before getting there. Hence, when the laser does advance forward with a slow speed, the new surroundings of the beam's application require less energy to melt than they would in the case of a faster speed.

### 3.7.1.2 Cladding Height

From Figure 3.27 it is seen that the cladding height for the pulsed laser decreases as the scanning speed increases. This decrease is due to the fact that the solid volume of the available material to be melted for a pulse, i.e., the remelted portion of the earlier built cladding decreases with increasing scanning speed.

On the other hand, the height of the cladding in the case of a continuous laser almost does not change with the scanning speed. Although the volume of the powder to be melted by the laser beam decreases with increased scanning speed, the width of the cladding decreases, thus, resulting in an almost constant layer height.

One of the most important parameters for a layered-manufacturing technique is a part-fabrication time. As indicated by the simulation results, the continuous laser can build claddings with shape properties comparable to those of the claddings built by a pulsed laser, but achieve these at higher scanning speeds. Also, from Table 3.2 it can be noted, that an increase in the scanning speed for the pulsed laser leads to a greater variability in cladding's shape properties, whereas the claddings produced by a continuous laser may be more consistent.

## 4. DESIGN OF EXPERIMENTAL SET-UP

The Nd-YAG laser-welding machine, at the Laser Machining Center Inc., Toronto, Ontario, was made available to this research for experimenting with a pulsed laser. The additional set-up built and used with this machine will be described in detail in Chapter 5. For experimenting with a continuous laser, on the other hand, the development of a new experimental set-up was initiated in the University of Toronto. A 150 W, continuous, Nd-YAG laser with fiber-optic light-delivery system, made by Heraeus LaserSonics Inc., was acquired for this purpose. The design of this experimental, prototype rapid manufacturing system is discussed in this Chapter.

### 4.1 Axiomatic Approach to Design

Design may be formally defined as synthesis of solutions, in the form of products, processes or systems, that satisfy the needs of customers. This can be achieved through a mapping between the Functional Requirements (FRs) of the product/process and the Design Parameters (DPs). More than one solution may result from the generation of the DPs that satisfy the FRs. The design axioms, provided by the Axiomatic Approach to Design [36] can be used as principles which the mapping technique must satisfy to produce a good design. These axioms offer a basis for comparing and selecting synthesis solutions [36]:

1. *The Independence Axiom*: Maintain the independence of FRs, and
2. *The Information Axiom*: Minimize the information content.

The above mentioned Axiomatic Approach to Design is used herein as a tool for the evaluation of various design decisions.



## 4.2 Identification of Main Functional Requirements

One can recall that the primary steps for the proposed fabrication process for building 3D parts via the laser-beam fusion of predeposited metal powder, are as follows:

- (1) A container deposits powder onto the top surface of the baseplate, Figure 2.2(a).
- (2) A wiper levels the powder yielding the required layer thickness, Figure 2.2(b).
- (3) A laser beam selectively melts the metal powder, Figure 2.2(c).
- (4) A piston lowers the part by the required layer height, Figure 2.2(d).

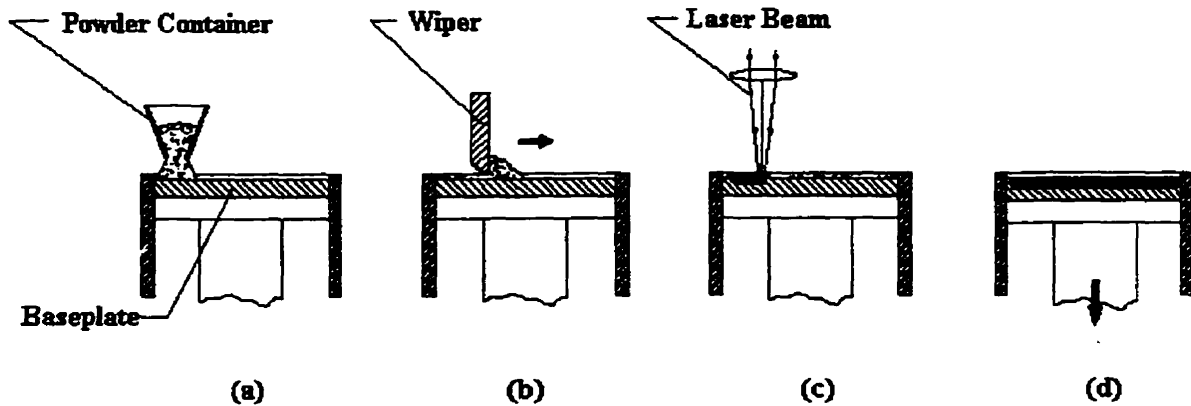


Figure 2.2. Steps of Proposed Process.

The above process must take place in an inert gas-environment. Therefore, the synthesis problem at hand can be stated as follows:

*Design an apparatus, which will allow the layered production of fully-densed metal parts based on the process described above.*

The following first-level FRs are identified as follows:

FR1 = Maintain a powder layer with required uniform thickness,

FR2 = Selectively scan the powder,

FR3 = Fully melt the powder, and

FR4 = Stack the layers.

The necessity of inert gas environment is considered here as a system constraint.

The second constraint considered in this design process is the overall size of the building chamber. Since the current project's objective is only the investigation of process-parameters' influence on the single-claddings' geometrical properties, the size of the building volume was limited to 100 x 100 x 100 mm.

### **4.3 Selection of the First-Level Design Parameters**

Based on the Independence Axiom, the highest priority, in search for appropriate DPs, is given to finding such DPs which would control only their respective FRs in a decoupled or uncoupled manner. The second important consideration is the manufacturability of the selected design solution and use of standard components. This agrees with the Information Axiom. The information content of the design is reduced by avoiding solutions requiring unnecessary machining and tight tolerances.

Considering the first-level FRs, it can be deduced that the system would incorporate at least six subsystems: powder delivery and leveling, laser-light delivery, horizontal-plane (XY) motion, vertical (Z) motion, inert-gas supply, and overall process-control.

The design parameters for the corresponding FRs (numbering of FRs has been changed due to elimination of FR1) are chosen as follows:

- DP1 = Powder delivery and leveling,
- DP2 = Computer-controlled X-Y motion,
- DP3 = Irradiance of the laser beam, and
- DP4 = Computer-controlled Z-axis motion.

At the current stage, the design equation for the first level of FRs is:

$$\begin{Bmatrix} FR1 \\ FR2 \\ FR3 \\ FR4 \end{Bmatrix} = \begin{bmatrix} X & ? & O & X \\ O & X & O & O \\ O & ? & X & O \\ ? & O & O & X \end{bmatrix} \begin{Bmatrix} DP1 \\ DP2 \\ DP3 \\ DP4 \end{Bmatrix} \quad (4.36)$$

where “X” indicates that a change in DP affects corresponding FR, “O” indicates that a change in DP does not affect corresponding FR, and “?” indicates that effect of DP on FR is not clear at this stage.

#### 4.3.1 First-Level, Design-Matrix Considerations

The powder delivery and leveling DP does not affect the selective scanning of the powder, and nor its melting, resulting in an “O” in the {2,1} and {3,1} elements of the design matrix of Equation (4.36). This statement is accurate provided that (i) the required powder layer thickness is kept constant during the part-building process, and (ii) that its optimal value is derived from the process-simulation and experimentation results at the current stage of the research. Based on this argument, the “?” in {4,1} element of the matrix can also be replaced with an “O”.

The influence of the XY plane motion on the powder-layer quality depends on the general layout of the system. In the case of having a moving building chamber and a fixed light-delivery subsystem, there exists a possibility that during scanning the powder can be displaced, affecting the layer uniformity. This would yield an “X” entry in the {1,2} element of the design matrix. On the other hand, if the building chamber is assumed to be fixed in the horizontal plane, and the laser-light delivery subsystem moves during scanning, this problem would not exist, resulting in an “O” entry in the design matrix. Hence, the

latter system layout-scheme is used herein to maintain independence of the functional requirements.

The X-Y plane scanning motion does not affect the melting of the powder, if the scanning speed is kept below a limiting value. This limit must be determined through experimentation. Therefore, the “?” in the {3,2} element of the design matrix can be replaced by an “O”.

Irradiance of the laser beam does not affect the maintenance of the required thickness of the powder layer, nor the selective scanning of the powder, resulting in an “O” in {1,3} and {2,3} entries in the design matrix.

The {4,3} element of the design matrix is set to “O” based on the fact that the process parameters are defined upon a priori and kept within their working range.

The “X” in the {1,4} design-matrix element indicates that the Z motion affects the powder-layer thickness, defined herein as the vertical distance between the wiper and the platform.

The “O” in the {2,4} and {3,4} elements of the design matrix indicate that the vertical motion of the platform does not affect selective scanning and melting of the powder due to the fact that its optimal value is defined in advance and kept constant.

The first-level design matrix can therefore be modified as follows:

$$\begin{Bmatrix} FR1 \\ FR2 \\ FR3 \\ FR4 \end{Bmatrix} = \begin{bmatrix} X & O & O & X \\ O & X & O & O \\ O & O & X & O \\ O & O & O & X \end{bmatrix} \begin{Bmatrix} DP1 \\ DP2 \\ DP3 \\ DP4 \end{Bmatrix}. \quad (4.37)$$

As seen in Equation (4.37), a decoupled design is obtainable. This design matrix indicates that FR1 must be determined first by adjusting DP1 and DP4. The system

constraint (inert-gas environment) is satisfied by the hermetic enclosure of the processing chamber.

#### **4.4 Design Decomposition**

The design matrix (4.37) for the first level of the functional requirements defines the general configuration of the experimental set-up. In order to manufacture it, however, one needs information about its constituent components and subsystems. In order to obtain this information, further decomposition of the main level FRs and their corresponding DPs is needed [36]. This decomposition would result in a hierarchical configuration of the system in the functional and physical domains. The experimental system can be manufactured based on the information from the lowest level of the physical-domain hierarchy, where further decomposition is impossible.

##### **4.4.1 Powder Delivery and Leveling**

The corresponding FR for this subsystem is stated as “maintaining required uniform thickness for the powder layer”. The following FRs of the second level can now be derived as:

FR11 = Deliver a sufficient amount of powder onto the baseplate, and

FR12 = Produce a powder layer with a uniform thickness.

The corresponding DPs of this level of decomposition are:

DP11 = Powder delivery subsystem, and

DP12 = Wiping subsystem.

The powder-delivery subsystem must be designed in such a way that it deposits the amount of powder needed for covering the entire surface of the baseplate. The subsystem

must also deliver the powder to the front part of the wiping unit. If both conditions are satisfied, the resulting design matrix is uncoupled, namely,

$$\begin{Bmatrix} FR11 \\ FR12 \end{Bmatrix} = \begin{bmatrix} X & O \\ O & X \end{bmatrix} \begin{Bmatrix} DP11 \\ DP12 \end{Bmatrix}. \quad (4.38)$$

#### 4.4.1.1 Powder-Delivery Subsystem

The requirement for the powder-delivery subsystem is to deliver sufficient amount of powder to cover the entire surface of the baseplate. The powder-delivery system is connected to the hermetic enclosure, and therefore, sufficient amount of powder must be stored in the system in order to minimize disturbances to the process. The oxygen in the air must be removed from the powder-delivery subsystem prior to the process in order to prevent oxidation of the material at elevated temperatures, and the unit must be filled with inert gas. The FRs of the third level are, therefore:

FR111 = Store a sufficient amount of powder,

FR112 = Remove oxygen from powder prior to deposition,

FR113 = Fill the storage unit with an inert gas, and

FR114 = Deposit a sufficient amount of powder to cover the entire surface of the baseplate.

The design parameters for the first three FRs are:

DP111 = Volume of the storage container,

DP112 = Powder vacuum-treatment, and

DP113 = Constant inert-gas supply to the storage container.

A rotary shaft with a slot, driven by a computer-controlled stepper motor, was chosen for the deposition, Figure 4.1. Prior to deposition, the slot faces upwards, thus accumulating sufficient amount of powder within it. During deposition, the shaft rotates 180° and dumps the powder in front of the wiper.

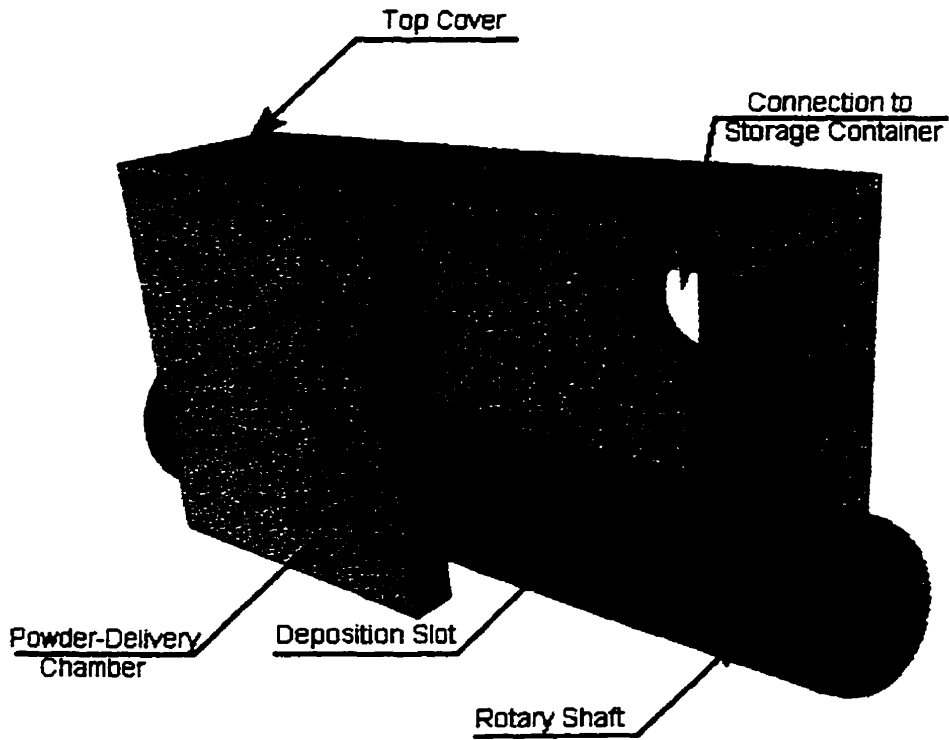


Figure 4.1. Powder-Delivery Working Chamber.

Therefore, the DP for the last FR is:

DP114 = Volume of the slot.

The resulting design matrix is:

$$\left\{ \begin{array}{l} FR111 \\ FR112 \\ FR113 \\ FR114 \end{array} \right\} = \begin{bmatrix} X & 0 & 0 & 0 \\ 0 & X & 0 & 0 \\ 0 & 0 & X & 0 \\ 0 & 0 & 0 & X \end{bmatrix} \left\{ \begin{array}{l} DP111 \\ DP112 \\ DP113 \\ DP114 \end{array} \right\} \quad (4.39)$$

Equation (4.39) indicates that the design of the powder-delivery subsystem is uncoupled. Thus, the independence of functional requirements is achieved.

It must be noted that, due to height limitations, the powder-storage container is located away from the powder-delivery chamber. They are connected by a flexible tube, where the powder is delivered by gravitational forces.

The powder-delivery chamber is enclosed by a top cover with multiple holes. A filter is installed underneath the cover in order to provide an escape route to residual air, and prevent pressure build-up in the chamber.

#### 4.4.1.2 Wiping Subsystem

The functional requirement for the wiping subsystem is to produce a powder layer with a uniform thickness. In order to achieve this objective, a planar wiper is utilized. The wiper can be driven by a computer-controlled stepper motor through a leadscrew. The main requirement for this wiper is to maintain a uniform thickness of the powder layer. This can be achieved by maintaining of the wiper's parallel motion using two guiding slots, Figure 4.2.

The wiping of the powder is achieved by first shearing off the pile of powder using a scraper blade, and subsequently rolling it using a cylindrical roller. The effectiveness of these two steps must be investigated in terms of the layer-surface quality. In the current design, a modular wiper is utilized to allow such a future investigation. Also, as reported in [37], the direction of the roller's rotation may have an effect on the powder-layer surface quality. The roller's shaft was expanded on one side, thus, allowing a future installation of a driving-belt gear, Figure 4.2.



Due to the possible magnetic effect of the building materials, the roller should be brass. The ends of the roller's shaft are installed in the wiper's frame using bearings.

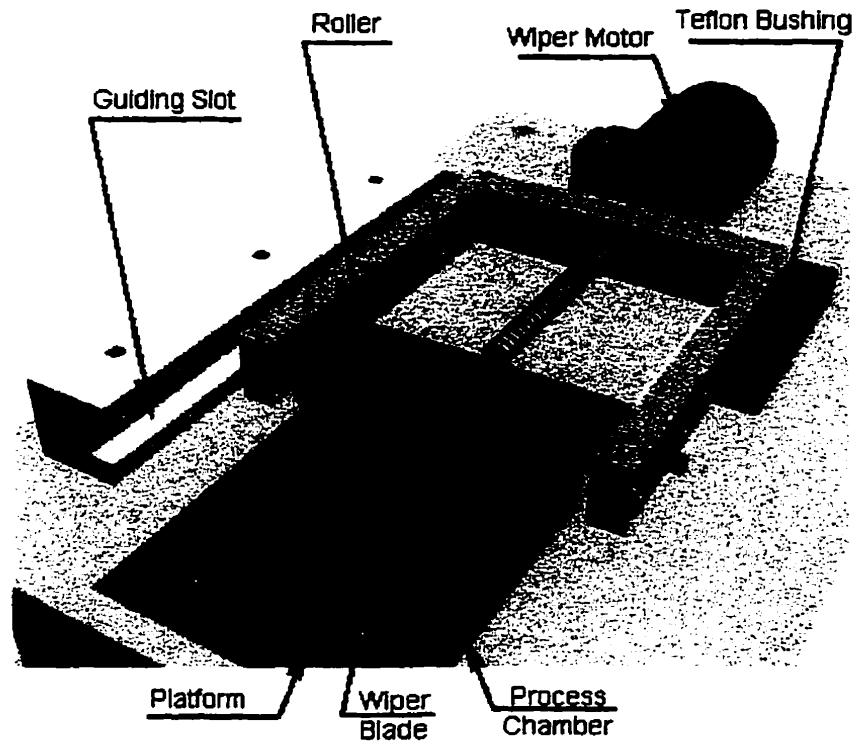


Figure 4.2. Wiping Subsystem (second guiding slot is not shown).

The FRs of the wiping subsystem are as follows:

FR121 = Uniform thickness of powder layer, and

FR122 = Good surface quality of powder layer.

The corresponding DPs are:

DP121 = Guiding slots, and

DP122 = Geometry of wiping device.

The resulting design equation,

$$\begin{Bmatrix} FR121 \\ FR122 \end{Bmatrix} = \begin{bmatrix} X & O \\ O & X \end{bmatrix} \begin{Bmatrix} DP121 \\ DP122 \end{Bmatrix}, \quad (4.40)$$

shows that the design is uncoupled.

#### 4.4.2 Laser-Light Delivery

The general configuration of the system is based on a fixed processing chamber, with a vertically moving platform, and a moving laser-light-delivery subsystem, mounted on an X-Y table. The main requirements for this subsystem are (i) the ability to focus the laser beam, and (ii) to be of light weight, in order to minimize the inertial forces of the moving components. These requirements were satisfied by purchasing a fiber-optic based customized focusing system from Melles-Griot Canada, Inc., Figure 4.3.

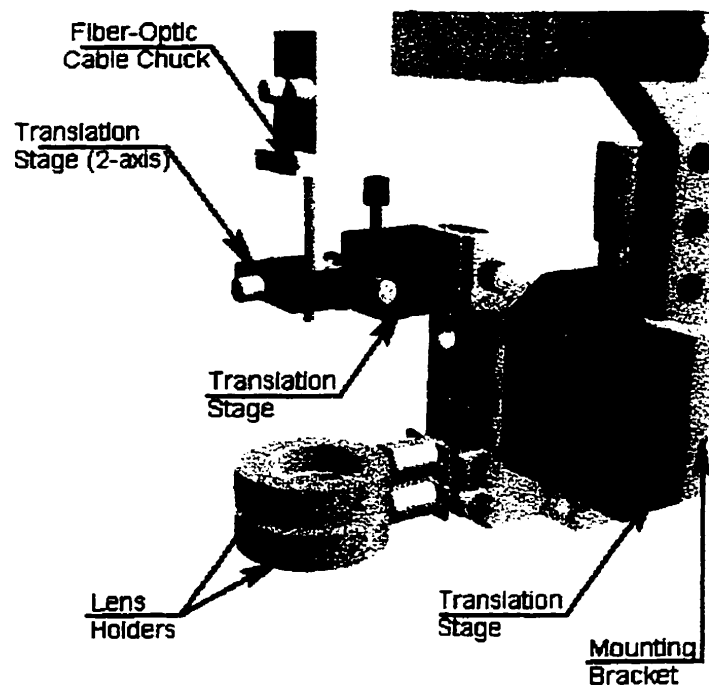


Figure 4.3. Laser-Light Delivery Subsystem.

The proposed solution agrees with the axiomatic approach to design, which considers use of standard components as minimization of the information content.

### 4.4.3 Horizontal Motion Subsystem

The requirement for the X-Y horizontal motion subsystem is to provide the laser-light-delivery subsystem with an effective ability to selectively scan the powder layer. The proposed “gantry-table” configuration is shown in Figure 4.4. Two motors are used: a high-resolution linear stepper-motor (12,500 steps/inch or 492 steps/mm), and a high-resolution servo motor (25,000 steps/revolution), both manufactured by Compumotor Inc. These motors are connected to their respective motion controllers, which are in turn connected to a PC. The rotation of the servo motor was translated into a linear motion using a ballscrew with reduced backlash, manufactured by NEAT Motion Products Ltd.

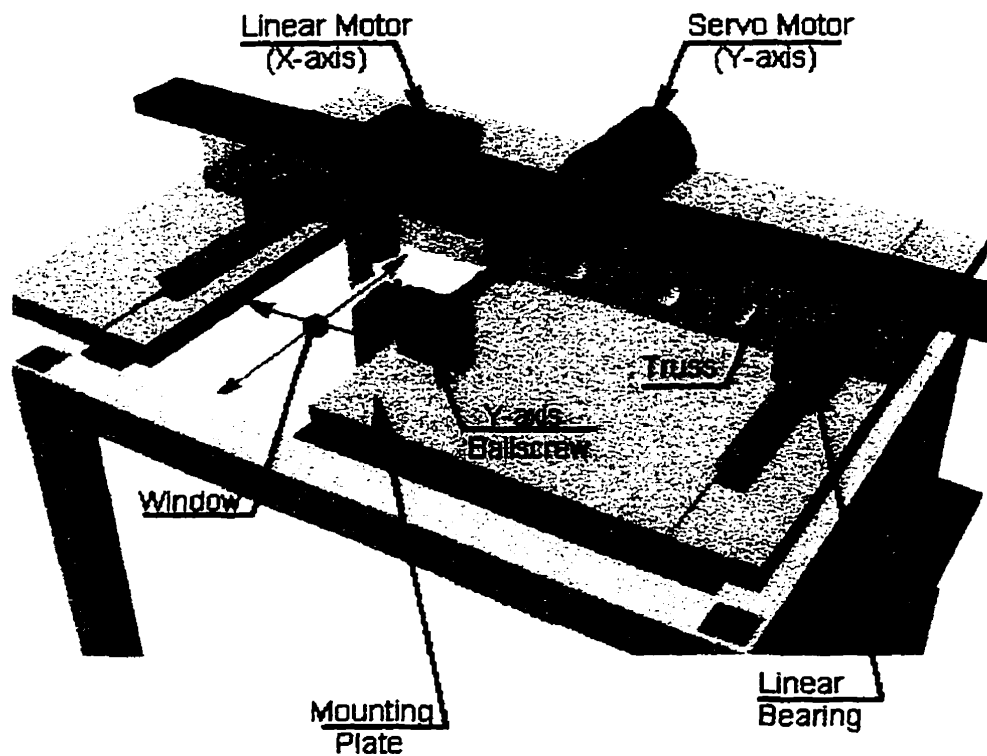


Figure 4.4. X-Y Motion System.

The linear motor is mounted on top of a truss, which has linear bearings on each end. The bearings' rails are mounted on an aluminum plate. The servo-motor's ballscrew

nut is mounted in the center of the truss, thus, reducing the possibility of jamming. Such an X-Y table configuration is widely used in industry, and, hence, is not assessed herein using the axiomatic approach to design.

The laser-light delivery subsystem is mounted on a bracket, which in turn is mounted on top of the linear motor. In order to provide the laser-light delivery-subsystem with access to the powder layer, a window has been provided in the X-Y table mounting plate.

#### **4.4.4 Vertical-Motion Subsystem**

The requirement for the Z-axis subsystem is to lower the platform, on which the part is built, by a controlled depth. The platform's motion must be parallel to the Z axis to provide the layer-thickness uniformity. Therefore, the FRs for the vertical-motion subsystem are:

FR41 = Move platform by specified distance, and

FR42 = Maintain parallel motion of the platform.

The motion of the platform is achieved by using a ballscrew, where the platform's bottom surface is coupled to the screw's nut, and the ballscrew's ends are installed in bearings. The ballscrew is driven by a PC-controlled stepper motor through a cogged belt. The processing chamber is rectangular, and the platform uses a rectangular seal to prevent the powder from entering the gap between the platform and the chamber's walls. The parallel motion of the platform is achieved by using rods, sliding in four linear bushings, Figure 4.5.

The DPs for this subsystem are:

DP41 = Ballscrew, and

DP42 = Guiding bushings.

The resulting design equation shows that the design is uncoupled:

$$\begin{Bmatrix} FR41 \\ FR42 \end{Bmatrix} = \begin{bmatrix} X & O \\ O & X \end{bmatrix} \begin{Bmatrix} DP41 \\ DP42 \end{Bmatrix} \quad (4.41)$$

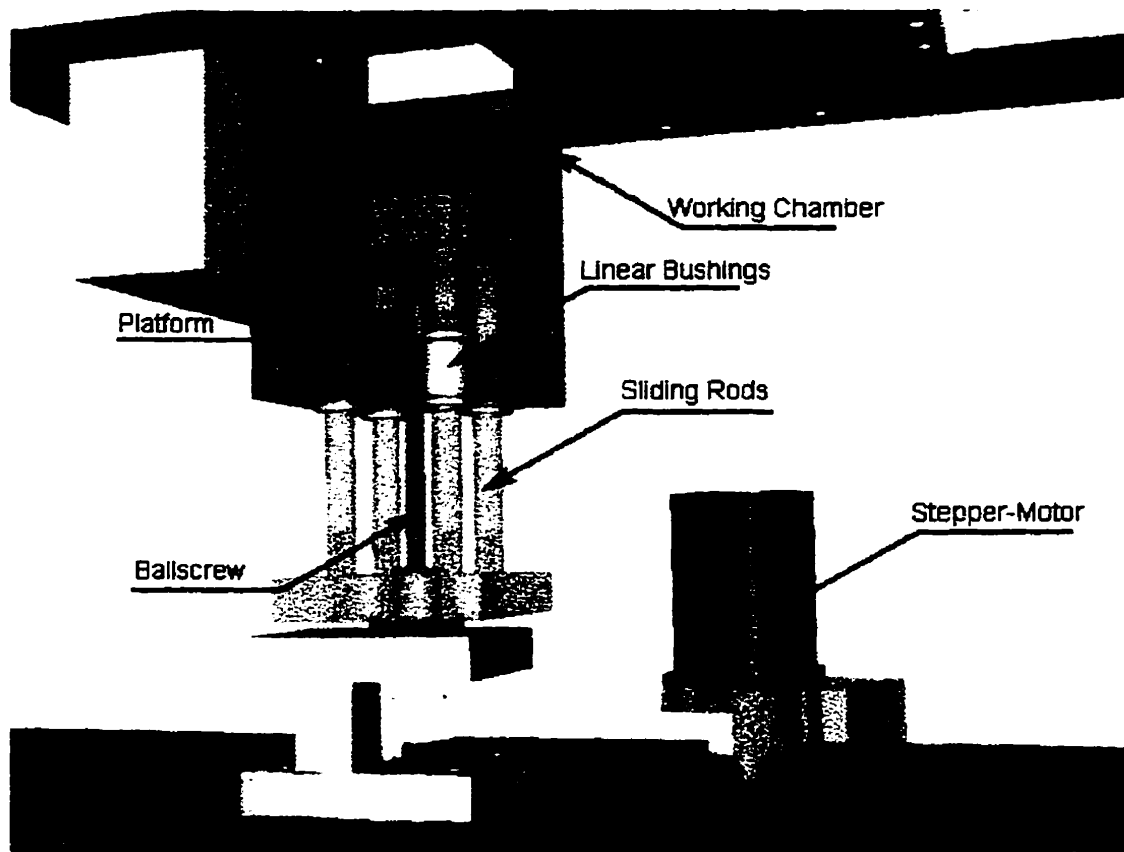


Figure 4.5. Vertical Motion Subsystem (Driving belt is not shown).

The overall system set-up is shown in Figures 4.6 and 4.7. It must be noted that, a powder-collecting chamber is included in the proposed design behind the processing chamber, Figure 4.6. Its purpose is to collect excessive powder for future re-use. The X-Y table mounting plate is shown as almost transparent in Figure 4.6.

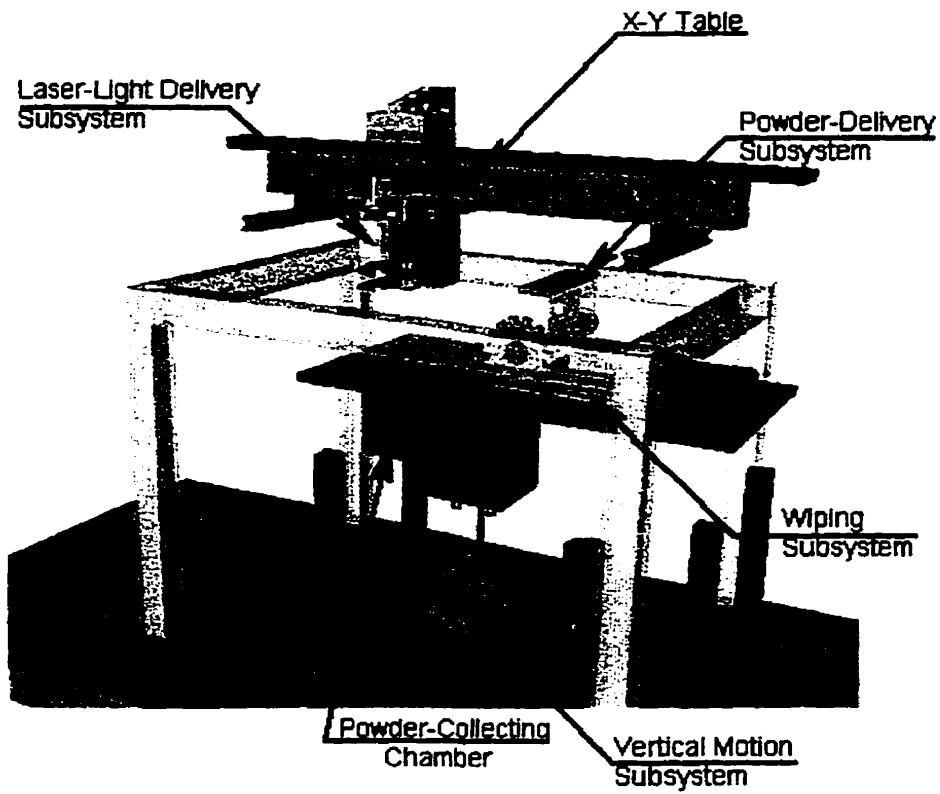


Figure 4.6. CAD Model of the Set-Up.

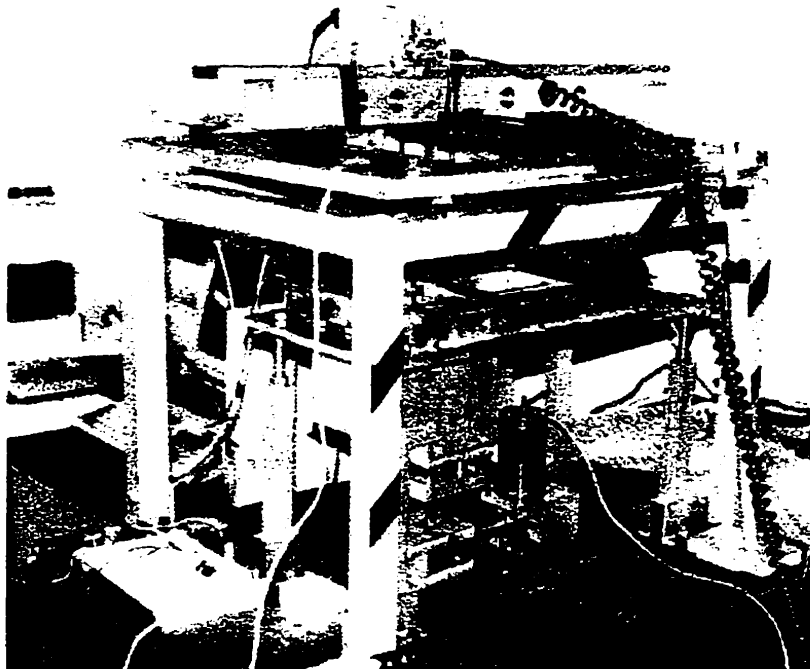


Figure 4.7. Photograph of the Assembled Set-Up.

## 5. EXPERIMENTS

In order to investigate the influence of scanning speed on the cladding's shape properties, two separate experimental studies were conducted: one for a pulsed laser, and another for a continuous laser.

### 5.1 Experiments with A Pulsed Laser

#### 5.1.1 Experimental Set-Up

The experimental setup for the pulsed-laser comprised: (i) a 1kW, Nd-YAG laser source, pulsed with the maximum rate of 20 Hz and power-on-period of 2.5 ms; (ii) optical devices, which focused a light spot of 0.5 mm on the powder's surface, located at a 100 mm distance; (iii) an aluminum process chamber with an acrylic observation window; and (iv) a three-axis CNC translation system, on which the process chamber was placed, Figure 5.1.

The 50 x 50 x 3 mm baseplates were made of AISI 316 Stainless Steel and installed at the bottom of the chamber for every experiment. The nominal composition of the AISI 316 Stainless Steel is given in Table 5.1 [31]. Water-atomized, AISI 316 Stainless Steel powder, with a particle size less than 45  $\mu\text{m}$  and an irregular particle shape, was used for producing claddings.

Table 5.1 Chemical Composition of AISI 316 Stainless Steel

	<b>Chromium</b>	<b>Nickel</b>	<b>Molybdenum</b>	<b>Carbon</b>	<b>Iron</b>
<b>Weight, %</b>	16.00-18.00	10.00-14.00	2.00-3.00	0.08	Balance

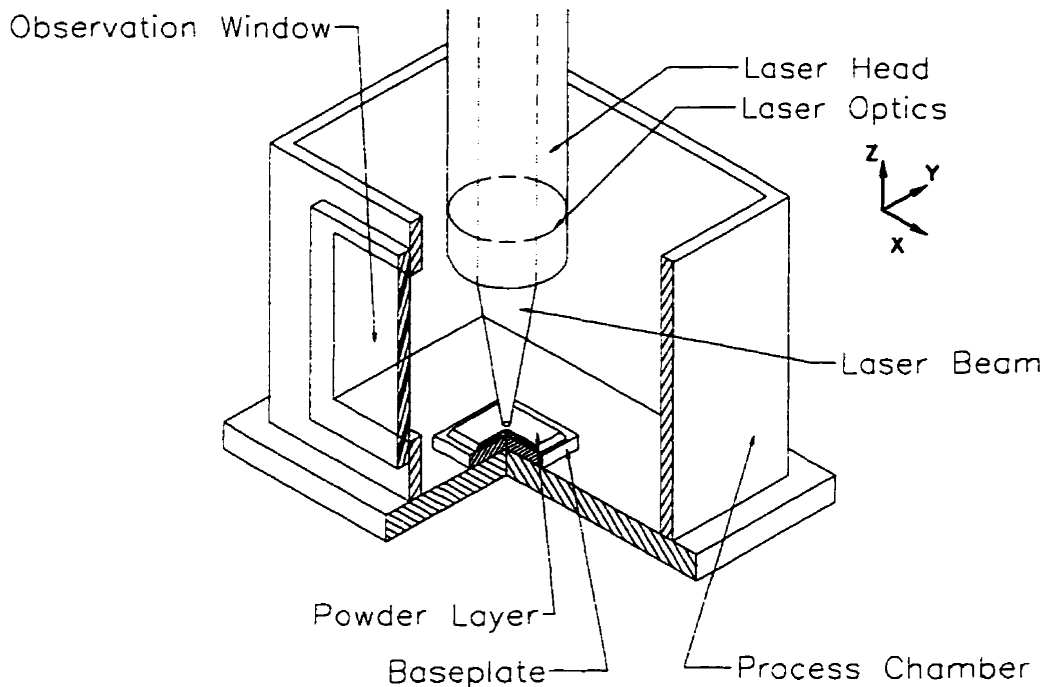


Figure 5.1. Experimental Set-Up for Pulsed-Laser Experiments.

### 5.1.2 Experimental Procedure

The following experimental procedure was used:

1. The laser power is set to 300 W, though its exact output could not be measured during the experiments due to the absence of a suitable power meter, and the pulsing rate is set to 14 Hz (maximum achievable for a 300 W power setting),
2. The process chamber is filled with Argon,
3. The powder is manually deposited onto the top surface of the baseplate and leveled accurately with a scraper blade, yielding a layer thickness of 0.5 mm, Figure 5.2, and
4. The powder layer is scanned with the laser beam.

A number of straight-line-claddings were produced at scanning speeds ranging from 1.27 mm/s to 6.35 mm/s. Also, in order to determine a working range for laser-power level, the laser-power level was varied from 250 W to 350 W.



The claddings' widths were measured using an optical microscope with a resolution of  $2.5\ \mu\text{m}$  in both the X and Y directions. The claddings' maximum heights were measured using a flat-tip dial indicator with a resolution of  $10\ \mu\text{m}$ . All measurements were made at  $0.1\ \text{mm}$  intervals along the claddings.

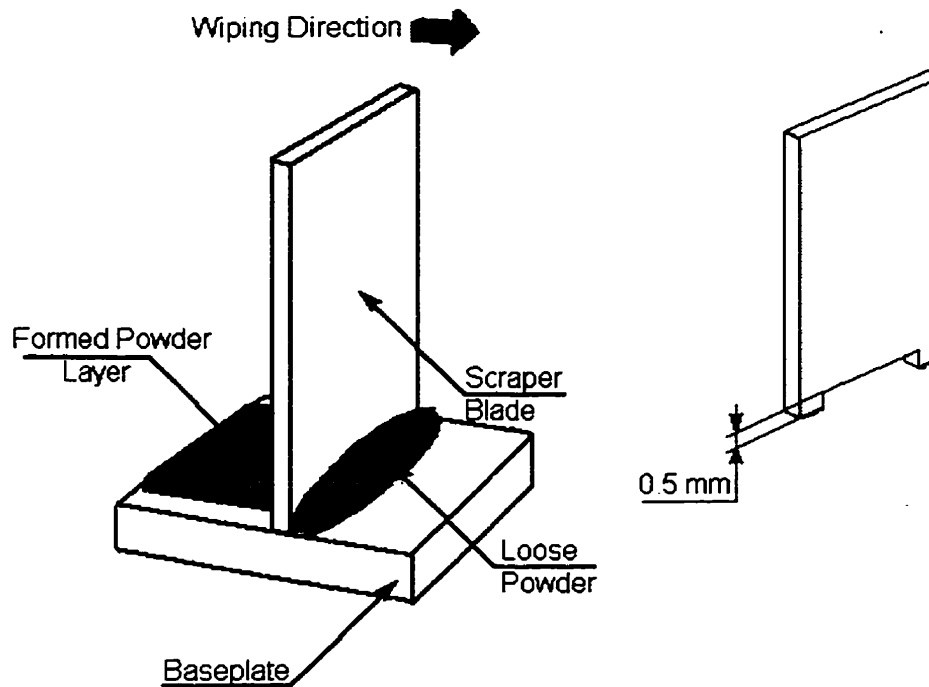


Figure 5.2. Powder Leveling.

The claddings were also cross-sectioned both in the normal and parallel planes to the scanning direction. They were etched using 10% ocelic acid in order to reveal molten zones in the cladding as well as in the baseplate.

### 5.1.3 Experimental Results

For each setting of the scanning speed, five lines were fabricated. Two typical cross-sections, normal and parallel to the scanning direction, are shown in Figures 5.3 and 5.4, respectively. In Figure 5.3, it is seen that the claddings tend to have a spherical shape and that the molten zone penetrates into the baseplate.

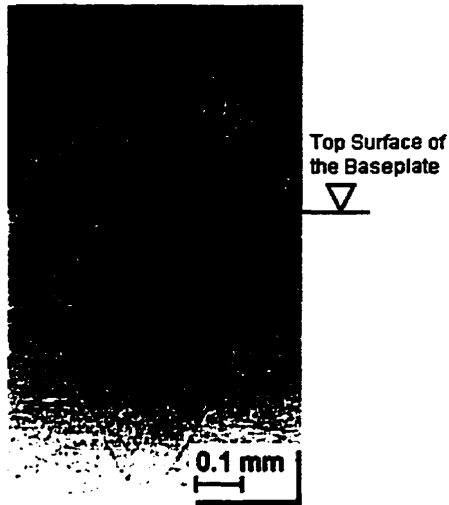


Figure 5.3. Typical Cladding's Cross-Section for Pulsed Laser.

In Figure 5.4, it is seen that the molten zones, produced by single pulses, can be distinguished from each other. This observation supports the results of process simulation, reported in Chapter 3.4, indicating that the mass built by a single pulse solidifies before the next pulse is applied. Also, the molten-zones' boundaries above the baseplate are almost vertical. This observation, in turn, supports the assumption of the molten-zone's cylindrical shape made during the simulations in Section 3.5.2.

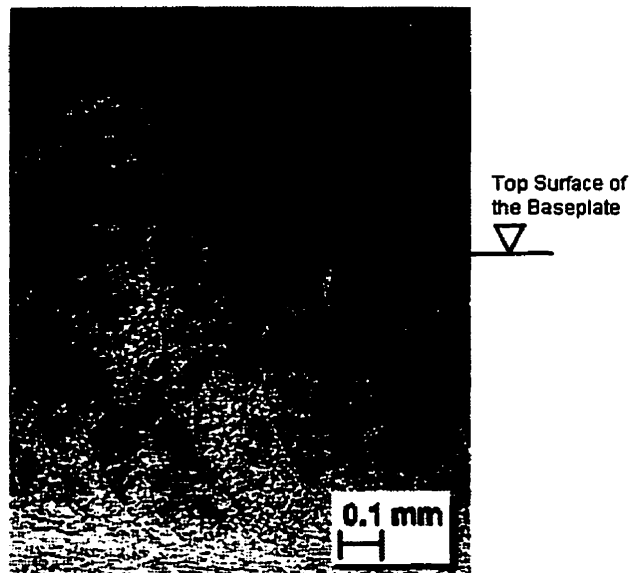


Figure 5.4. Typical Cladding's Longitudinal-Centerline Section for Pulsed Laser.

The claddings' average widths and heights (calculated using over 100 measurements per line) are plotted versus the scanning speed in Figures 5.5 and 5.6, respectively. Figure 5.5 shows that the cladding width decreases with increasing scanning speed. Also, the variability of the measured cladding width increases with increasing scanning speed.

During the experiments, it was observed that the molten metal departs from the layer surface in the form of small particles (sparks), possibly due to evaporation-recoil pressure, where some may randomly land and adhere to the cladding's surface. This may be one of the mechanisms causing variability. Furthermore, a larger variation in the cladding width with increasing speed can be due to the fact that the centers of individual spherical masses, built by single pulses, are located further apart. For example, at the fastest speed used, 6.35 mm/s, the spherical masses are only loosely connected.

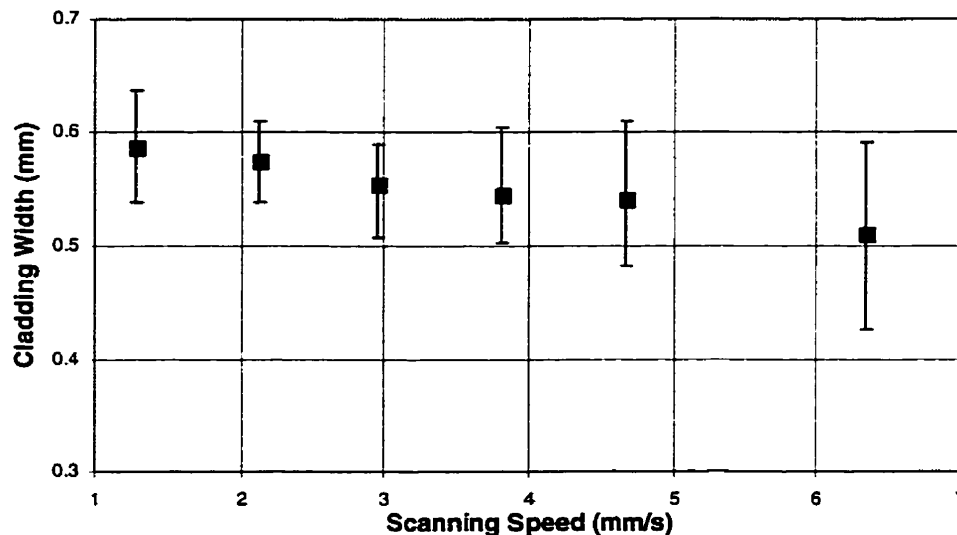


Figure 5.5. Cladding Width versus Scanning Speed for Pulsed-Laser Experiments.

Figure 5.6 shows that the cladding height decreases with increasing scanning speed. The large variations in the cladding height can also be explained by the

evaporation mechanism discussed above. Furthermore, the powder's porous nature may have also influenced this variability. The width of the cladding, on the other hand, is defined mostly by the laser-beam diameter, and thus would not be affected by the presence of pores in the powder.

Since the cladding-height measurements were acquired using a dial indicator with a flat tip, whose diameter was larger than the distance between the masses' centers, some variability was filtered out for higher-scanning-speed claddings.

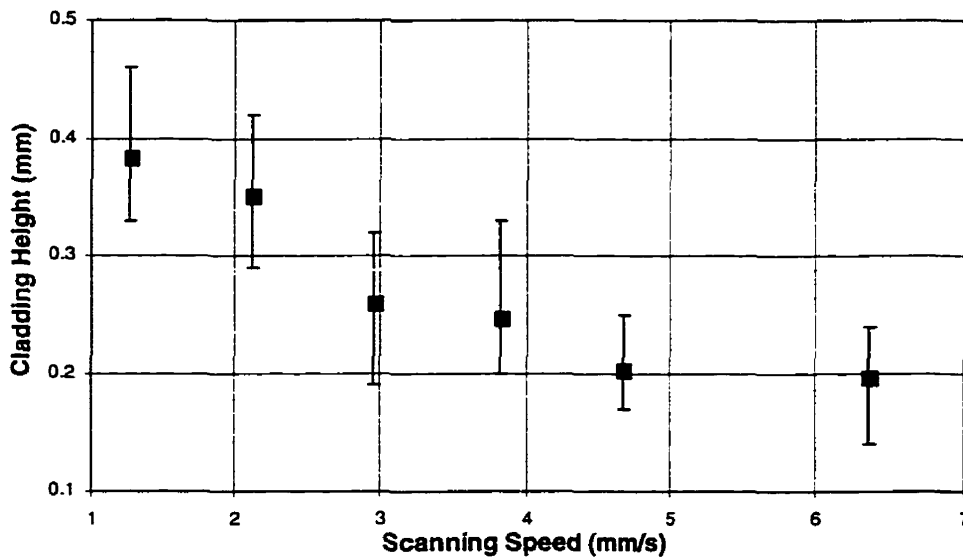


Figure 5.6. Cladding Height versus Scanning Speed for Pulsed-Laser Experiments.

The cladding's average widths and heights are plotted versus the laser-power level in Figures 5.7 and 5.8, respectively. Figure 5.7 shows that the cladding width increases with increasing laser-power level. The variability of the layer width is the largest for the lowest setting of the laser-power level. During the experiments, it was observed that with a low laser-power level the process becomes unstable, since the claddings do not bond to the baseplate. This results in higher variability. On the other hand, as the power-level

increases, the evaporation process discussed above becomes more noticeable. Eventually, an increase of the power level beyond a threshold results in the cutting of the baseplate.

Figure 5.8 shows that the cladding height decreases with increasing laser-power level.

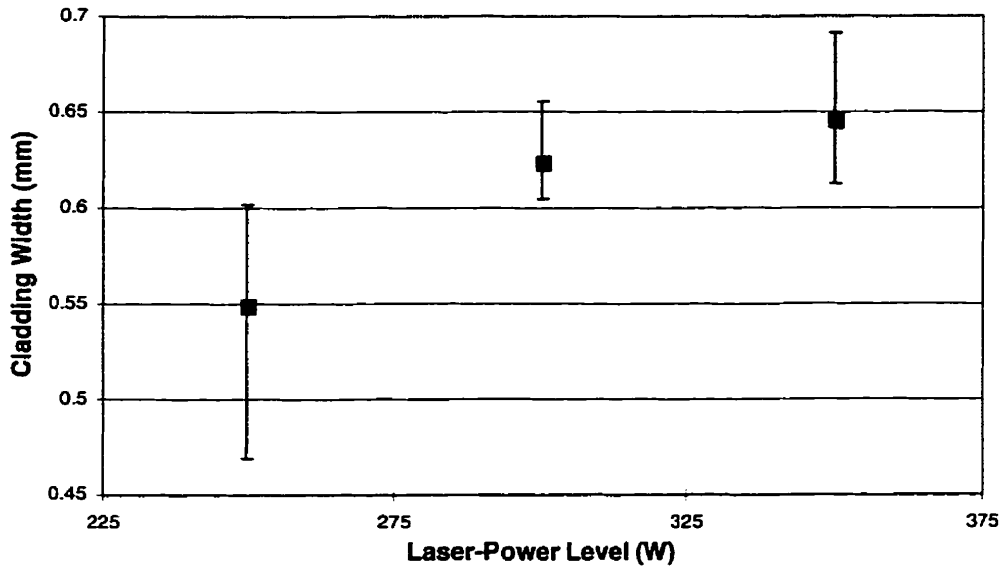


Figure 5.7. Cladding Width versus Laser-Power Level for Pulsed-Laser Experiments.

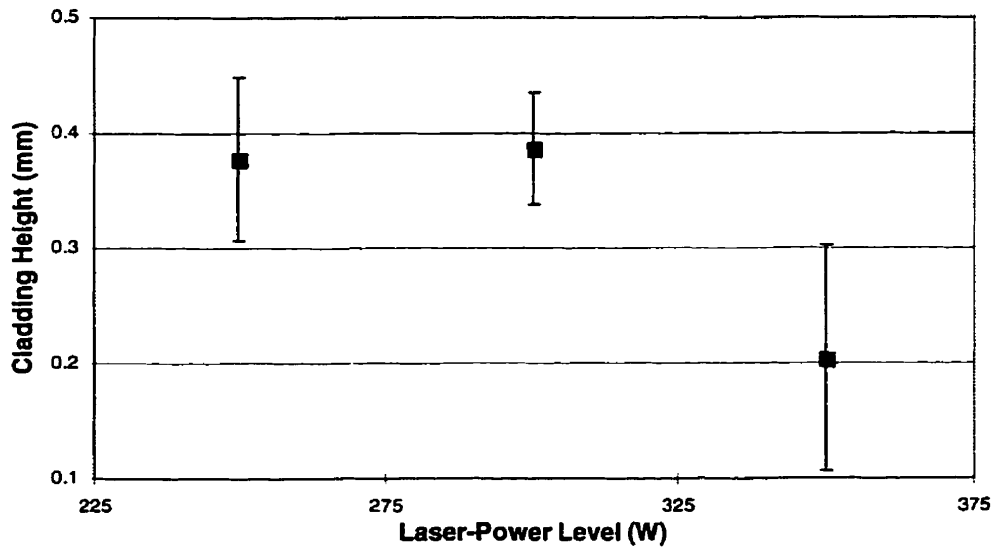


Figure 5.8. Cladding Height versus Laser-Power Level for Pulsed-Laser Experiments.

This phenomenon is due to a large increase in the corresponding cladding width, where the overall volume of the powder available for the cladding's building does not

change significantly. The variability of the cladding height is large for the both smallest and largest settings of the laser-power level.

#### 5.1.4 Comparison to Simulation Results

The experiments for the pulsed-laser were carried out with a powder-layer thickness of 0.5 mm due to system's physical limitations, whereas the process simulation was performed for a powder-layer thickness of 0.3 mm, since this value is our target for the continuous-laser based system developed at the University of Toronto.

Therefore, in order to employ only one finite-difference model for both laser-working modes and compare only fundamental relationships, i.e., trends, the process simulations were carried out at a powder-layer thickness targeted for the continuous laser.

As seen in Figure 5.9, for the pulsed-laser operating at 14 Hz frequency, the experimental and simulation results, yield similar trends for the cladding width versus scanning speed relationship.

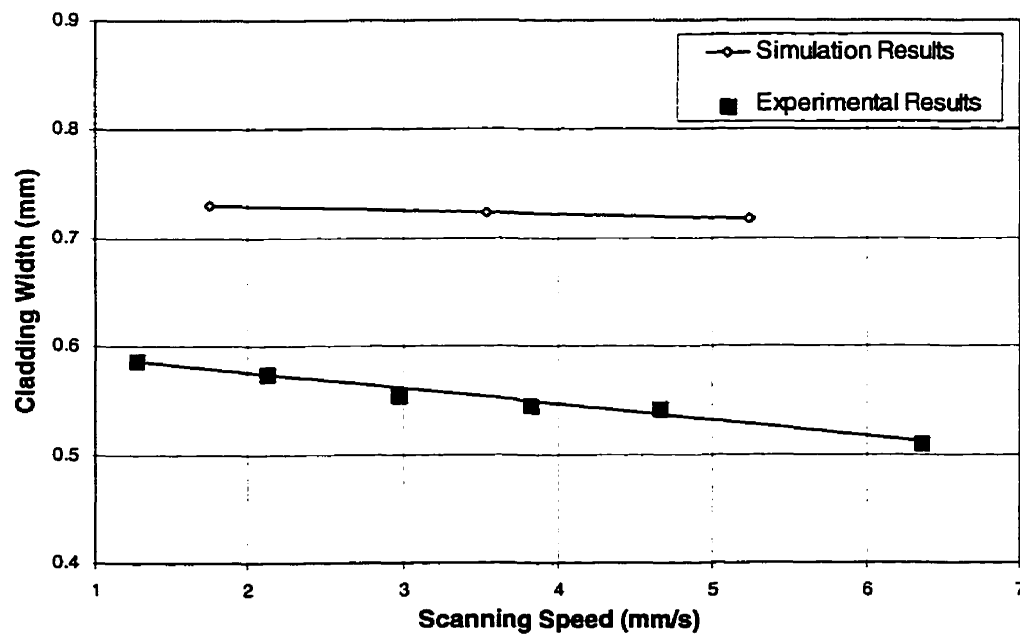


Figure 5.9. Experimental versus Simulation Results for Cladding-Width Measurements.

In order to compare the relationships between the cladding height and the scanning speed, the experimental and simulation results were normalized. All cladding-height measurements were divided by the original height of the powder layer. As seen in Figure 5.10, the experimental and simulation results also agree on the fundamental characteristic of the relationship between the scanning speed and the cladding height. The difference in the slopes of the two curves may be due to several approximations made during process simulation.

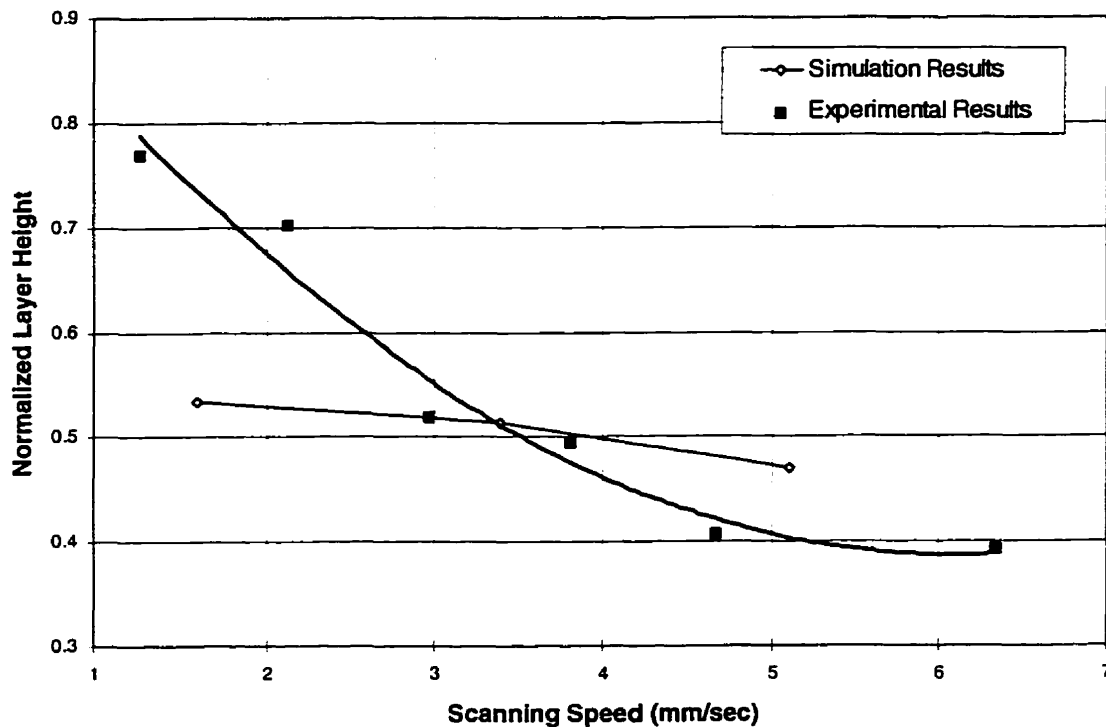


Figure 5.10. Experimental versus Simulation Results for Cladding-Height Measurements.

## 5.2 Experiments with a Continuous Laser

### 5.2.1 Experimental Set-Up

The experimental set-up for the continuous-laser system comprised: (i) the experimental part-fabrication prototype described in Chapter 4; (ii) a continuous, 150 W, Nd-YAG laser; (iii) a fiber-optical cable of 0.6 mm diameter coupled to focusing optics,

which together yielded a laser spot of 0.6 mm on the powder-layer's surface located at 50 mm distance; and (iv) a process-control PC.

At the preliminary stage of the experimentation, the dimensions of the baseplate were the same as those used for the pulsed-laser experiments. However, the laser was unable to selectively melt the powder and yield useful cladding. Therefore, much smaller baseplates (20 x 4 x 1.2 mm) were used.

### 5.2.2 Experimental Procedure

The following experimental procedure was used:

1. The laser power is set to 150 W. (However, the measured output from the light-delivery system was only 90-100 W due to optical losses during the experiments),
2. The process chamber is filled with Argon,
3. The powder is deposited onto the top surface of the baseplate using powder-delivery subsystem of the experimental prototype. The powder is leveled with a roller, yielding a powder-layer thickness of 0.3 mm, and
4. The powder layer is scanned with the laser beam.

Two straight-line claddings were scanned at 1 mm/s, and two at 1.76 mm/s scanning speed. (With a further increase in the scanning speed, the claddings did not bond to the baseplate). The claddings' widths and heights were measured using the same procedure as in case of the pulsed laser.

The claddings were cross-sectioned normal to scanning direction for determination of their general shape. Two cross-sections for each cladding were produced. One at the visible beginning of the cladding, and another at a distance of 2 mm along the scanning path.



### 5.2.3 Experimental Results

A typical cladding's appearance is shown in Figures 5.11 and 5.12, at 90° and 45° from the horizontal line, respectively. The (dark color) cladding is surrounded by sintered powder in both figures. As expected, the cladding's surface is smoother than those produced by a pulsed laser.



Figure 5.11. Top View of Cladding.

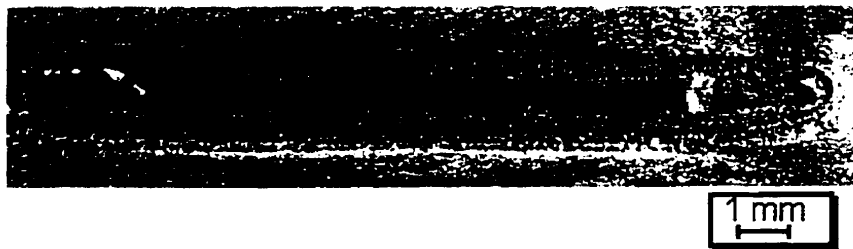


Figure 5.12. 45° View of Cladding.

The cladding's cross-sections, at the beginning and 2 mm from the beginning, are shown in Figures 5.13 and 5.14, respectively. It can be seen that claddings are not fully-bonded to the baseplate due to inadequate laser irradiance.

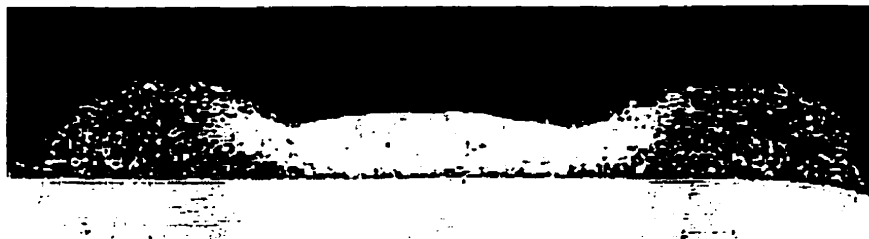


Figure 5.13. Cladding's Cross-Section in the Beginning.

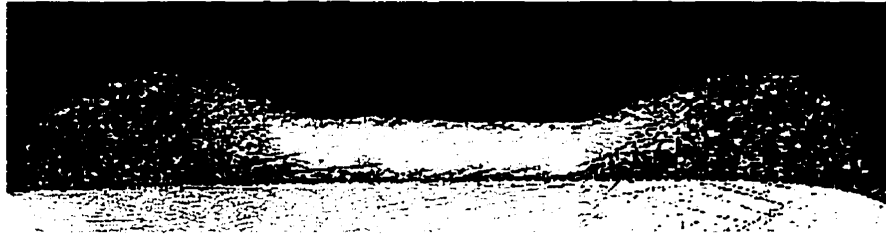


Figure 5.14. Cladding's Cross-Section 2 mm from the Beginning.

The claddings' average widths and heights (for 10 measurements per line) are plotted versus the scanning speed in Figures 5.15 and 5.16, respectively. Figure 5.15 shows that the cladding width decreases with increasing scanning speed. Large cladding-width variations are associated with the higher scanning speed due to inadequate laser-power level.

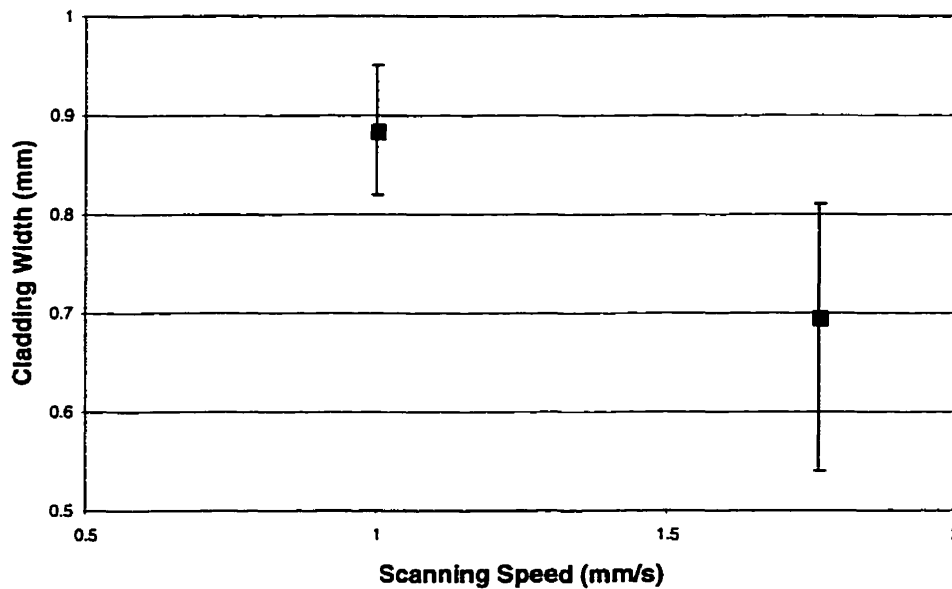


Figure 5.15. Cladding Width versus Scanning Speed for Continuous-Laser Experiments.

Figure 5.16 shows that average cladding height remains almost constant with increasing scanning speed. However, one must note that the experimental cladding-height measurements were normalized, since the measurements of the remaining sintered powder layers showed that their thicknesses were different (0.36 and 0.22 mm,

respectively). This discrepancy is expected since the first several layers of any layered-manufacturing process fluctuate in height [38]. In all processes, the plate, on which a part is built, is lowered only by an approximate distance, since exact measurements are impractical to carry out. All cladding-height measurements were divided by corresponding sintered powder-layer thickness.

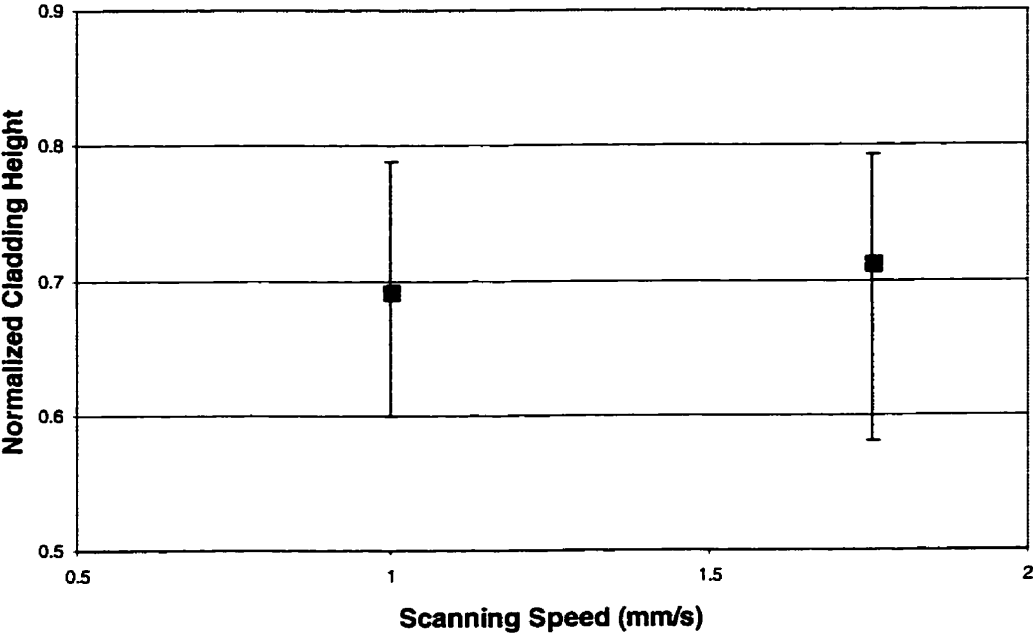


Figure 5.16. Cladding Height versus Scanning Speed for Continuous-Laser Experiments.

### 5.2.4 Comparison to Simulation Results

As seen in Figure 5.17, experimental and simulation results for the continuous laser, yield very similar trends for the cladding width versus scanning speed relationship.

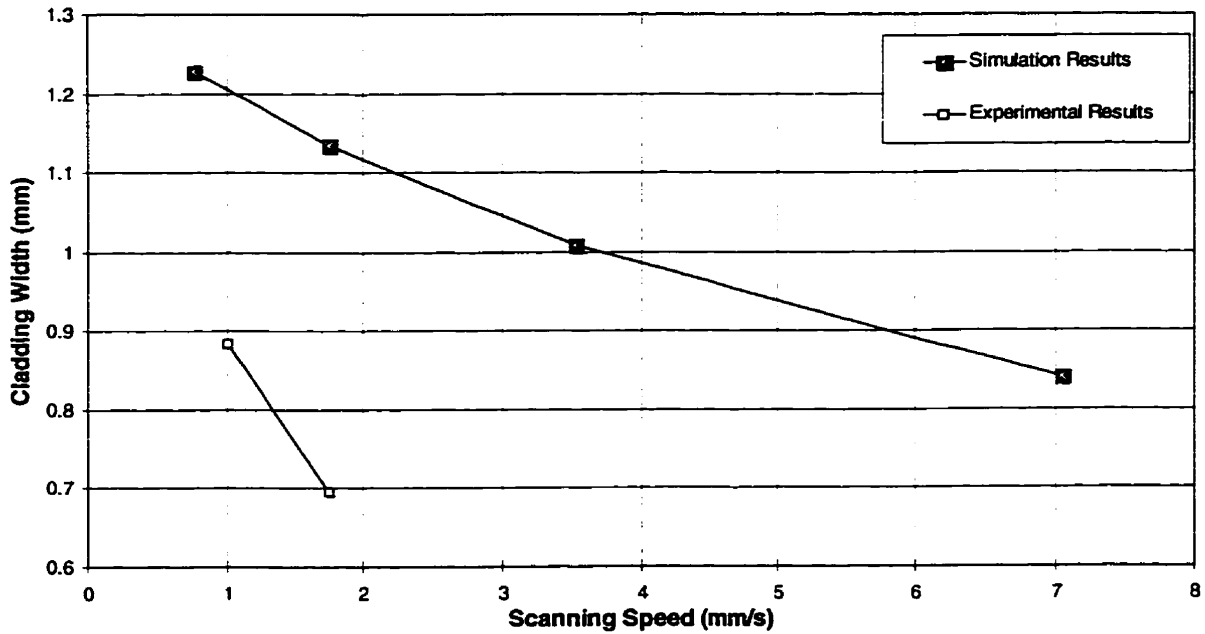


Figure 5.17. Experimental versus Simulation Results for Cladding-Width Measurements. Continuous Laser.

Figure 5.18 shows that the experimental and simulation results do not agree on the character of the relationship of cladding height versus scanning speed. However, it must be noted that the two scanning speeds used in the experiments were very close. Thus, any serious conclusions about the actual relationship between cladding's geometrical properties and process parameters could not be made at this point. The experimental process needs refinement in order to verify the findings of the process simulation.

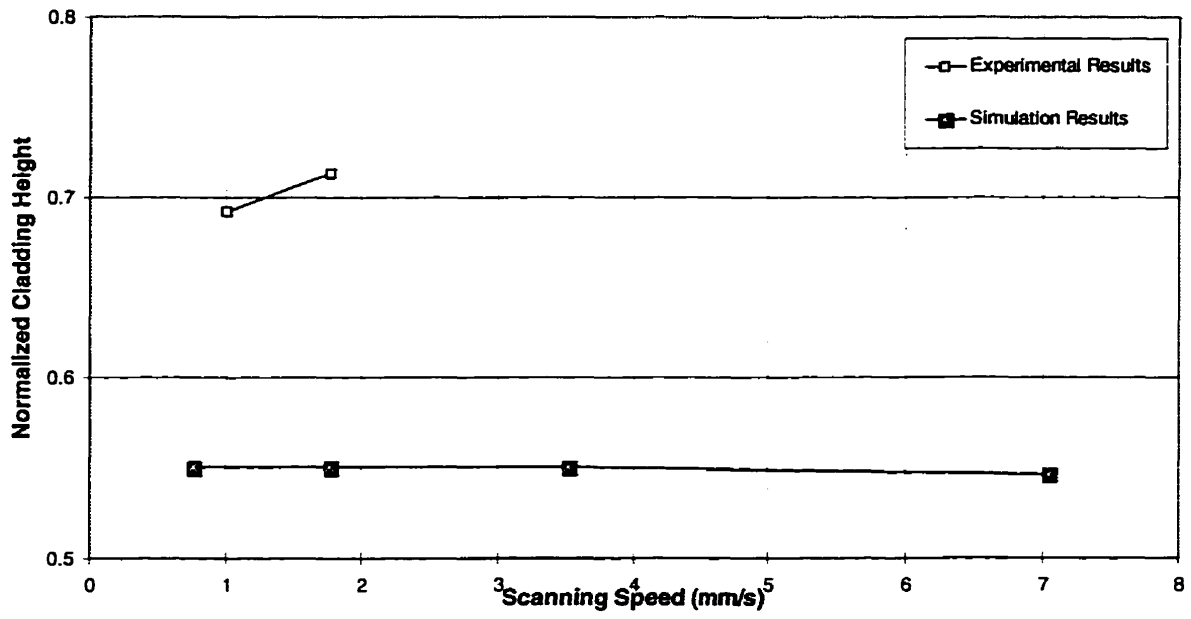


Figure 5.18. Experimental versus Simulation Results for Cladding-Height Measurements. Continuous Laser.

## 6. CONCLUSIONS

### 6.1 Summary

The primary goal of this thesis was envisioned as the determination of the relationships between the process parameters of a proposed metal-based layered RM technique and the geometrical-shape properties of the layers. Subsequently, the two main research tasks were set as: (i) process modeling and computer simulation; and, (ii) preliminary experimental verification via a prototype RM system design.

Process modeling and computer simulations were performed for single-cladding building with two possible laser modes - pulsed and continuous. The governing phenomenon in the modeled process was heat propagation in a two-material system, i.e., powder and solid substrate. The finite-difference technique was utilized for determination of the global temperature fields, and the thermophysical properties of the powder. Subsequently, the cladding's geometrical properties, namely its width and height, were determined using analytical geometry.

In order to verify the findings of the process simulations, experimental set-ups for both modes of the laser operation were built. Numerous straight-line claddings were fabricated and their geometrical properties were measured. The experimental and process-simulation results showed good agreement in terms of qualitative relationships between process parameters and cladding's geometrical properties.

The process simulations also indicated the superiority of the continuous laser over a pulsed one in terms of the cladding-building speed and cladding-surface quality. The continuous-laser claddings achieved geometrical properties comparable to those of a pulsed-laser, but could be produced at much higher scanning speeds.

## 6.2 Conclusions

The overall objective of the thesis, i.e., determining the effect of process parameters on the cladding geometry, was successfully achieved. The pulsed-laser process simulation results were in good agreement with the experiments. However, due to the limited laser power of the prototype system, we were unable to vary the process parameters sufficiently in order to evaluate the process simulation results for a continuous laser. One can also note, however, that the experiments not only supported the findings of the process simulation, but they also demonstrated feasibility of the proposed RM process.

The computer-modeling and process-simulation procedures developed in this thesis can serve as tools for further investigation into the proposed RM process. Simulations provide us with a better understanding of the heat propagation mechanism, which is the fundamental physical phenomenon in the RM process.

The analytical model of the process can be utilized in the future to model and investigate subsequent fabrication steps, e.g., inter-cladding and inter-layer bonding. The first step in such an investigation would be the modeling of a multi-cladding-building environment, where additional new powder is deposited onto the layer under construction after every single-cladding fabrication step and the laser-beam selectively melts the new cladding-line adjacent to a previously-built one. The next investigative step would be determination of the multi-cladding-layer's geometrical properties based on the global temperature fields.

### **6.3 Recommendations**

The work reported in this thesis can be extended in several directions. Firstly, additional work is needed in order to refine the heat-transfer model used for the computer simulations. This would include accounting for the phase change and effects of the latent heat, as well as relaxing some of the approximations made in the determination of the shape properties. The current analytical model is built on the assumption that the molten zone has a cylindrical shape. An analytical model based on a conical shape of the molten zone is recommended for the further investigation, as being closer to the reality (as noted during the experiments).

Secondly, the experimental prototype system must be improved by either increasing the available continuous-laser power, or by decreasing the focal spot size in order to bring the irradiance of the laser beam to an acceptable level for building fully-densed and -bonded claddings. The fundamental aspects of building multi-cladding layers and multi-layered parts must also be investigated. These include inter-cladding and inter-layer bonding considerations, investigation of building procedures for complex 3D-structures, i.e., parts with inclined features and overhangs, and overall examination of the influence of laser-scanning and powder-replenishment procedures on the layer's geometrical properties.

Finally, the success of any rapid layered manufacturing process primarily depends on the mechanical properties of its output parts. It is conjectured herein that fully-densed metal parts manufactured via the process proposed in this thesis will have mechanical properties acceptable by the receptive industry. This claim however must be proven by additional research following this thesis.



## REFERENCES

- [1] C. Dawes, **Laser Welding**, Abington Publishing, 1992.
- [2] P. F. Jacobs, **Stereolithography and Other RP&M Technologies** SME, 1996.
- [3] S. Ashley, "Rapid Prototyping is Coming of Age", *Mechanical Engineering*, July 1995, pp. 63-68.
- [4] M. L. Murphy, W. M. Steen, C. Lee, "The Rapid Manufacture of Metallic Components by Laser Surface Cladding", *Laser Assisted Net Shape Engineering, Proceedings of the LANE'94*, Erlangen, Germany, Vol. II, October 1994, pp. 803-814.
- [5] W. Konig, T. Celiker, Y.-A. Song, "Process Development for Direct Manufacturing of Metallic Parts", *Laser Assisted Net Shape Engineering, Proceedings of the LANE'94*, Erlangen, Germany, Vol. II, October 1994, pp. 785-792.
- [6] J. L. Koch, J. Mazumder, "Rapid Prototyping by Laser Cladding", *Proceedings of International Conference on Applications of Lasers and Electro-Optics (ICALEO)*, Orlando, FL, October 1993, pp. 556-565.
- [7] R. Mah, "Directed Light Fabrication", *Advanced Materials and Processes*, Vol. 151, No. 3, March 1997, pp. 31-33.
- [8] S. Ashley, "From CAD Art to Rapid Metal Tools", *Mechanical Engineering*, March 1997, pp. 82-87.
- [9] P.M. Dickens, M. S. Pridham, R. C. Cobb, and I. Gibson, "3D Welding", *Proceedings of the 1<sup>st</sup> European Conference on Rapid Prototyping*, Nottingham, UK, July 1992, pp. 81-84.

- [10] K. Hartmann, R. Krishhan, R. Merz, G. Neplotnik, F. B. Prinz, L. Shultz, M. Terk, and L. E. Weiss, "Robot-Assisted Shape Deposition Manufacturing," *Proceedings of the 1994 IEEE International Conference on Robotics and Automation*, IEEE, San Diego, May 1994, Vol. 4, pp. 2890-2895.
- [11] M. L. Griffith, D. M. Keicher, C. L. Atwood, J. A. Romero, J. E. Smugeresky, L. D. Harwell, D. L. Greene, "Free Form Fabrication of Metallic Components Using Laser Engineered Net Shaping (LENS)", *1996 Solid Freeform Fabrication Conference Proceedings*, Austin, TX, pp. 125-131.
- [12] D. Radaj, **Heat Effects of Welding**, Springer-Verlag, 1992, New York, NY.
- [13] H. S. Carslaw, J. C. Jaeger, **Conduction of Heat in Solids**, 2nd Ed. Oxford, University Press, 1959.
- [14] A. Kar, J. Mazumder, "Modeling in Laser Materials Processing: Melting, Alloying, Cladding", **Laser Processing: Surface Treatment and Film Deposition**, J. Mazumder - Editor, Kluwer Academic Publishers, Netherlands, 1996, pp. 129-155.
- [15] F. Lemoine, D. F. Grevey, A. B. Vannes, "Cross-Section Modeling of Pulsed Nd-YAG Laser Cladding", in *Laser Materials Processing and Machining, Proceedings of SPIE No. 2246*, 1994, pp. 37-45.
- [16] R. Colaco, L. Costa, R. Guerra, R. Vilar, "A Simple Correlation between the Geometry of Laser Cladding Tracks and the Process Parameters", **Laser Processing: Surface Treatment and Film Deposition**, J. Mazumder - Editor, Kluwer Academic Publishers, Netherlands, 1996, pp. 421-429.
- [17] V. M. Weerasinge, W. M. Steen, "Computer Simulation Model for Laser Cladding" **Transport Phenomena in Materials Processing**, *Winter Annual Meeting of ASME*, Boston, MA, 1983, pp. 15-23.

- [18] A. F. A. Hoadley, C. F. Mardsen, M. Rappaz, "A Computer Study of the Laser Cladding Process" **Modeling of Casting, Welding and Advanced Solidification Processes V**, *Proceedings of the Fifth International Conference on Modeling of Casting and Welding Processes*, Davos, Switzerland, 1990, pp. 123-130.
- [19] H. Haferkamp, F.-W. Bach, F. von Alvensleben, J. Gerken, " Laser Prototyping: Metal Models in Minutes" *Photonics Spectra*, May 1996, pp. 122-124.
- [20] F. Klocke, H. Wirtz, "Direct Manufacturing of Metal Prototypes and Prototype Tools", *1996 Solid Freeform Fabrication Conference Proceedings*, Austin, Texas, pp. 141-147.
- [21] L. A. Killander, "Future Direct Manufacturing of Metal Parts, with Free Form Fabrication" *Annals of the CIRP*, Vol. 44, No.1, 1995, pp. 451-454.
- [22] F. Hensel, C. Binroth, G. Sepold, "A Comparison of Powder- and Wire-Fed Laser Beam Cladding", **Laser Treatment of Materials**, DGM GmbH, Germany, 1992, pp. 39-45.
- [23] M. Von Allmen, **Laser-Beam Interaction with Materials**, 2<sup>nd</sup> Ed., Springer-Verlag, NY, 1995.
- [24] Y. Arata, I. Miyamoto, "Some Fundamental Properties of High Power Laser Beam as a Heat Source (Report 3: Metal Heating by Laser Beam)", in **Plasma, Electron and Laser Beam Technology**, American Society for Metals, Metals Park, Ohio, 1986, pp. 245-263.
- [25] A. Sajak, **Ferrous Powder Metallurgy**, Cambridge, 1995.
- [26] J. P. Holman, **Heat Transfer**, 7<sup>th</sup> Ed., McGraw-Hill, 1990.
- [27] I-DEAS TMG On-line manual, Chapter "Thermal Modeling Theory".

- [28] A. M. Prokhorov, V. I. Konov, L. Ursu, I. N. Mihailescu, **Laser Heating of Metals**, Adam Hilger, NY, 1990.
- [29] Y. S. Touloukian, Ed. “**Thermophysical Properties of High-Temperature Solid Materials. Vol. 3: Ferrous Alloys**” Macmillan Publishing, NY, 1967.
- [30] T. Watanabe, Y. Yoshida, “Weldability of Stainless Steel with the YAG Laser Beam and a Presumption of Weld Strength by Numerical Analysis”, *Proceedings of the Fifth International Conference on Modeling of Casting and Welding Processes*, Davos, Switzerland, 1990, pp. 173-184.
- [31] E. A. Avallone, T. Baumeister, (ed.), **Marks’ Standard Handbook for Mechanical Engineers**, 10<sup>th</sup> Ed., McGraw-Hill, 1996.
- [32] S. W. Churchill, “The Thermal Conductivity of Dispersions and Packed Beds - an Illustration of the Unexploited Potential of Limiting Solutions for Correlation”, in **Advances in Transport Processes**, Vol. 4, J. Wiley, 1986, pp. 394-418.
- [33] M. R. Spiegel, **Schaum’s Outline Series. Mathematical Handbook**, McGraw-Hill, 1996.
- [34] M. Ya. Vigodsky, **Spravotchnik po Visheii Matematike**, (Handbook of Advanced Calculus), in Russian, Fizmatgiz, Moscow, 1961.
- [35] **The Student Edition of MATLAB. Version 4. User’s Guide**, Prentice-Hall, 1995.
- [36] N. P. Suh, **The Principles of Design**, Oxford University Press, New York, 1990.
- [37] B. Van der Schueren, J. P. Kruth, “Powder Deposition in Selective Metal Powder Sintering”, *Rapid Prototyping Journal*, Vol.1, No. 3, 1995, pp. 23-31.
- [38] K. Rehap, J. P. Kruth, “Recoating Issues in Stereolithography”, *Rapid Prototyping Journal*, Vol. 1, No. 3, 1995, pp. 4-16.

## APPENDIX A: Thermal Modeling with I-DEAS TMG

The I-DEAS model files with finite-difference models used in this thesis are located in *cad1/yevko* directory. Their names are:

1. *TMG\_Gr\_Zero\_Pulsed\_Rate.mf1* and *.mf2* - the model for pulsed laser,
2. *TMG\_Gr\_Zero\_Contin.mf1* and *.mf2* - the model for continuous laser with 0.75 mm/s scanning speed,
3. *TMG\_Gr\_Zero\_Con\_2Speed.mf1* and *.mf2* - the model for continuous laser with 3.52 mm/s scanning speed, and
4. *TMG\_Gr\_Zero\_Con\_3Speed.mf1* and *.mf2* - the model for continuous laser with 7.04 mm/s scanning speed.

The generic procedure for a thermal modeling is as follows:

1. Create a new model file,
2. Create a solid model of the physical system,
3. Mesh the model,
4. Create a set of boundary conditions,
5. Set analysis options, and
6. Solve the model.

The creation of a model and its meshing is described in detail in “I-DEAS Master Series. Student Guide” by SDRC. Additional information can be gathered from I-DEAS on-line manual. Only the aspects of the thermal modeling procedure relevant to this thesis are reported herein. In order to carry out a thermal modeling, the I-DEAS “Simulation” application must be used.

## A.1 Model Meshing

An issue not covered in the above mentioned literature is the creation of the two-material system. For this purpose, the solid model must be either partitioned or new elements (in case of a simple model geometry) must be extruded. The model used in this thesis was created by the latter method, where a sub-application “Meshing” is used.

The first step is the creation of the baseplate’s solid-model. Next, the top surface of the baseplate is meshed with thin-shell elements. The mapping of the surface is used for this purpose. The desired number of rectangular elements is specified for each edge. Subsequently, the software automatically creates the mesh.

The solid elements are created by the extrusion of the shell elements. The extrusion procedure is as follows:

1. In I-DEAS command prompt, type *element*, *multiple\_create*, *extrude*, and *translate*.

Each command must be followed by *Enter*,

2. When the software asks for element type, choose *solid* from the menu,

3. Choose free faces from the model,

4. Define element thickness,

5. Define labels for new elements and nodes,

6. Define material, and

7. Define number of copies, i.e., layers with desired thickness, to be produced.

In order to generate surface-coating elements, which are necessary for convection modeling, type *surface\_coating* after *element* and *multiple\_create*. The rest is the same as for element extrusion.

The models used in this thesis have two materials, defined in the model files. The *SS316* corresponds to AISI316 stainless steel, and *Powder45* to AISI316 stainless steel powder with particle size of 45  $\mu\text{m}$ .

## A.2 Boundary Conditions

### A.2.1 Heat Load

The rest of the thermal analysis is performed using “TMG Thermal Analysis” sub-application. The first step in defining boundary conditions is the definition of heat loads.

The following procedure is used:

1. Picking the *Heat Load* icon, Figure A.1, will bring up the heat-load dialog box, Figure A.2,

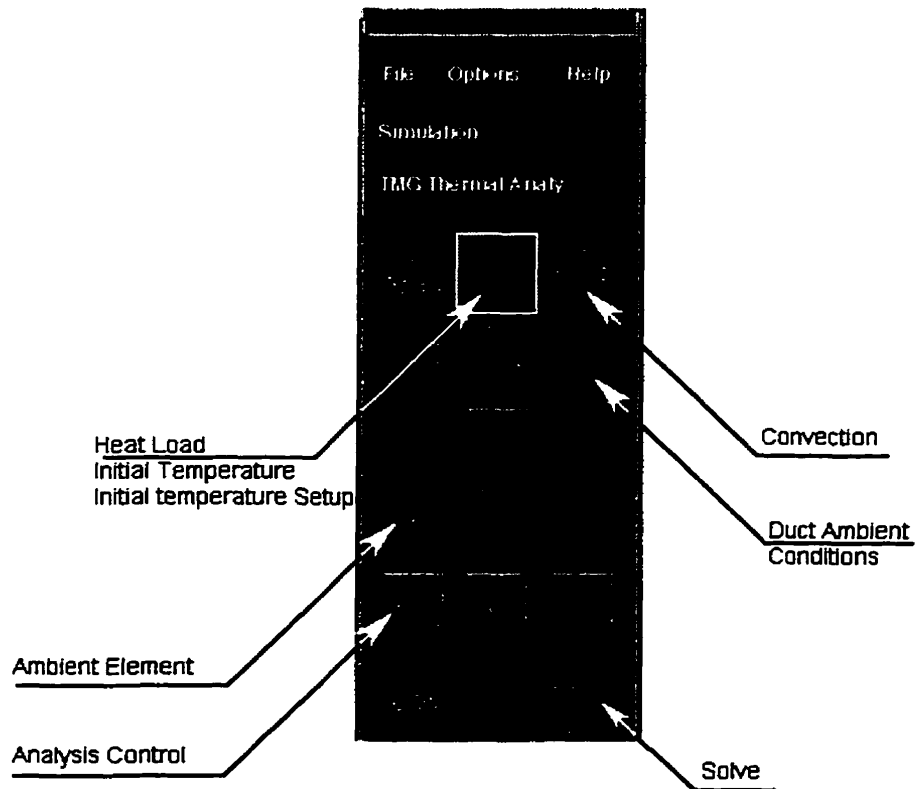


Figure A.1. TMG Thermal Analysis Main Toolbar.

2. In order to create a new heat-load set, one must type its name in the *Name* box and pick *Create*. Figure A.2 shows the heat-load boundary-condition dialog box for the continuous laser. In order to modify one of the entries, it must be highlighted, which in turn will permit the *Modify* icon to be picked. The L1C entry corresponds to the first strip of elements, L2C to the second strip of elements, and so on.

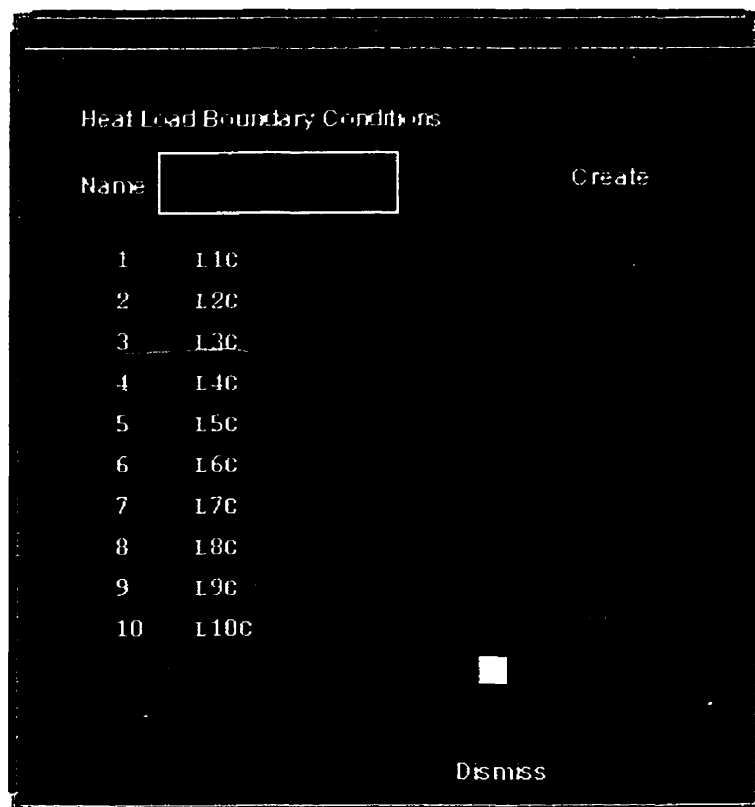


Figure A.2. Heat Load Dialog Box.

3. Picking the *Modify* icon brings the *Heat Load Boundary Condition - Modify* Dialog Box, Figure A.3. The *Elements* sub-dialog box permits desired elements to be picked in order to apply heat load. The *Constant* radio button permits the constant and *Time Varying* heat loads to be defined.



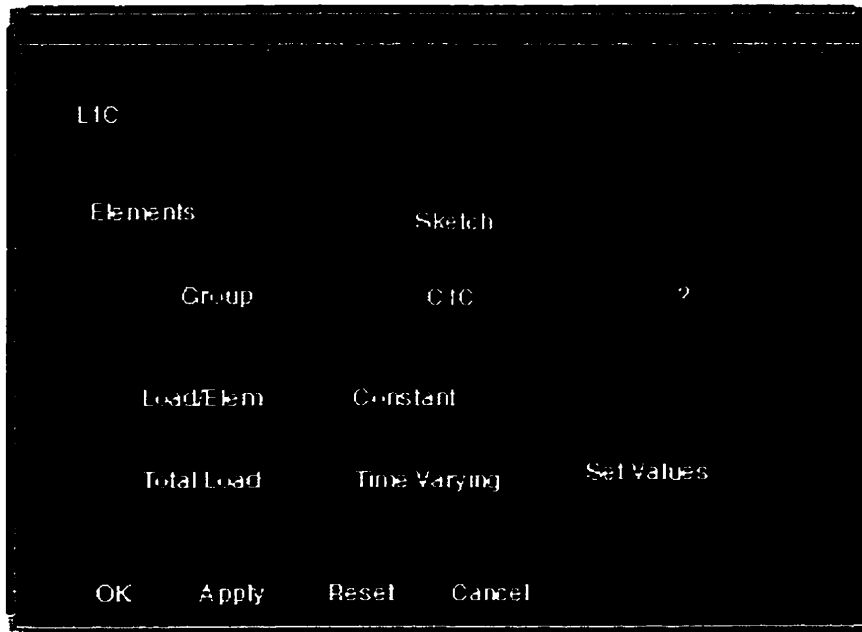


Figure A.3. Heat-Load Boundary-Condition-Modification Dialog Box.

4. Picking the *Time-Varying* button will bring up the *Tabular Data* dialog box, Figure A.4. Heat loads in this thesis were defined as time varying for both pulsed and continuous lasers. This permitted to solve the model in one run. For this purpose, the heat loads were defined for each group of elements, corresponding to the laser-spot location.

The heat-load application time can be defined either as tabulated data or as a function. The heat-load application's start time must be equal to 0, and the end time must be greater than that of the thermal analysis. Otherwise, a run-time error will occur and the analysis will be aborted.

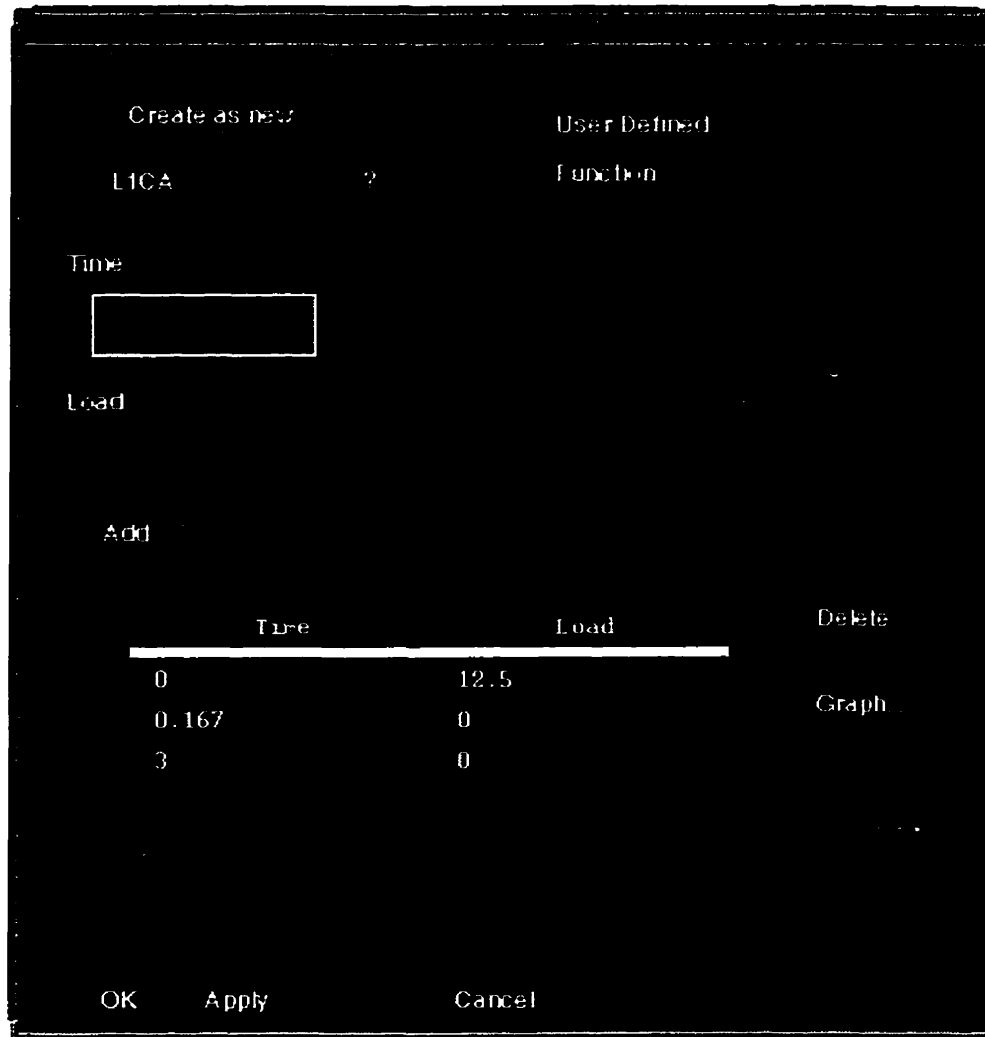


Figure A.4. Tabular Data for Heat-Load Boundary Condition.

### A.2.2 Convection

In order to be able to carry out thermal analysis, the model must be provided with one or more “heat dissipation paths”, as defined by IDEAS. The convection boundary condition is used for this purpose in this thesis. The model must be coated with surface-coating elements in order to be used for convection heat-transfer analysis.

Non-geometric elements representing the surroundings of the model must be created by picking *Non-Geometric Element* icon in main toolbar. Usually, a name

*Ambient* is used. Its properties must be set by picking *Duct Ambient Conditions* icon. If a material for this element is not specified, the simulation will be aborted at runtime.

Picking the *Free Convection* icon brings up the *Free-Convection Couplings* dialog box, Figure A.5. At least one convection boundary-condition set must exist in the model. This set can be modified by picking the *Modify* icon. This in turn will bring up a *Free-Convection-Coupling-Modify* dialog box, Figure A.6. Here, all the visible elements must be selected as convecting, and the ambient as a fluid element.

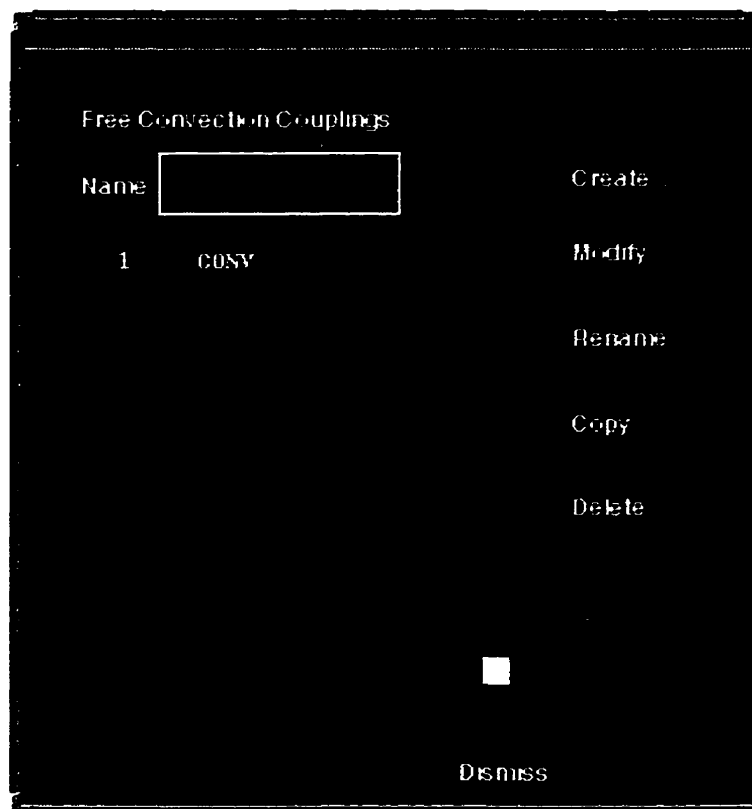


Figure A.5. Free Convection Dialog Box.

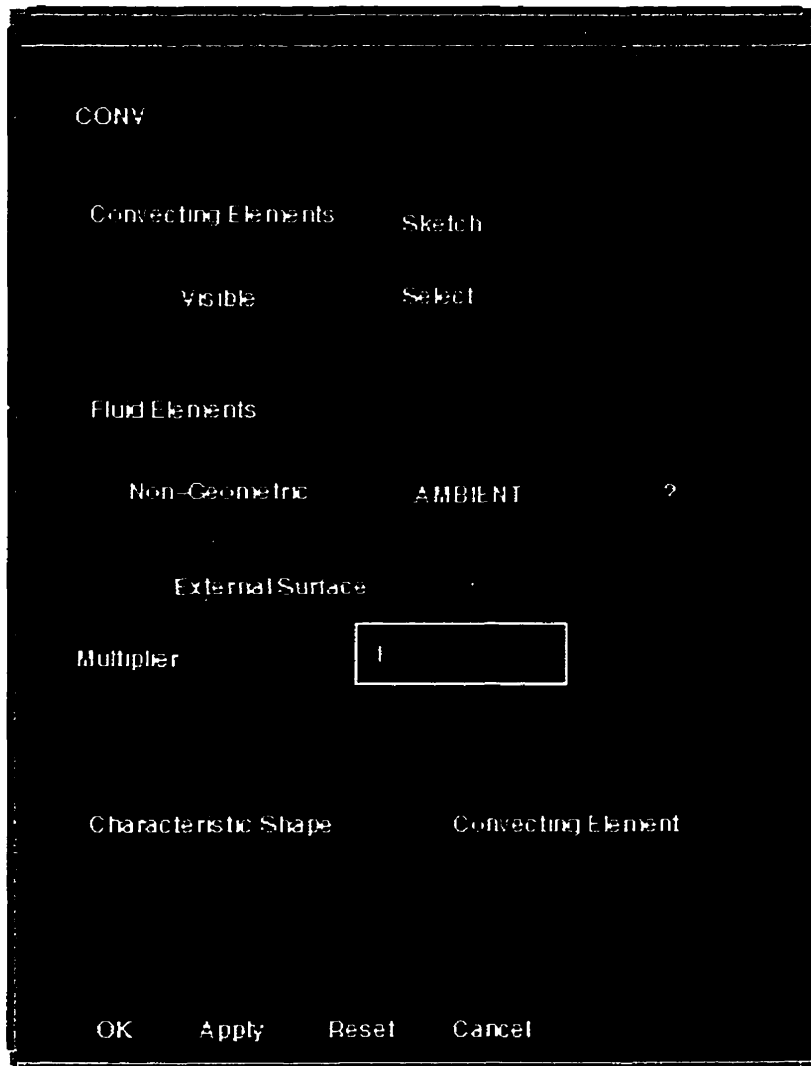


Figure A.6. Free-Convection Coupling - Modify Dialog Box.

### A.2.3. Initial Temperature Set-up

The initial temperatures for the model must be set by picking the *Initial Temperature* icon in the main toolbar, selecting all the elements in the model, and specifying the desired temperature in the dialog window. The option of starting the analysis using the previous temperature field in the model is provided by *Initial Temperature Setup* icon. For this purpose, the temperature history must be retrieved from

TEMPF file, generated after model's solution, and stored in separate file, Section A.4. The name of this file must be specified in *Initial Temperature Setup* dialog box.

### A.3 Analysis Control

Picking the Analysis Control icon brings up the Analysis Control dialog box, Figure A.7.

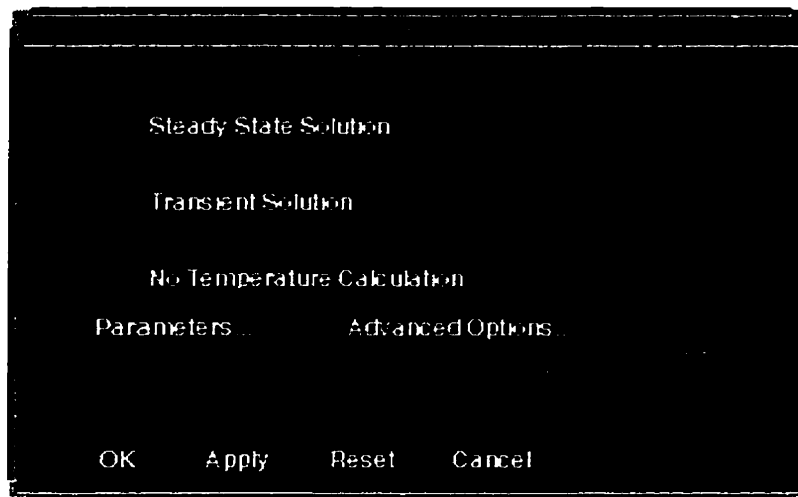


Figure A.7. Analysis Control Dialog Box

The *Transient Solution* button must be checked. Picking the *Parameters* icon brings up the *Transient Analysis Parameters* dialog box, Figure A.8. Here, the analysis' start and end time must be specified, as well as solution method. The solution time-step can be set as constant, time varying, or time-constant multiplier. The last method was used in this thesis. Time-constant multiplier means that the software automatically determine the maximum permissible solution time step from the smallest element size based on the stability criterion. The actual value specified in the dialog box is a fraction of this maximum permissible time step. This parameter must be between 0 and 1, and the

smaller it is, the larger solution time it requires. It is recommended to keep this value at 0.5<sup>1</sup>.

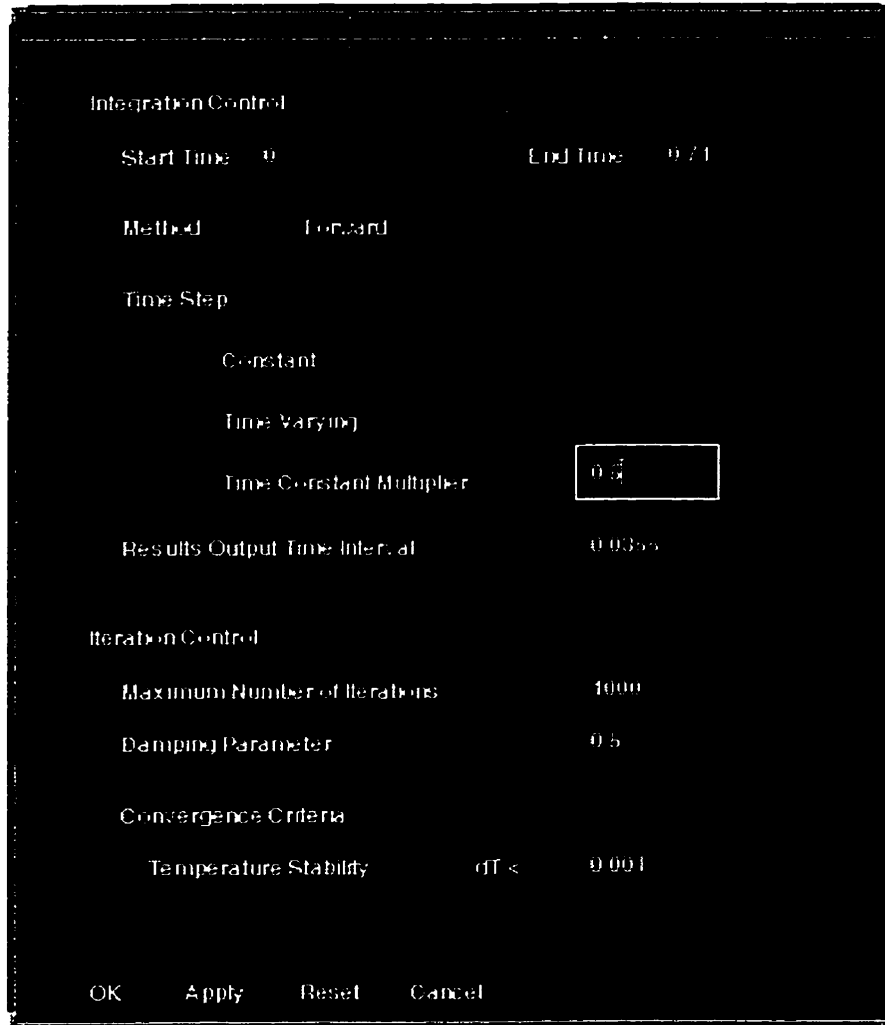


Figure A.8. Transient Analysis Parameters Dialog Box.

## A.4 Analysis Solution and Post-Processing

After specifying all the settings, picking the *Solve* icon in the main toolbar leads to the model solution. At the beginning of the analysis the software asks whether it should stop at warnings or ignore them. The latter option is recommended.

---

<sup>1</sup> I-DEAS TMG On-Line Manual

Number of data files is generated during the solution. Two of them are of particular interest - TEMPF and GTEMPF. The former holds information about the element temperatures, and the latter about the nodal temperatures. The structures of both are the same, as shown in Figure A.9. This is an ASCII text file and starts with -99999, followed by the time corresponding to the following block of data. The data corresponding to the next time step starts after -99999. The element (or node) numbers are in the right column, and the temperatures are in the left.

In order to use the information in the TEMPF file as the initial temperature setting for the subsequent analysis, one must copy the desired block of data, i.e., everything contained between the two lines starting with -99999, into a separate file. The name of this file should then be specified in the *Initial Temperature Setup* dialog box.

In order to use the information in the GTEMPF file, for cladding's geometrical properties calculation, one must create individual files for each time step. Such files must start with -99999, retain the original data structure of the GTEMPF file, and have the extension \*.txt.

```

-99999 3.1950000E-01
      1 2.1943676E+01
      2 2.1938618E+01
      3 2.1923517E+01
      4 2.1898941E+01
      5 2.1865761E+01
      6 2.1825024E+01
      7 2.1777790E+01
-----
-----
5635 1.5928954E+02
5636 1.5773824E+02
-99999 3.9700000E-01
      1 2.1943676E+01
      2 2.1938618E+01
-----

```

Figure A.9. Data File Structure.

## **APPENDIX B: Cladding Geometrical-Properties Calculation using MATLAB**

The files necessary for the cladding's geometrical properties calculation are located in Mercury/users/vladimir/matlab. The files used for this purpose are MATLAB script files with extension \*.m. These files can be modified using any text editor, such as Notepad, Write, MS Word, etc. In order to run these files, MATLAB must be running, and the name of the file should be typed in the command prompt.

### **B.1 Retrieval of Thermal-Modeling Results**

In order to retrieve thermal-modeling results, one must use the **getemp.m** program. No editing is necessary for this program. The files containing nodal temperatures must be stored within the Mercury/users/vladimir/matlab directory. The program searches for \*.txt files in the directory and shows a list of available files. When the file name is specified in command prompt, the program asks for a name of the range file. If **range1.txt** is used, the nodal temperatures along the scanning path (on the symmetry line) for all model's layers of elements are generated. If **r.txt** is used instead, only the top three layers, i.e., the top surface of the powder, the mid-surface of the powder, and the top surface of the baseplate, are output. For transverse temperature profiles **rantrv.txt** must be used.

### **B.2 Calculations for the Pulsed-Laser Mode**

The files used for the calculation of cladding's geometrical properties for the pulsed laser are:



- **cc\_final.m** - The main script file,
- **cc\_input.m** - The initial input file. It is used for the calculation of the properties of a spherical mass, built by the first pulse, and
- **cc\_inpu2.m** - The input file used for all pulses, starting from the second

The procedure of the pulsed-laser cladding's geometrical-properties calculation is as follows:

1. Determine molten zones radii  $R_{tp}$ ,  $R_{mp}$ , and  $R_{ts}$  for each pulse used in the analysis, as described in Section 3.5.2. The values of all the parameters must be in millimeters.
2. Open the **cc\_input.m** file with text editor and input radii values for the first and the second pulses in the spaces provided. The variable names in the file are in all capital letters, e.g., RTP corresponds to  $R_{tp}$  for the first pulse, and RTPN corresponds to  $R_{tp}$  for the second (new) pulse.
3. Input the initial powder-layer thickness,  $H_{pl}$ , which corresponds to HPL in the initial input file and the distance between adjacent pulses' centers  $m$ . In order to output the geometrical properties of the first spherical mass, one must remove semicolons from the ends of the lines, starting with "R =", and "H = ".
4. Save the input file and close it.
5. Make sure that, in the file **cc\_final.m**, the line containing the name of the initial input file **cc\_input** is NOT commented (the "%" must be removed), and the line containing **cc\_inpu2** is commented.
6. Type **cc\_final** in MATLAB command prompt. The program will output the **second** spherical mass' geometrical properties, Figure B.1. RCYL in the program corresponds to  $R_c$  and RNEW CUT to  $R_{cnew}$  in the thesis' text.

7. Record the values underneath the dashed lines, and input them into `cc_inpu2.m`, where needed. The radii of the molten zones must also be input. The initial values (RTP, RMP, RTS) will now correspond to the second pulse radii, and new ones (RTPN, RMPN, RTSN) to the third.
8. Save the input file `cc_inpu2.m` and close it.
9. Comment `cc_input` in `cc_final.m`, and uncomment `cc_inpu2`. Save `cc_final.m`.
10. Repeat Steps 6-9 for as many pulses as needed.

```

MATLAB Command Window

Radius on the Steel Top Surface for Previous Pulse (RCYL) = 0.3547
Total Volume of Remelted Part of Spherical Segment      = 0.02226
Total Volume of Remelted Powder                          = 0.02308
Total Volume of the Spherical Segment Built by Next Pulse = 0.04534
-----
Radius of Current Spherical Segment (R)                  = 1.44
Radius on the Steel Top Surface (RNEW CUT)               = 0.3787
Center Offset (n)                                       = 0.8486
Highest Z Point (zp)                                    = 0.1805
n for New Calculation (nc)                               = 0.5713
Height Offset (h)                                       = -1.258

```

Figure B.1. Typical Output from `cc_final.m` Program.

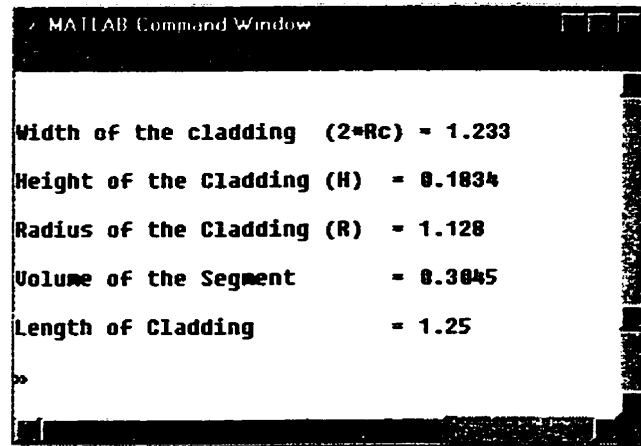
### B.3 Calculations for the Continuous-Laser Mode

The files used for the calculation of cladding's geometrical properties for the continuous laser are:

- `cont01.m` - The main script file,

- **con\_inp1.m** - The input file.

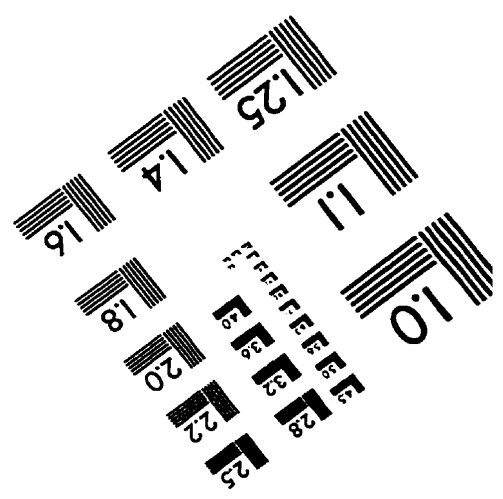
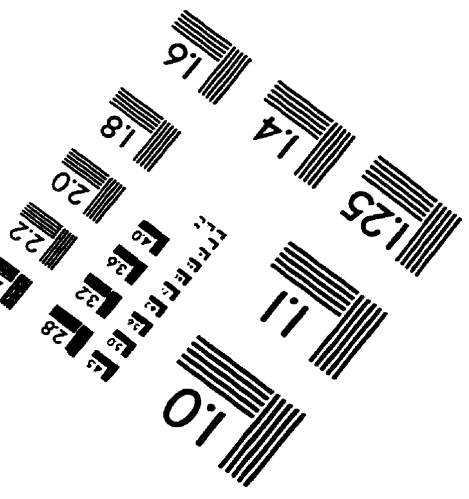
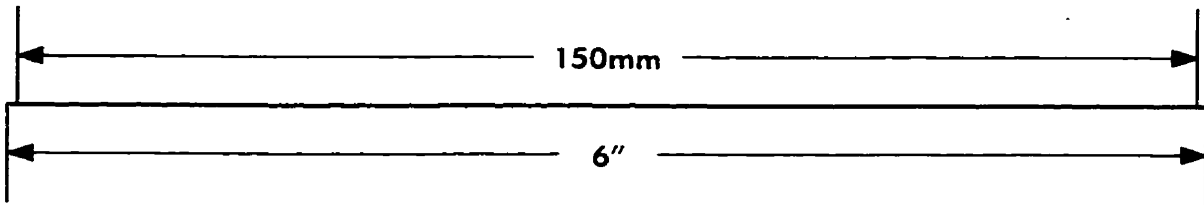
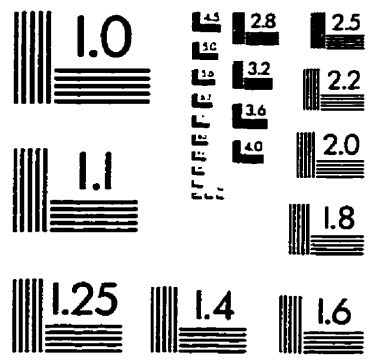
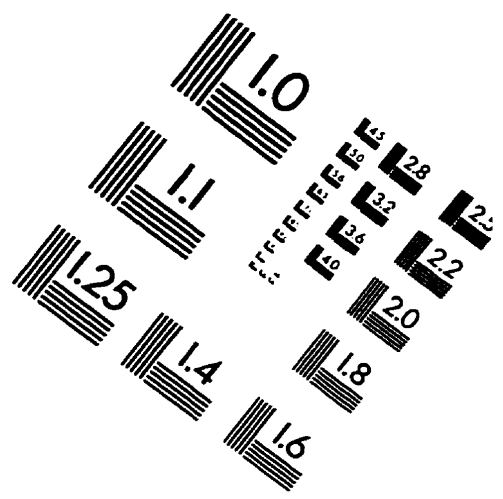
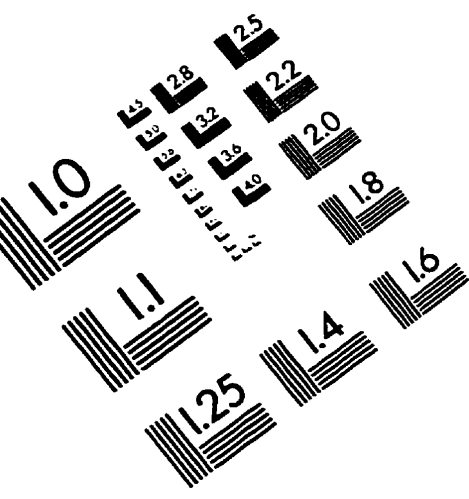
Here, only one input file is used, and, hence there is no need to edit the main script file. The procedure for input is the same as in case of the pulsed laser. The program returns width, height, and radius of the cladding, all in mm, Figure B.2



```
MATLAB Command Window  
  
Width of the cladding (2*Rc) = 1.233  
Height of the Cladding (H) = 0.1834  
Radius of the Cladding (R) = 1.128  
Volume of the Segment = 0.3845  
Length of Cladding = 1.25  
»
```

Figure B.2. Typical Output from cont01.m Program.

# IMAGE EVALUATION TEST TARGET (QA-3)




**APPLIED IMAGE, Inc**  
 1653 East Main Street  
 Rochester, NY 14609 USA  
 Phone: 716/482-0300  
 Fax: 716/288-5989

© 1993, Applied Image, Inc.. All Rights Reserved